DOCTORAL THESIS

Improving Beam-Based Regulation for Continuous-Wave Linear Accelerators with a Disturbance Model-Based Design

Andrei Maalberg

TALLINNA TEHNIKAÜLIKOOL
TALLINN UNIVERSITY OF TECHNOLOGY
TALLINN 2023

TALLINN UNIVERSITY OF TECHNOLOGY
DOCTORAL THESIS
51/2023

Improving Beam-Based Regulation for Continuous-Wave Linear Accelerators with a Disturbance Model-Based Design

ANDREI MAALBERG

TAL TECH PRESS

TALLINN UNIVERSITY OF TECHNOLOGY
School of Information Technologies
Department of Computer Systems

The dissertation was accepted for the defence of the degree of Doctor of Philosophy in Information and Communication Technology on 25 September 2023

Supervisor: Ph.D., Tenured Full Professor Eduard Petlenkov
Department of Computer Systems, School of Information Technologies
Tallinn University of Technology
Tallinn, Estonia

Co-supervisor: Ph.D., Michael Kuntzsch
Department of Radiation Source ELBE, Institute of Radiation Physics
Helmholtz-Zentrum Dresden-Rossendorf
Dresden, Germany

Opponents: Ph.D., Sven Pfeiffer
Deutsches Elektronen-Synchrotron
Hamburg, Germany

Ph.D., Associate Professor S. Hassan HosseinNia
Delft University of Technology
Delft, Netherlands

Defence of the thesis: 09 November 2023, Tallinn

Declaration:
Hereby I declare that this doctoral thesis, my original investigation and achievement, submitted for the doctoral degree at Tallinn University of Technology, has not been submitted for any academic degree elsewhere.

Andrei Maalberg _____
signature

Copyright: Andrei Maalberg, 2023
ISSN 2585-6898 (publication)
ISBN 978-9916-80-053-9 (publication)
ISSN 2585-6901 (PDF)
ISBN 978-9916-80-054-6 (PDF)
Printed by Koopia Niini & Rauam

TALLINNA TEHNIKAÜLIKOOL
DOKTORITÖÖ
51/2023

Pidevlaine lineaarsete kiirendite kiire põhise reguleerimise täiustamine häiringu mudelil põhineva sünteesi abil

ANDREI MAALBERG

TAL TECH
KIRJASTUS

Contents

List of Publications 7

Author's Contributions to the Publications 8

Abbreviations 9

1 Introduction 11
- 1.1 Scope of this Work 12
  - 1.1.1 RF Station 12
  - 1.1.2 LLRF Control System 13
  - 1.1.3 Bunch Compressor 15
  - 1.1.4 Bunch Arrival Time Monitor 17
  - 1.1.5 Linear Accelerator ELBE 19
- 1.2 State of the Art 19
- 1.3 Motivation and Problem Statement 21
- 1.4 Author's Contributions 22
- 1.5 Thesis Outline 23

2 Exploiting RF Noise for Disturbance Modeling 25
- 2.1 Analysis of Measured RF Noise Data 25
- 2.2 Simulation Model for RF Noise Propagation to Electron Beam 26
  - 2.2.1 RF Noise Modeling 26
  - 2.2.2 Bunch Compressor in Simulink 28
- 2.3 Conclusions 30

3 Improving Beam-Based Regulation with a Disturbance Model-Based Design 33
- 3.1 Beam-Based Regulation 33
- 3.2 Disturbance Model-Based Design 39
  - 3.2.1 Using $\mathcal{H}_2$ Mixed-Sensitivity Problem 39
  - 3.2.2 Evaluation at ELBE 45
- 3.3 Conclusions 47

4 Implementing a High-Order State-Space Regulator for Fast Beam-Based Feedback 49
- 4.1 Toward Digital Beam-Based Regulator 49
- 4.2 Integration with MTCA.4 Digital Platform 51
  - 4.2.1 Hardware/Software Interface 52
  - 4.2.2 Fixed-Point Analysis of Regulator Signals and Gains 54
  - 4.2.3 Top-Level Architecture of VHDL Firmware Framework 56
- 4.3 Using DSP48E1 for Proportional Regulator 57
- 4.4 State-Space Implementation for $\mathcal{H}_2$ Regulator 58
  - 4.4.1 Systolic Array Structure 58
  - 4.4.2 Data Flow To Drive Systolic Arrays 60
  - 4.4.3 Application Modeling in Terms of Data Flows 61
  - 4.4.4 Finite-State Machine 62
  - 4.4.5 Evaluation of Latency and Usage of FPGA Resources 63
- 4.5 Firmware Verification 64
- 4.6 Conclusions 65

Conclusions 69

References 72

Acknowledgements 79

Abstract 80

Kokkuvõte 81

Appendix 1 Sensitivity Functions S and T 83

Appendix 2 Algebraic Riccati Equation 85

Appendix 3 87

Appendix 4 97

Appendix 5 107

Appendix 6 131

Curriculum Vitae 146

Elulookirjeldus 148

List of Publications

The present Ph.D. thesis is based on the following publications that are referred to in the text by Roman numbers.

I A. Maalberg, M. Kuntzsch, and E. Petlenkov. Simulation of RF Noise Propagation to Relativistic Electron Beam Properties in a Linear Accelerator. In *Proc. 21st IFAC World Congr.*, pages 348–354, Jul 2020

II A. Maalberg, M. Kuntzsch, and E. Petlenkov. Regulation of the Linear Accelerator ELBE Exploiting Continuous Wave Mode of a Superconducting RF Cavity. In *Proc. 2022 Am. Control Conf.*, pages 5346–5353, Jun 2022

III A. Maalberg, M. Kuntzsch, and E. Petlenkov. Real-Time Regulation of Beam-Based Feedback: Implementing an FPGA Solution for a Continuous Wave Linear Accelerator. *Sensors*, 22(16):6236, Aug 2022

IV A. Maalberg, M. Kuntzsch, K. Zenker, and E. Petlenkov. Regulation of electron bunch arrival time for a continuous-wave linac: Exploring the application of the $\mathcal{H}_2$ mixed-sensitivity problem. *Phys. Rev. Accel. Beams*, 26:072801, Jul 2023

Author's Contributions to the Publications

All results in I–IV were obtained by the author of the thesis under the supervision of Dr. Michael Kuntzsch and Prof. Dr. Eduard Petlenkov.

I In I a Simulink model was developed to analyze the propagation of radio frequency noise to electron beam properties. To simulate the radio frequency noise, the author of the thesis created a dynamical model that was based on data from the continuous-wave linear accelerator ELBE. The data was kindly provided by Dr. Michael Kuntzsch. The created noise model laid the foundation for further design of a beam-based regulator.

II The contribution of the author of the thesis in II lies in the design of a beam-based regulator formulated in the context of the $\mathcal{H}_2$ mixed-sensitivity problem. The regulator design was tailored to a disturbance model that was based on real-world noise data. The performance evaluation of the designed regulator was carried out by means of software simulation.

III In III a real-time feasible solution was proposed for the implementation of a beam-based regulator. Specifically, an FPGA-based implementation was developed in the hardware description language VHDL. The implementation used a firmware framework from the Deutsches Elektronen-Synchrotron to perform mundane tasks, such as communicating with other FPGA boards, establishing a user interface with software and data saving to memory. To verify the implementation, the author of the thesis devised a hardware testbench, formed of two interconnected FPGA boards.

IV The problem of improving a commonly used proportional beam-based regulator was considered in IV. For this purpose, the proportional regulator was produced and then compared to an $\mathcal{H}_2$ regulator. The latter was designed to take process disturbance explicitly into account. The comparison was performed through a set of measurements at the continuous-wave linac ELBE.

Abbreviations

API	Application programming interface
a.u.	Arbitrary unit
BAM	Bunch arrival time monitor
CPU	Central processing unit
CW	Continuous-wave
DALI	Dresden advanced light infrastructure
DAQ	Data acquisition
DDR	Double-data rate
DESY	Deutsches Elektronen-Synchrotron
DSP	Digital signal processor
ELBE	Electron linear accelerator for beams with high brilliance and low emittance
FPGA	Field-programmable gate array
FSM	Finite-state machine
HW/SW	Hardware/software
HZDR	Helmholtz-Zentrum Dresden-Rossendorf
II	Internal interface
IP	Intellectual property
Linac	Linear accelerator
LLL	Low-latency link
LLRF	Low-level radio frequency
LQR	Linear quadratic regulator
MIMO	Multiple-input multiple-output
MTCA	Micro telecommunications computing architecture
PCIe	PCI Express
RF	Radio frequency
rms	Root-mean-square
SFP	Small form-factor pluggable
SISO	Single-input single-output
SRF	Supeconducting radio frequency
SSPA	Solid-state power amplifier
TELBE	Terahertz facility at the ELBE accelerator
TESLA	Teraelectronvolt superconducting linear accelerator
UML	Unified modeling language

1 Introduction

The present thesis is devoted to a highly interdisciplinary work that is governed by accelerator physics, control theory and digital logic. By uniting these disciplines, a solution emerges that not only extends our knowledge regarding the stability of linear accelerators, but also provides an elaborated technical implementation that is ready for a technology transfer. At the same time, the thesis aims to bridge a gap between different communities that are represented by the three above-mentioned disciplines and, thus, advocate fruitful collaborations, such as the current work.

More specifically, this work is carried out in the context of an accelerator-based light source, called Terahertz facility at the ELBE accelerator (TELBE) [22, 34], in which accelerated electrons emit flashes of light in the far infrared spectrum of electromagnetic radiation. This light, which is generally referred to as the secondary radiation, is then used by scientists to conduct material research [23, 24, 35]. Technically, such light generation can be partitioned into the following stages. First, the electrons, which are denoted here as e^-, are produced by an electron source, or gun, which in case of TELBE employs a laser-excited cathode to release electrons. When the electrons leave the gun, they already have an energy of a few megaelectronvolts. Then, these electrons are accelerated to a target energy of about $30\,\mathrm{MeV}$ using radio frequency electromagnetic fields. At this energy, the electrons are in the relativistic regime, where they travel at almost the speed of light. Finally, a magnetic structure, called undulator, applies a periodic magnetic field on the electrons, thus, forcing them to take a sinusoidal trajectory. This motion makes the electrons emit light, see Figure 1.

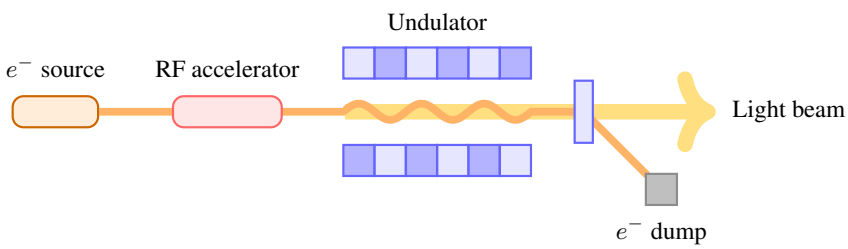

Figure 1: General schematic of an accelerator-based light source.

In terms of material research, an accelerator-based light source represents a valuable tool to capture dynamics that occur in materials on an ultra-fast timescale, typically picosecond and femtosecond timescales. These are time-resolved pump-probe experiments [64] that are designed to first excite the dynamics in matter with an electromagnetic field of a pump pulse and then probe the excited matter with ultra-short photon pulses in a stroboscopic manner. To achieve a temporal resolution of a few tens of femtoseconds root-mean-square (rms), these experiments rely on a tight synchronization between a pump source, which is typically an optical laser, and a source that generates the probes, i.e. the accelerator-based light source. Figure 2 shows experimental data that is measured [34, 11] under different levels of synchronization. For demonstration purposes, the blurry result was produced by artificially distorting the laser system on the experimental side.

So besides potential instabilities in the optical laser, the temporal stability of the electron accelerator, specifically of the underlying electron beam, is therefore of critical importance. This stresses the need to apply proper beam regulation and, simultaneously, defines the scope of this work.

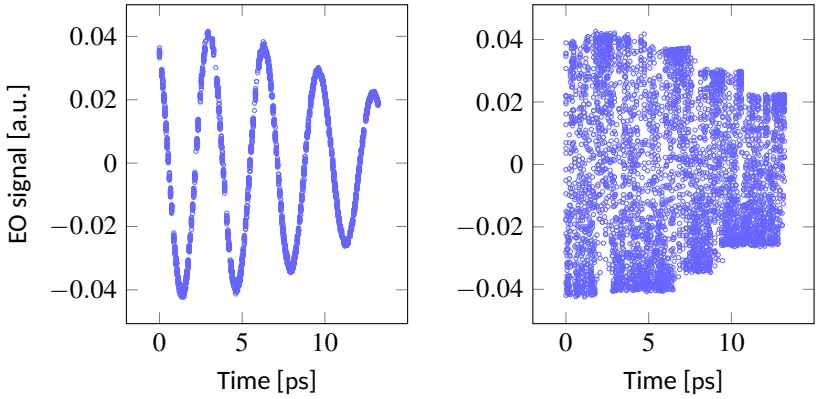

Figure 2: Electro-optical signal that shows the probing of dynamics inside excited matter in case of different levels of synchronization.

1.1 Scope of this Work

The scope of this thesis is defined by a technology that is fundamental to radio frequency accelerators—bunch compression [76, 18, 17]. Besides its direct purpose to compress an electron bunch, this technology has a side-effect, which delays or advances the bunch with respect to some target position in a beamline, thus changing the so-called arrival time of the bunch. In this work, the indirect use case is expected to allow the regulation of the electron bunch arrival time, and, for this purpose, the given open-loop system includes

- Low-level radio frequency (LLRF) controller to actuate the process of bunch compression
- Bunch compressor as the plant of this system
- Bunch arrival time monitor (BAM) to sense the bunch arrival time and provide feedback

In what follows, an overview of these open-loop components is given, and their existing installations on the Electron Linear accelerator for beams with high Brilliance and low Emittance (ELBE), i.e. the accelerator that drives TELBE, are presented.

1.1.1 RF Station

The central part of a radio frequency (RF) station is a mechanical structure called cavity that is designed to house a resonating RF field. Depending on the purpose of a concrete station, different cavity types may be employed [52, 10, 73], including superconducting RF (SRF) cavities that were developed in the context of a teraelectronvolt superconducting linear accelerator (TESLA) collaboration and that are now commonly used for the purpose of electron acceleration. Figure 3 illustrates a standard 9-cell TESLA cavity housing a standing electromagnetic wave. Since the RF fields inside the cavity cells are phase shifted relative to each other by 180 degrees (hence the name π-mode), a relativistic electron bunch sees the accelerating voltage amplitude nine times in a row, thus becoming increasingly accelerated.

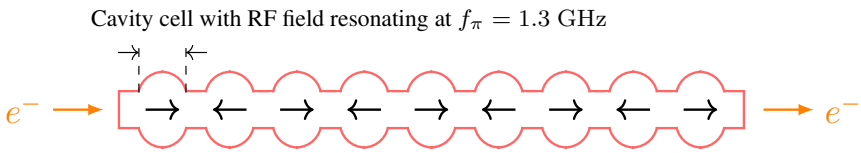

Figure 3: TESLA cavity housing a standing electromagnetic wave. Black arrows denote the field gradients at one point in time.

Due to its inherently high quality factor, the TESLA cavity exhibits a rather narrow bandwidth. For example, the TESLA cavity installed at ELBE has a loaded quality factor in the range of $Q_{L\pi} \approx 6.5 \cdot 10^6$, which yields

$$f_{\frac{1}{2}} = \frac{f_\pi}{2Q_{L\pi}} \approx 100\,\text{Hz}, \tag{1}$$

where $f_\pi = 1.3$ GHz and denotes the cavity resonance frequency, and where $f_{\frac{1}{2}}$ is the cavity half-bandwidth. Such narrow bandwidth leads to a rather slow time response, which seriously restricts the regulation options of a potential algorithm. The situation is improved to some extent when the cavity is operated in closed loop, because the gain applied by a dedicated LLRF controller extends the closed-loop bandwidth to the range of $f_{\frac{1}{2}} \approx 35$ kHz [80]. Consequently, by treating the LLRF controller as an interface to the RF cavity, the beam-based regulator can expect a faster response. Of course, understanding the structure and dynamics of the LLRF control system is then of utmost priority.

1.1.2 LLRF Control System

As depicted in Figure 4, the goal of the LLRF control system is the tracking of the RF field variables, i.e. the amplitude A and phase ϕ. However, due to implementation specifics, the LLRF controller does not operate with A and ϕ directly, but with their in-phase I and quadrature Q representations. Stabilized by the LLRF controller, these I and Q signals are then applied inside a vector modulator (VM) to modulate a reference RF signal coming from a master oscillator. Since the signals generated by the LLRF controller are in the range of milliwatts (hence the name low-level RF), a solid-state power amplifier (SSPA) is used to drive the modulated RF signal to a kilowatt range. This finally results in a high-power RF signal that is passed through a waveguide to the TESLA cavity.

From the control point of view, the RF station represents a dynamical multiple-input multiple-output (MIMO) system [57, 63] that is expressed as

$$\begin{bmatrix} y_I \\ y_Q \end{bmatrix} = \begin{bmatrix} G_{11} & G_{12} \\ G_{21} & G_{22} \end{bmatrix} \begin{bmatrix} r_I \\ r_Q \end{bmatrix}, \tag{2}$$

where G_{ij} are the closed-loop transfer functions of I and Q signals. Then, the LLRF controller [55, 58] that is installed at ELBE [80, 53] uses the following concepts to achieve better control of the RF station: decoupling of the I and Q; suppression of the parasitic fundamental modes of the TESLA cavity. These concepts can be illustrated by the magnitude frequency response of the corresponding closed-loop system, see Figure 5. It is seen how the off-diagonal transfer functions G_{12} and G_{21} are suppressed in the low-frequency range in order to minimize coupling between the I and Q variables. Following this, it can be assumed that there are only two single-input single-output (SISO) transfer functions in the system, i.e. G_{11} and G_{22}. There is also a steep high-frequency roll-off at about 750 kHz that designates the suppression of the parasitic $\frac{8}{9}\pi$ fundamental mode of the

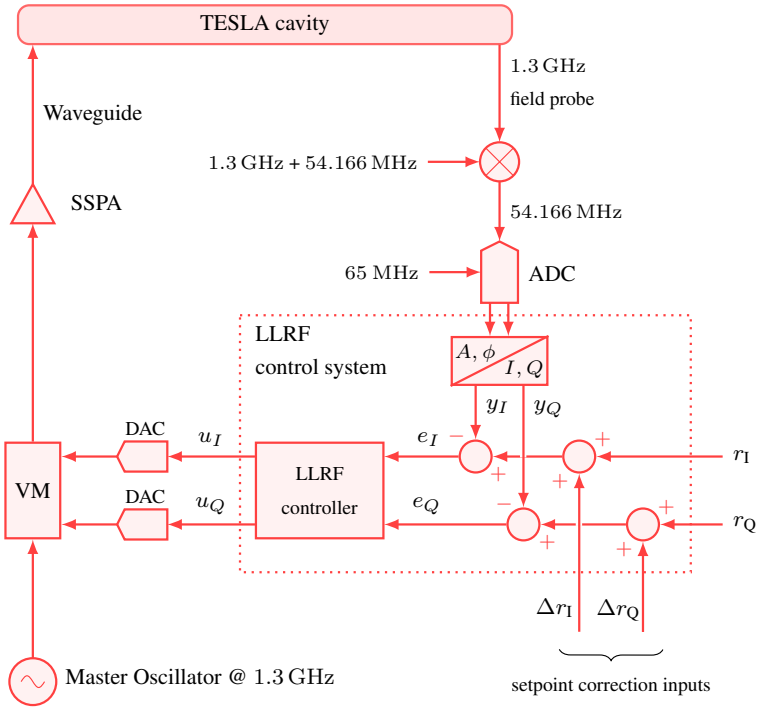

Figure 4: Schematic of an RF station that is installed at ELBE together with its associated LLRF control system. Adapted from [51, 65].

TESLA cavity. In addition, the illustrated frequency response reveals the bandwidth of the closed-loop LLRF system, which is about 35 kHz.

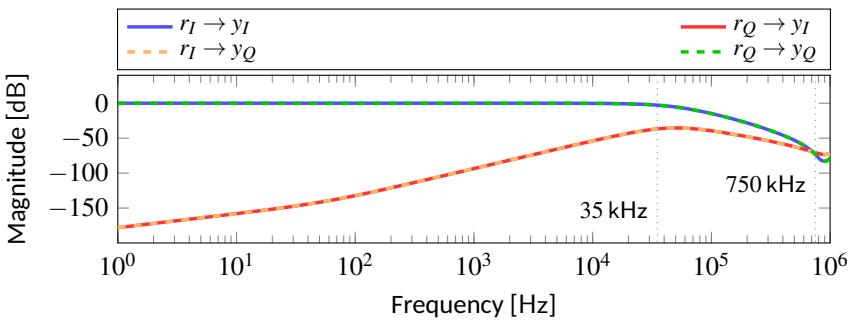

Figure 5: Magnitude frequency response of the closed-loop LLRF control system.

Similarly, taking a closer look at the open-loop transfer function can reveal another important aspect of the present LLRF control system, namely the corresponding gain and phase margins [50], see Figure 6. The gain margin G_M is determined by first finding the frequency f_{G_M}, where the phase response crosses the level of -180 degrees. Then, the magnitude response is evaluated at that frequency, and the difference between the evaluated value and a 0 dB level defines G_M. A likewise procedure is carried out to determine the phase Φ_M. This time, the frequency f_{Φ_M} is found by examining the 0 dB crossing of the magnitude response. The phase response is then evaluated at the found frequency,

and the difference between the evaluated value and the level of -180 degrees defines Φ_M. According to these procedures, the presented open-loop LLRF control system features G_M and Φ_M equal to 11.6 dB and 60 degrees, respectively. It is important to note that the LLRF model used for these calculations already contains an internal time delay of about 1 µs that is derived from system identification [53] performed at ELBE [80]. In case there is more time delay in the system, the phase response will be shifted down, thus decreasing f_{G_M} and, in turn, G_M. Less margin means less gain that can be additionally applied before turning the system unstable.

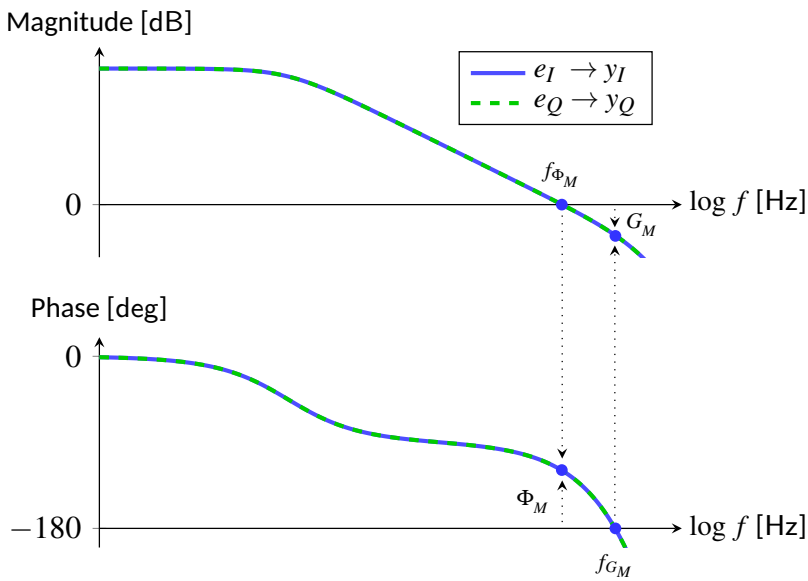

Figure 6: Bode diagram showing gain and phase margins derived from the diagonal open-loop transfer functions of the LLRF control system.

1.1.3 Bunch Compressor

The state of a single particle is usually expressed relative to an orbit, where the orbit is assumed to be the path of a reference particle with nominal parameters. This allows to define a Cartesian frame moving with the reference particle and providing the corresponding x, y and z coordinates, see Figure 7.

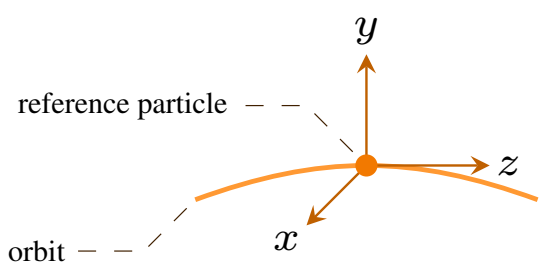

Figure 7: Reference particle moving along an orbit with coordinate frame defined.

Moreover, this concept can be generalized to represent an ensemble of particles, e.g. an electron bunch, by treating the ensemble as its center of mass. It is therefore common to describe the state as a six-dimensional phase space vector [76]

$$\rho = \left[\begin{array}{cccccc} x & x' & y & y' & z & \delta \end{array} \right]^T, \tag{3}$$

where x, y and z are the distances from the orbit, $x' = \partial_x/\partial_z$ and $y' = \partial_y/\partial_z$ are the horizontal and vertical derivatives, respectively, and where $\delta = \Delta E/E_0$ is a relative deviation from the reference energy. To first order, the x, y and z components can be decoupled, and, thus, the rest of the phase space can be neglected in order to concentrate on the longitudinal part

$$\rho_L = \left[\begin{array}{cc} z & \delta \end{array} \right]^T. \tag{4}$$

The main beamline section that is able to change the longitudinal state ρ_L is called bunch compressor. It is a combination of an RF cavity and a magnetic structure called chicane, formed by a minimum of four dipole magnets. The RF cavity is operated off-crest in order to chirp the bunch, i.e. to imprint an energy modulation that correlates with the longitudinal position z within the bunch. Correspondingly, the transfer map of the RF cavity can be expressed as

$$z(s_1) = z(s_0), \tag{5}$$

$$\delta(s_1) = \delta(s_0) + \frac{eA}{E_0} \cos\left(\frac{\omega}{c} z(s_0) + \phi \right), \tag{6}$$

where e is an elementary charge, c is the speed of light, and where A, ϕ and ω are the amplitude, phase and angular frequency of the RF cavity field, respectively. Beamline locations s_0 and s_1 mark the start and end of the RF cavity section, respectively. Then, by means of energy dispersion, the magnets of the chicane force the electrons to travel different paths, depending on the electron energy. Using only first-order terms, the corresponding transfer map is denoted as

$$z(s_2) = z(s_1) + R_{56}\,\delta(s_1), \tag{7}$$

$$\delta(s_2) = \delta(s_1), \tag{8}$$

where R_{56} is a first-order design parameter of the magnetic chicane that translates the energy modulation into a longitudinal position change. Beamline locations s_1 and s_2 mark the start and end of the magnetic chicane section, respectively. The concept of the bunch compressor is illustrated in Figure 8.

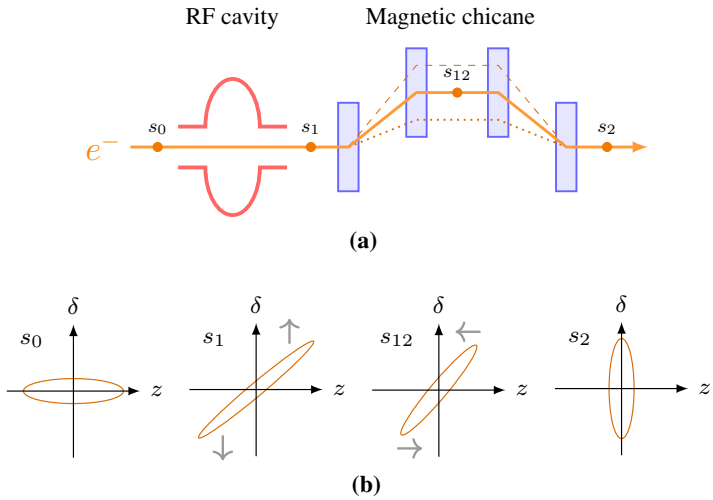

*Figure 8: Schematic of a bunch compressor exhibiting **(a)** the combination of an RF cavity and a magnetic chicane, as well as **(b)** the evolution of the longitudinal phase space of the passing electrons.*

The presented concept shows how electrons travel different paths through the magnetic chicane, depending on the energy received from the RF cavity. So in principle, the bunch compressor changes the longitudinal phase space of the electrons in a two-step sheering process: first, the RF cavity changes the energy distribution within the bunch; and second, the magnetic chicane delays the electrons accordingly.

In case of arrival time, the electron bunch is represented by its center of mass. Thus, setting $z = 0$ and focusing only on the energy modulation introduced by the RF cavity allows to transform (6) into

$$\Delta\delta = \frac{eA}{E_0}\cos\phi. \tag{9}$$

This leads to a similar update of (7) featuring, in addition, a conversion to proper arrival time units

$$\Delta\tau = \frac{1}{v}R_{56}\,\Delta\delta, \tag{10}$$

where τ is the arrival time in seconds, and where $v \approx c$ and denotes the velocity of a relativistic bunch. Therefore, changes of the RF variables A and ϕ cause a change in the arrival time of electron bunches, which can then be diagnosed with the help of a bunch arrival time monitor.

1.1.4 Bunch Arrival Time Monitor

The working principle of the bunch arrival time monitor is based on measuring the arrival time relative to an actively-stabilized optical timing reference. Specifically, periodic pulses of a reference laser are amplitude-modulated with electric signals coming from pick-up antennas [1] that probe the electric field of the passing electron bunch. The arrival time information is, thus, transferred into an amplitude modulation of coincident laser pulses, see Figure 9.

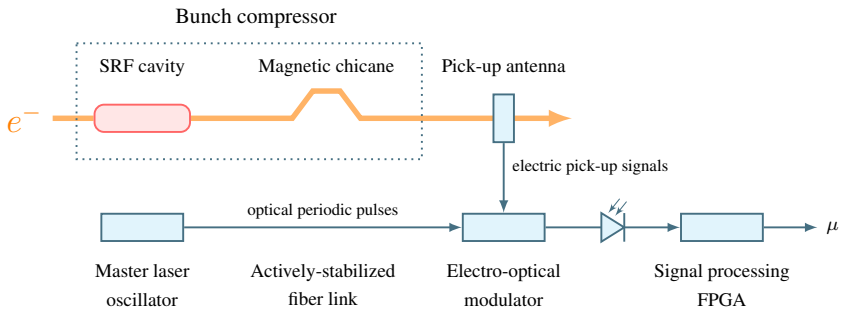

Figure 9: Schematic of a bunch arrival time monitor.

According to such arrival time representation, the output of this sensor is defined by a dimensionless modulation value μ with a working point set to $\mu = 1$. For the purpose of analysis, the dimensionless value μ is converted to a corresponding value τ in picoseconds. Figure 10 exemplifies such analysis that is based on BAM data measured on the ELBE accelerator at a bunch repetition rate of 50 kHz. Note that a linear spectral density $\widetilde{S}_\tau$ [25] is defined in terms of picoseconds, whereas an integrated rms noise σ_τ is demonstrated in femtoseconds. In this work, plots that display frequency-domain data follow this convention. Moreover, the dimensionless deviations of μ around its setpoint are considered to be approximately equal to those of τ expressed in picoseconds. Hence the exclusive usage of τ in the rest of this work.

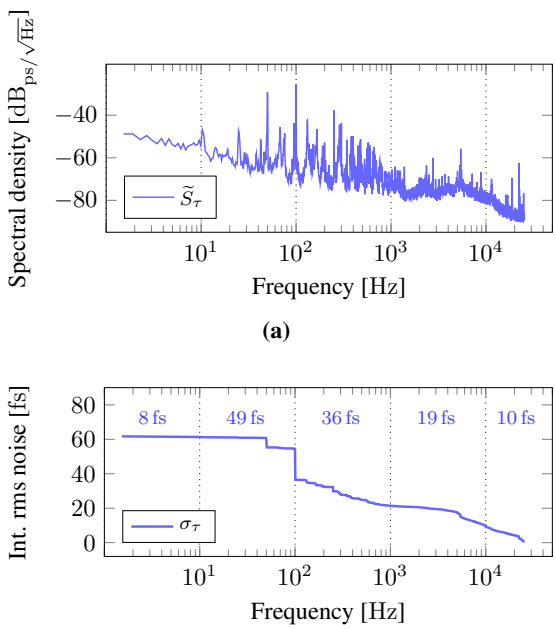

*Figure 10: BAM data displayed as **(a)** a linear spectral density and as **(b)** an integrated rms noise. The data in **(b)** is backward-integrated, such that the rms noise is accumulated toward lower frequency. Furthermore, numbers displayed in every decade correspond to respective rms noise. These numbers need to be summed in a root-mean-square manner to get the overall integrated noise.*

1.1.5 Linear Accelerator ELBE

The linear accelerator ELBE is a versatile light source located at Helmholtz-Zentrum Dresden-Rossendorf (HZDR), Germany. ELBE has been routinely running in user operation since 2004 with stepwise commissioning of secondary radiation targets [47]. These targets include infrared light, fast neutrons, bremsstrahlung and positrons. In addition, ELBE is one of the few electron linear accelerators to be routinely operated in a continuous-wave (CW) mode. In this work, the focus is set on a specific ELBE section that generates light for TELBE, see Figure 11.

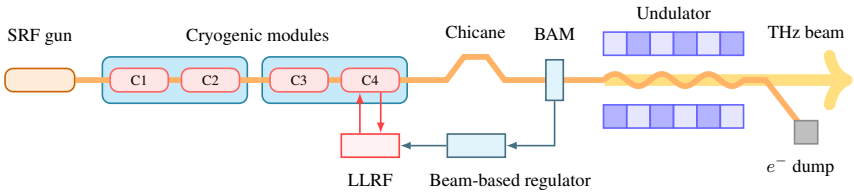

Figure 11: General layout of the ELBE accelerator section that generates the secondary radiation for TELBE. The depicted section features a prospective application of a beam-based regulation loop.

So in case of ELBE, the concept of an accelerator-based light source is implemented as follows. First, electrons are produced by an electron gun that uses an SRF cavity technology similar to the one described in Section 1.1.1. Specifically, the SRF gun [2] employs a 3.5-cell cavity, where the half-cell contains a laser-excited photocathode that releases electrons. The released electrons are formed into electron bunches, and this process is repeated at a typical TELBE rate of $50\,\mathrm{kHz}$. When operated in CW mode at a bunch charge of $225\,\mathrm{pC}$, such train of electron bunches results in $225\,\mathrm{pC} \cdot 50\,\mathrm{kHz} \approx 11\,\mu\mathrm{A}$ of average beam current. Next, the electron bunches are accelerated to $28\,\mathrm{MeV}$. The corresponding linear accelerator consists of two cryogenic modules, each housing two 9-cell TESLA cavities driven by a $1.3\,\mathrm{GHz}$ electromagnetic field. The cryogenic modules are filled with liquid helium to establish temperatures as low as a few kelvins. Under such conditions, niobium, i.e. a material that the TESLA cavities are made of, becomes superconducting, which permits almost lossless creation of high fields inside the cavities. These oscillating electromagnetic fields receive their power from SSPAs. Since there are two combined SSPAs for every cavity, ELBE features eight such amplifiers, each delivering up to $10\,\mathrm{kW}$ of RF power to accelerate electrons. Finally, the undulator forces the accelerated electrons to emit light, as described above.

Therefore, the fundamental bunch compression technology naturally entails concrete devices when applied to ELBE, namely the SRF cavity C4 and the magnetic chicane. These devices form the bunch compressor, which, in turn, represents the plant of the prospective beam-based regulation system. Since C4 is associated with a certain LLRF control system, the latter becomes the actuator. Then, to diagnose bunch arrival time changes, which are caused by this actuator, a BAM is installed downstream of the chicane. Finally, this work focuses on closing the described open-loop system by providing a solution that extends the state of the art.

1.2 State of the Art

Regulating the arrival time of electron bunches is a crucial step to improve the temporal resolution of accelerator-based time-resolved experiments. Nowadays, a regulation method, called beam-based feedback, has been shown to work well for stabilizing longi-

tudinal beam properties on pulsed accelerator machines [33, 56, 61, 68, 66]. The bunch arrival time is among these properties. Essentially, this method resembles a typical design of a proportional regulator, where the plant is represented by an electron beam response matrix, and where the inversion of such matrix produces the regulator. Specifically, the matrix denotes the electron beam response to variations in an RF field that resonates inside an upstream RF cavity. The inverse of such matrix is then incorporated into the LLRF controller to allow adjusting the RF field based on the beam feedback. Therefore, during an RF pulse, i.e. when the RF field is active, the LLRF controller can use the beam-based feedback to compensate the noise acting on the beam.

Contrary to the pulsed operation, a CW mode fills the accelerating cavities with a continuously-driven RF field. That is, an RF field with a $100\,\%$ duty cycle. For a user, the CW mode enables the formation of a continuous uniformly-spaced train of electron bunches with a high repetition rate [20]. Due to a high average beam current generated by such train, a proper irradiation of various experiment samples becomes feasible. In addition, the continuous train of electron bunches that is maintained for a sufficient amount of time greatly improves the statistics of the experiment data. For all of these reasons, an increased interest emerged in recent years towards linear accelerators (linacs) operating in the CW mode. In particular, the construction of the Shanghai hard X-ray free electron laser facility (SHINE) began in 2018 [81]. The Linac Coherent Light Source II (LCLS-II) is nearing completion [82]. Moreover, the European X-ray Free Electron Laser (EuXFEL) considers a CW upgrade in the foreseeable future [7]. In this context, the ELBE accelerator has been operating in the CW mode for over 20 years and, therefore, represents a unique environment to test new algorithms and beamline components [5, 72]. Hence, the results that are obtained at ELBE may have a substantial impact on a growing CW community.

Besides the user benefits, the improved statistics offered by the CW mode also help enhance beam diagnostics related to the feedback. For example, a one-second sampling of the RF field by a $50\,\mathrm{kHz}$ electron beam, i.e. a beam with a $50\,\mathrm{kHz}$ bunch repetition rate, provides data for a spectrum with a frequency resolution of 1 Hz. Since the electron bunches sample the RF noise as well, a high-resolution spectral analysis of such noise becomes feasible [36].

Another important aspect of the superconducting RF cavity is related to its inherently narrow bandwidth [73, 49]. From the regulation point of view, the RF cavity is an actuator, so the narrow bandwidth can cause a rather slow time response of the regulation system. Depending on the actual noise bandwidth that is targeted by the beam-based regulator, the slow actuator may pose a serious limitation for the regulator performance. Even when driven by the dedicated LLRF controller that extends the closed-loop bandwidth, the superconducting RF cavity can still remain a limitation [52].

Despite the slow actuator, regulating the arrival time of electron bunches is considered a fast process [56]. Indeed, the sampling step of a corresponding digital regulator is defined by the bunch repetition rate, and the latter can reach several megahertz. This leads to a necessity to work with sampling times that reside on a sub-microsecond level. Obviously, such regulator requires an efficient, yet adjustable implementation of its algorithm, thus strongly suggesting a digital solution that is based on a field-programmable gate array (FPGA). In fact, low latency and high reconfigurability—the outstanding features of FPGAs—facilitated the adoption of FPGA-based solutions by accelerator community [62, 60, 75, 70, 67]. And thus, electron linear accelerators, such as ELBE and EuXFEL, feature the LLRF controllers [80, 62] and BAMs [38, 21] that are implemented on these highly efficient digital circuits.

To keep the sampling steps as short as possible, a common practice [67, 55] is to re-

duce the order of the LLRF controller with the help of fixed-order optimization [8, 59]. Converted to its transfer function form, the low-order controller is then implemented on an FPGA in terms of digital infinite impulse response (IIR) filters. On the one hand, this approach could also be favorable for the beam-based regulator, provided there is an FPGA-based solution that comes with ready implementations of the IIR filters. On the other hand, the fixed-order optimization puts constraints on the regulator design, which may not be desirable.

There are commercially available FPGA-based solutions that are aimed at accelerator control and diagnostics [15, 16]. Nevertheless, collaboration is quite common in the accelerator community, so the ELBE installations of the LLRF and BAM actively use a hardware/-software (HW/SW) environment [74, 32, 9, 37] developed at the Deutsches Elektronen-Synchrotron (DESY). This environment is based on the micro telecommunications computing architecture (MTCA). For the sake of using available hardware resources in the most efficient way, the beam-based regulator developed in this work is expected to stick to the existing technology stack, including the use of FPGA devices from Xilinx [78] and the application of a hardware description language, called VHDL [3, 28].

1.3 Motivation and Problem Statement

Based on the state of the art and relevant discussion, the following problems are formulated in order to constitute the motivation for the work presented in this thesis.

The CW operation of an electron linear accelerator opens a possibility to reinterpret the electron beam regulation as a disturbance rejection goal, where the disturbance is based on measured frequency data. This gives rise to formulations of the given regulation problem that take process disturbance explicitly into account. It is known that the frequency components of electron beam noise are directly transferred to the generated photon pulses [36], so applying appropriate compensation is expected to have a positive impact on the achievable time resolution of the pump-probe experiments.

It is thus of interest to study the beam-based regulation from the perspective of explicit disturbance modeling. If a valid disturbance model is established, the issue with the slow actuator could be resolved. That is to say, if the major noise components, e.g. those coming from an RF noise, reside below the actuator bandwidth, the slow actuator response would no longer limit the regulation. At the same time, keeping the model complexity low is preferred, considering the need for the real-time implementation. This circumstance adds modeling constraints that likely render methods that produce high-order models, e.g. fractional-order identification [27], inappropriate for the given task.

Once the valid disturbance model is established, a suitable regulator design must be selected. The design is expected to support the inclusion of so-called colored disturbances whose frequency content could be determined by the established disturbance model. It is also desirable to let the design reflect the actual physical problem, i.e. the minimization of rms fluctuations. Of course, evaluating the performance of the new design with respect to the proportional counterpart is of particular interest.

Moreover, it is important to consider the given RF actuator when designing the beam-based regulator. Related considerations include choosing a suitable interconnection for the overall scheme of the beam-based regulation; examining a possibility to reduce the complexity of the regulator design by omitting the dynamics of the RF actuator; selecting a proper method to apply the regulation signal to control signals present in the RF actuator; analyzing the FPGA-based implementation of the LLRF controller to determine the data types of the control signals—the regulation signal must be formatted correspondingly. Also, the digital logic of the LLRF implementation may have to be extended to accommo-

date the new beam-based functionality.

To implement the designed regulator on an FPGA, a number of issues need to be addressed. In particular, the application of fixed-point data types have to be examined to find the sampling times that can be achieved by a resulting digital circuit. The fixed-point implementation could then be compared to a floating-point one. Considering that the latter is readily available as an intellectual property (IP) [79], such comparison could help make conclusions regarding a trade-off between the circuit speed and additional design labor. Furthermore, if the designed regulator has a state-space form, the issue of matrix-vector multiplication has to be addressed as well. Despite the common IIR filter practice, this interdisciplinary work could investigate alternative solutions, e.g. implementing the state-space regulator using systolic arrays [31].

Therefore, a further set of research goals may be proposed: to investigate the problem of using RF noise data for the purpose of modeling electron beam disturbance; to propose and evaluate a disturbance model-based improvement for a commonly used proportional beam-based regulator; to develop a real-time feasible solution for a high-order beam-based regulator.

1.4 Author's Contributions

The main contribution of the author of the thesis is the design and implementation of a beam-based regulator for the CW linac ELBE. This contribution comprises three parts:

- *Modeling*: Exploiting RF noise for the purpose of modeling an electron beam disturbance [42]. As a result, a dynamical model is created that approximates the frequency content of the noise. The closest known solution is proposed in [27], but targets another application and, thus, does not show the noise propagation to the electron beam. In contrast, the author demonstrates such propagation with the help of a Simulink model that includes the noise and a bunch compressor models.

- *Regulation*: Based on the insight acquired through the modeling, the given regulation problem is reinterpreted as a disturbance rejection goal. Following this, a disturbance model-based regulator is designed [44, 45] that reduces the rms fluctuations of an electron bunch arrival time on CW linacs. The new regulator, which is designed in the context of a so-called $\mathcal{H}_2$ mixed-sensitivity problem, is intended to improve a commonly used proportional method. The improvement is evaluated on the CW linac ELBE [45]. To the best knowledge of the author, this disturbance model-based regulation of a CW linac has not been demonstrated in prior art.

- *Software and hardware implementation*: To enable a real-time feasible application of the designed beam-based regulator, a digital FPGA-based solution is designed and implemented [43] using a hardware description language, called VHDL. Contrary to the common IIR approach [55, 67], the regulator is implemented in its state-space form, and systolic arrays are responsible for corresponding matrix-vector multiplications. Importantly, both fixed- and floating-point implementations are considered, which allows to compare the two from the latency point of view. In order to verify the implementation, a hardware testbench is formed, in which the main FPGA is augmented by an auxiliary one. The latter is designed to transmit predefined stimuli to the former and then check the received response.

1.5 Thesis Outline

Each chapter begins with a summary of the research problem discussed therein. In addition, each chapter of the thesis ends with a section containing concluding remarks pertaining to theoretical and practical results reported in the corresponding chapter. Finally, the last chapter comprises general concluding comments, as well as items for prospective research. In what follows, a summary of each chapter is provided.

Chapter 2

This chapter is devoted to investigating the problem of using RF noise data for the purpose of modeling electron beam disturbance. The investigation is carried out with the help of a specially developed Simulink model.

Chapter 3

The topic of this chapter is beam-based regulation. Specifically, a disturbance model-based improvement for a commonly used proportional regulator is proposed and evaluated on the CW linac ELBE.

Chapter 4

In this chapter, a real-time feasible implementation for a high-order state-space regulator is presented. The digital solution is implemented on a fast FPGA board using VHDL.

2 Exploiting RF Noise for Disturbance Modeling

In this chapter, the problem of exploiting an RF noise for the purpose of modeling an electron beam disturbance is investigated. Special attention is devoted to analyzing the ability of the RF noise to reflect the size and frequency content of a measured electron bunch arrival time noise. The order of a resulting model is also taken into account. The structure of the chapter is as follows. First, the notion of the RF noise is introduced, and related measurement data is analyzed. Then, the measured data is used to create a shaping filter for the RF noise, and a Simulink model is built to simulate a bunch compressor that is perturbed by the shaped RF noise. Lastly, conclusions are drawn regarding the appropriateness of the created shaping filter for the modeling of the electron beam disturbance.

2.1 Analysis of Measured RF Noise Data

A noisy sinusoidal wave can be represented as [13]

$$v(t) = (A + \alpha(t)) \sin(2\pi f_c t + \varphi(t) + \phi_0), \tag{11}$$

where A, f_c and ϕ_0 are the amplitude, frequency and initial phase of a carrier wave, and where $\alpha(t)$ and $\varphi(t)$ are zero-mean random processes denoting the fluctuations of amplitude and phase, respectively. These unwanted fluctuations cause the spectral representation of $v(t)$ to contain a spread of spectral lines, both below and above the carrier wave, see Figure 12.

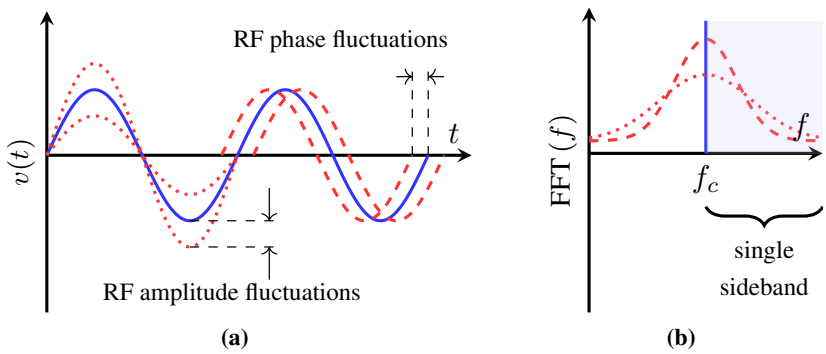

Figure 12: *The effect of contaminating a time domain signal $v(t)$ with RF noise, as observed in **(a)** time and **(b)** frequency domains.*

According to the standard [29], $\alpha(t)$ and $\varphi(t)$ can be represented as one-sided power spectral densities S_a and S_ϕ, respectively. The respective units are $1/\text{Hz}$ and rad^2/Hz. For the purpose of analysis, these densities can be converted to their linear representations $\widetilde{S}_a$ and $\widetilde{S}_\phi$ with units $\%/\sqrt{\text{Hz}}$ and $\text{rad}/\sqrt{\text{Hz}}$, respectively. Figure 13 presents such linear spectral densities that were measured using a phase noise analyzer [19] at the TESLA cavity C4. The measurement was performed during the closed-loop operation of the cavity.

Structurally, the presented frequency data contain two components [42]. These are 1) a random component represented by a spectral profile that decays with certain slopes as the frequency offset increases, and 2) a deterministic component that manifests itself as a number of spurs along that profile. Except for a spur at ca. $750\,\text{kHz}$ that is caused by the undesired $\frac{8}{9}\,\pi$-mode of the TESLA cavity, the majority of the spurs are located below $1\,\text{kHz}$, i.e. in a relatively low frequency range.

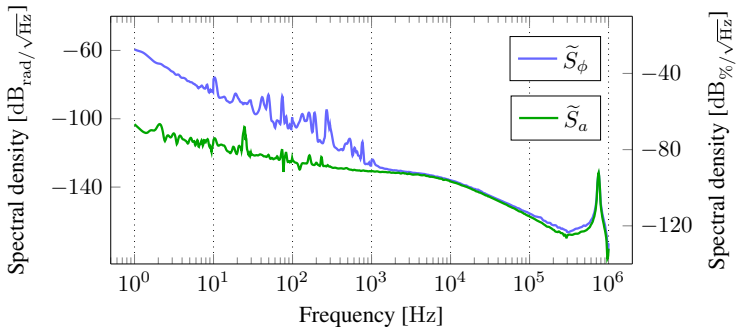

Figure 13: Linear spectral densities $\widetilde{S}_\phi$ and $\widetilde{S}_a$ showing measured noise components of RF field phase and amplitude, respectively. The units are $\mathrm{rad}/\sqrt{\mathrm{Hz}}$ *and* $\%/\sqrt{\mathrm{Hz}}$*, respectively.*

The rms integration of the displayed linear spectral densities produces a result shown in Figure 14. It is interesting to note the allocation of noise. On the one hand, most of the phase noise is concentrated in the low frequency range, and the spurs do not play a significant role, compared to the random component. On the other hand, the amplitude noise is mainly manifested by the 750 kHz spur, and the random component adds little to the overall size. This observation is taken into account during the creation of an appropriate Simulink model. Also note that in this discussion 1 m% signifies 0.001 %.

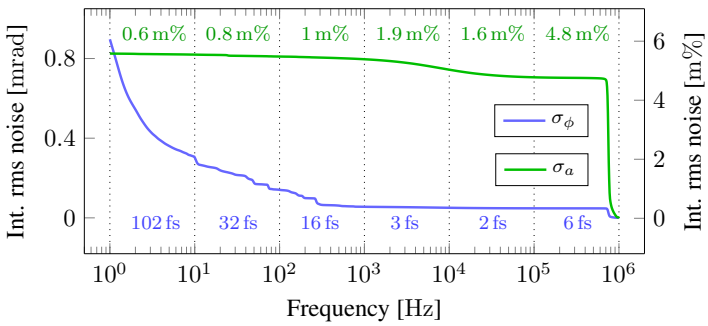

Figure 14: Integrated rms noise of measured RF field amplitude and phase.

2.2 Simulation Model for RF Noise Propagation to Electron Beam

2.2.1 RF Noise Modeling

Based on the discussion in Section 2.1 and related analysis, the modeling of RF noise can be divided into two main stages:

1. Exploiting a linear spectral density to determine the frequency content of data
2. Using rms integration to express the size of this frequency content

The first stage helps to model the frequency content as a dynamical system in s-domain using zeros and poles, whereas the second stage allows adjusting the magnitude response of the modeled dynamical system using its $\mathcal{H}_2$ norm. In this context, the dynamical system is denoted by its transfer function, and the $\mathcal{H}_2$ norm of some transfer function G measures

the rms response of its output, when its input is driven by a white noise excitation [6, 69]. The norm is denoted as

$$\|G\|_2 \triangleq \sqrt{\frac{1}{2\pi}\int_{-\infty}^{\infty} |G(j\omega)|^2 \,\mathrm{d}\omega}, \tag{12}$$

where $|G(j\omega)|$ designates the magnitude frequency response of G evaluated at an angular frequency ω. Following this, it is possible to adjust the $\mathcal{H}_2$ norm of G according to the rms amount of frequency-domain data, i.e.

$$\|G\|_2 \approx \sqrt{\int_{f_1}^{f_2} \left[\widetilde{S}(f)\right]^2 \mathrm{df}}, \tag{13}$$

where $\widetilde{S}(f)$ is a linear spectral density evaluated at a frequency f, and where f_1 and f_2 are the start and end of an integrated frequency interval, respectively. For an electron beam with a bunch repetition rate of 50 kHz, this integrated frequency interval is defined by setting $f_1 = 1$ Hz and $f_2 = 25$ kHz. When applied to the RF noise displayed in Figure 14, the defined frequency interval leaves the size of the phase noise essentially intact, but halves the amplitude noise, see Table 1.

Table 1: Size of integrated rms noise for various linear spectral densities and integration intervals.

	Size of integrated rms noise	
Integration interval	$\widetilde{S}_\phi$	$\widetilde{S}_a$
1 Hz – 1 MHz	0.9 mrad	5.6 m%
1 Hz – 25 kHz	0.9 mrad	2.7 m%

Due to the Nyquist frequency of 25 kHz, there is no reason to model the large 750 kHz spur found in the amplitude noise. The phase noise also does not manifest its spurs that much. So only the random components need be modeled in both cases. For that, the zero-mean random processes $\alpha(t)$ and $\varphi(t)$ are extracted from (11) and treated as colored disturbances, whose frequency contents are determined by shaping filters. These filters are then designed as dynamical systems by choosing the locations of s-domain zeros and poles to reflect the frequency-domain shape of measured data, e.g.

$$G_a(s) = \alpha \frac{(s+z_0)(s+z_1)(s+z_2)}{(s+p_0)(s+p_1)(s+p_2)(s+p_3)}, \tag{14}$$

$$G_\phi(s) = \alpha \frac{(s+z_0)(s+z_1)}{(s+p_0)(s+p_1)(s+p_2)}, \tag{15}$$

where G_a and G_ϕ are dynamical systems describing amplitude and phase noise shaping filters, and where z_i and p_i are zero and pole locations, respectively. Scalar α is used to satisfy (13) when $f_1 = 1$ Hz and $f_2 = 25$ kHz, and s is the Laplace variable. By filling these parameters with values from Table 2, shaping filters G_a and G_ϕ are finally created, see Figure 15. Note that adhering to (13) makes the shaping filters exhibit a magnitude frequency response that is slightly greater than the frequency-domain shape of the data. Consequently, for demonstration purposes, extra parameters $\varepsilon_\phi = 2.5$ and $\varepsilon_a = 0.75$ align the slopes.

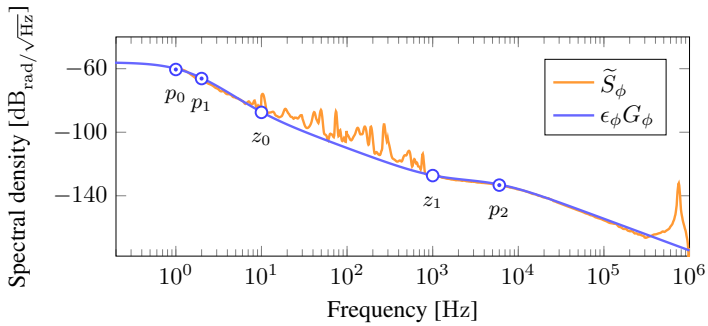

(a)

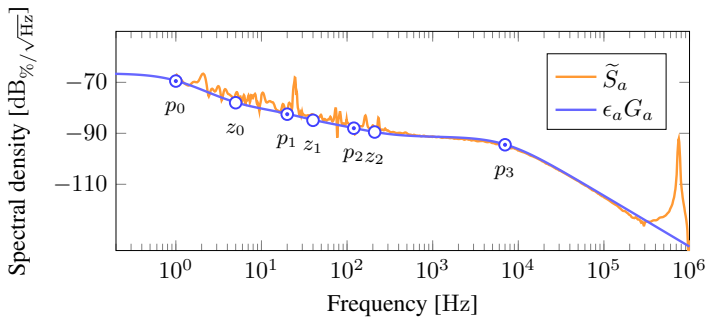

(b)

*Figure 15: Designing RF noise shaping filters to match the measured data of RF field **(a)** phase and **(b)** amplitude.*

Table 2: Modeling parameters for RF noise shaping filters G_a and G_ϕ.

	Value	
Parameter	G_a	G_ϕ
z_0	$2\pi \cdot 5$ rad/s	$2\pi \cdot 10$ rad/s
z_1	$2\pi \cdot 40$ rad/s	$2\pi \cdot 1000$ rad/s
z_2	$2\pi \cdot 210$ rad/s	n/a
p_0	$2\pi \cdot 1$ rad/s	$2\pi \cdot 1$ rad/s
p_1	$2\pi \cdot 20$ rad/s	$2\pi \cdot 2$ rad/s
p_2	$2\pi \cdot 120$ rad/s	$2\pi \cdot 6000$ rad/s
p_3	$2\pi \cdot 7000$ rad/s	n/a
α	0.7767	0.0046
2-norm	0.0027 %	0.0009 rad

2.2.2 Bunch Compressor in Simulink

Figure 16 displays a Simulink model, in which the zero-mean random processes $\alpha(t)$ and $\varphi(t)$ from (11) are modeled as a white Gaussian noise that is filtered by G_a and G_ϕ designed in Section 2.2.1, respectively.

The Gaussian noise is configured to have a unit variance according to [83]

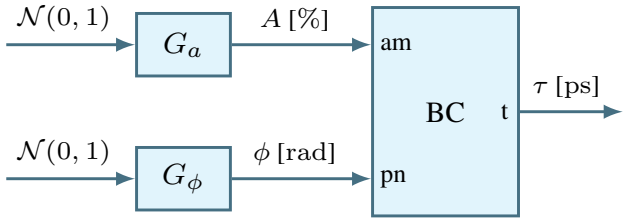

Figure 16: Simulation model to perturb a bunch compressor with RF noise.

$$\sigma^2 = 2\frac{N_0}{2}B, \tag{16}$$

where B is a noise bandwidth in hertz, and where $\frac{N_0}{2}$ is a two-sided power spectral density of the noise in watts. Since only a one-sided spectrum is considered in this work, the constant is doubled. Following this, the unit variance is configured by setting $B = 25\,000$ Hz and $\frac{N_0}{2} = 1$ W. Then, the filtered noise is fed into a bunch compressor model, which implements (9) and (10) in terms of a MATLAB function. The parameters of this bunch compressor are taken from an ELBE configuration and are listed in Table 3. Finally, the whole scheme is sampled at 50 kHz.

Table 3: Bunch compressor parameters for a Simulink model.

Parameter	Value
RF field amplitude A of a chirping SRF cavity	7.33 MV
Off-crest RF field phase ϕ of a chirping SRF cavity	-12 deg
Reference energy E_0 of a magnetic chicane	28 MeV
R_{56} of a magnetic chicane	96 mm

When viewing the results of this simulation in frequency domain, there is a clear alignment between the perturbed output of the bunch compressor and the applied RF noise, see Figure 17. In particular, as the frequency decreases, the bunch compressor output switches from following the RF amplitude to phase noise. Note that for demonstration purposes, G_ϕ is scaled by $\varepsilon_\phi = 208$ and G_a by $\varepsilon_a = 1.35$ to align the slopes. So in general, this simple experiment illustrates the static nature of the bunch compressor. The input noise is propagated to the output with some minor variability depending on the bunch compressor parameters, mostly the phase (see below).

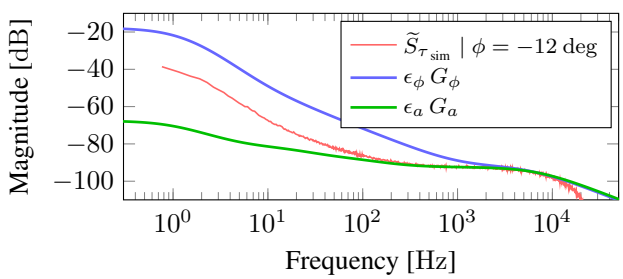

Figure 17: Simulating the impact of RF noise on a bunch compressor.

At the same time, the results of this simulation do not match the measured τ signal, see Figure 18. First, the integrated rms amount of simulated noise is far less than the measured one, namely 12 fs rms compared to 62 fs rms, respectively. Note that for this reason, the simulated data has to be increased by $\psi = 16\,\mathrm{dB}$ to align the slopes of linear spectral densities. Second, there is still a clear mismatch between the slopes below 100 Hz. It is also interesting to note that by decreasing ϕ it is possible to achieve better alignment, but this new ϕ breaks correspondence with the measurement configuration.

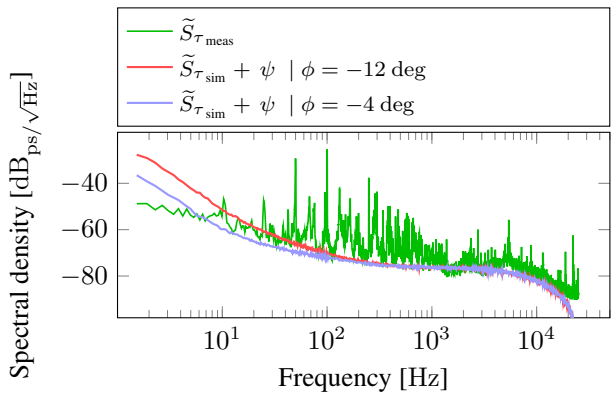

Figure 18: Simulation results of a bunch compressor, when compared to measured electron bunch arrival time data.

The displayed mismatch indicates that the given RF noise alone does not fully reflect the actual noise that is observed on τ. The actual noise has, therefore, a twofold origin, i.e.

- RF noise
- Initial arrival time noise of the passing electron bunches

The second origin is due to upstream noise sources, such as the SRF electron gun. Instead of treating all these noise sources separately, this work focuses on the final noise, which is observed on τ and which accumulates all noise contributions. This not only allows to reflect the actual noise more precisely, but also to keep the order of the resulting model low.

2.3 Conclusions

In this chapter, the problem of using an RF noise for the purpose of modeling an electron beam disturbance was investigated. The models for RF amplitude and phase noise were established and then used in a Simulink model to perturb the model of a bunch compressor. Finally, the results of these simulations were compared to the modeled RF noise and measured bunch arrival time data. This comparison showed two important things, namely

- Bunch compressor is a static system
- Initial arrival time noise constitutes a major contribution to the final noise observed downstream of the bunch compressor

These two aspects significantly impact further modeling that is performed in this thesis. First, the bunch compressor can be modeled as a static beam response matrix, where the

matrix elements are scalars derived from machine measurements. Second, disturbance modeling that is based on the measured RF noise reflects the actual noise neither in size, nor in frequency-domain shape. Simultaneously, such model turns out to be rather high-order, which is undesired for a beam-based regulator, because the high-order solution [44] increases the latency of calculations and may cause numerical instability.

For all of these reasons, it can be concluded that disturbance modeling that is based on the RF noise is inappropriate for the given task. In the rest of this thesis, the disturbance modeling is performed based on the electron bunch arrival time data [45]. Chapter 3 elaborates this new modeling in the context of control system design.

3 Improving Beam-Based Regulation with a Disturbance Model-Based Design

In the following chapter an improvement for a commonly used proportional beam-based regulator is proposed and evaluated. The chapter begins by analyzing the regulation of an electron bunch arrival time, and the common design of the proportional regulator is shown. After that, the given regulation problem is extended with a disturbance model-based design, which is then formulated in the context of the $\mathcal{H}_2$ mixed-sensitivity method. Both designs are evaluated at the continuous-wave linac ELBE in order to draw conclusions regarding the proposed improvement.

3.1 Beam-Based Regulation

According to (9) and (10), where E_0 and R_{56} are static for a given accelerator setting, the arrival time of an electron bunch can be regulated by modulating its energy. Usually, this modulation is performed with the help of an RF actuator, i.e. a control loop that allows setting and stabilizing the amplitude A and phase ϕ of an RF field. To give a concrete example, the RF field control loop, that is responsible for a bunch compressor at ELBE, consists of an SRF cavity and a digital LLRF controller. So from the point of view of the given regulator problem, this means that there are two RF field variables that a beam-based regulator can use to modulate the bunch energy. Yet according to (9), the RF field amplitude A is more linear, than the phase ϕ. Moreover, changing ϕ also changes the bunch compression, which is not desirable in this case. It is therefore reasonable to consider the phase ϕ a constant and define the output of the beam-based regulator in terms of A exclusively, i.e.

$$a = \frac{\Delta A}{A} \cdot 100, \tag{17}$$

where a is a change in percent with respect to the absolute RF field amplitude. In combination with a bunch arrival time monitor, the beam-based regulator extends the bunch compressor schematic by cascaded control loops, i.e. the already existing RF field control loop becomes the so-called inner loop, whereas the added beam-based feedback forms the outer loop, see Figure 19.

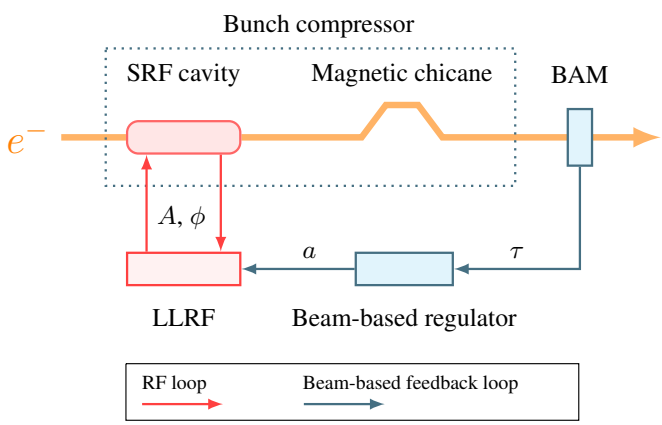

Figure 19: Schematic of a bunch compressor extended by cascaded loops to regulate an electron bunch arrival time.

The corresponding beam-based regulator can be designed by casting the extended bunch compressor to a SISO configuration, where τ is a regulated process variable, and where a is a regulation signal. The bunch compressor then represents a plant, where W_δ converts the control signal a to the absolute RF field amplitude A, and where G_δ and G_τ are (9) and (10), respectively. According to this simple design, the dynamics of the RF actuator are neglected. Instead, the beam-based regulator K acts directly on the bunch compressor in order to compensate an error e, i.e. a negative impact of some unknown disturbance d on the process variable τ, see Figure 20.

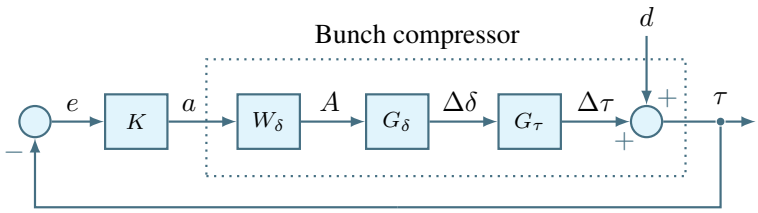

Figure 20: Beam-based regulation cast to a SISO configuration that is based on the first principles derived from a bunch compressor model.

The twofold origin of disturbance d is described in Chapter 2. Here, the origin details are deliberately omitted, and d represents a generalization, e.g. a unit step. To counteract such disturbance, it is straightforward to let K be an inverse of the bunch compressor plant, i.e.

$$K = \gamma G_{BC}^{-1}, \tag{18}$$

where

$$G_{BC} = G_\tau G_\delta W_\delta = \frac{1}{v} R_{56} \frac{eA}{E_0} \cos\phi \, \frac{1}{100}, \tag{19}$$

and where γ is an additional gain to adjust the regulator performance. In fact, the value of G_{BC} can be determined analytically by evaluating (19) with corresponding parameters. Since the ultimate goal is to regulate the ELBE accelerator, G_{BC} is evaluated with ELBE bunch compressor parameters from Table 4. The aim here is to find the amount of variation in τ, given the input parameter $a = 1$. In this case, G_{BC} yields $0.78\,\mathrm{ps}/\%$. Essentially, the resulting scalar plant represents an electron beam response to variations in the RF field. The scalar variant can also be replaced by a matrix, provided there are more beam sensors available. The inverse of such matrix produces a proportional regulator K.

Table 4: Bunch compressor parameters at ELBE.

Parameter	Value
RF field amplitude A of a chirping SRF cavity	7.27 MV
Off-crest RF field phase ϕ of a chirping SRF cavity	-21 deg
Reference energy E_0 of a magnetic chicane	28 MeV
R_{56} of a magnetic chicane	96 mm

Even though the presented analytical formulation of G_{BC} captures the overall concept of the bunch compressor, it is still too simplified to match reality. The phase space of an electron bunch entering the bunch compressor may be far more complicated [41], than a simple ellipse illustrated in Figure 8. This is why, a common engineering practice is to measure the beam response on a real machine, while changing the RF field in a step-wise manner. The ELBE bunch compressor, configured according to Table 4, yields about $0.42\,\mathrm{ps}/\%$ as a result of such measurement, see Figure 21.

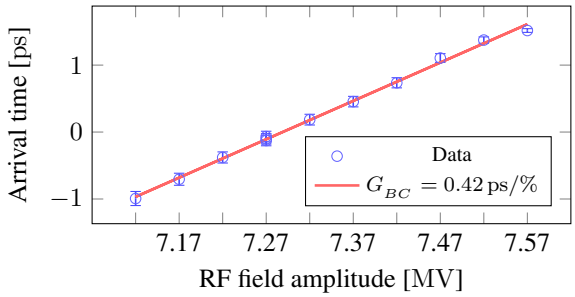

Figure 21: Measuring the response of electron bunch arrival time τ at ELBE, while changing the setpoint of an RF field amplitude, i.e. $A = 7.27$ MV, by steps of 50 kV.

The cross-check of the measured beam response can be performed using the final value theorem [50]. This theorem shows the final value of $e(t)$, i.e. the error of a closed-loop system, as t approaches infinity. So the idea of the cross-check is to first find γ that corresponds to the measured $e(\infty)$. Knowing the value of K that was applied during the measurement, the found γ can be used to determine G_{BC} from (18). Therefore, given the assumption that disturbance d is a unit step, the theorem is defined as

$$e(\infty) = \frac{1}{1 + \lim_{s \to 0} L(s)}, \tag{20}$$

where s is the Laplace variable, and where the limit of a constant open-loop transfer function $L = G_{BC}K$ can be evaluated with the help of (18), yielding

$$\lim_{s \to 0} G_{BC}K = G_{BC}K = \gamma G_{BC} G_{BC}^{-1} = \gamma. \tag{21}$$

By substituting the limit in (20) with (21) $e(\infty)$ can be expressed as a function of γ, i.e.

$$e(\infty) = \frac{1}{1+\gamma}. \tag{22}$$

Then, $e(\infty)$ is redefined as

$$e(\infty) = \frac{\sigma_{\tau_o}}{\sigma_{\tau_i}}, \tag{23}$$

where σ_{τ_i} and σ_{τ_o} denote the integrated rms noise of the electron bunch arrival time measured at ELBE with the proportional feedback off and on, respectively, see Figure 22.

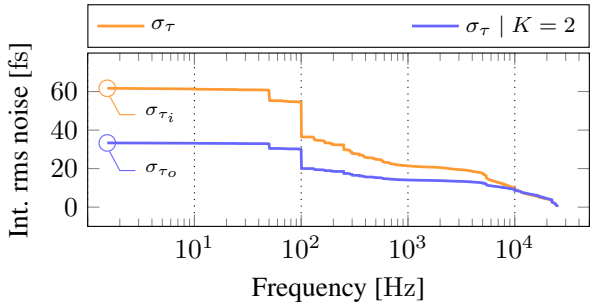

Figure 22: Integrated rms noise of an electron bunch arrival time measured at ELBE with a proportional regulator $K = 2$ off and on.

So by substituting $e(\infty)$ in (22) with (23) γ can be expressed as a function of the measured arrival time ratio, namely

$$\gamma = \frac{\sigma_{\tau_i}}{\sigma_{\tau_o}} - 1. \tag{24}$$

Finally, when evaluated with values from Table 5, (24) and (18) yield $\gamma = 0.88$ and $G_{BC} = 0.44$ ps/%, respectively. The cross-checked value of G_{BC} indicates the validity of the beam response reported earlier.

Table 5: Regulation of an electron beam at ELBE using a proportional regulator.

Parameter	Value	Remark
σ_{τ_i}	62 fs	rms integration range 1 Hz – 25 kHz
σ_{τ_o}	33 fs	rms integration range 1 Hz – 25 kHz
K	2 %/ps	

Choosing $\gamma < 1$ to evaluate G_{BC} is characterized by a need to avoid triggering the degradation of the regulator performance. Specifically, increasing γ on the real machine does not reduce $e(\infty)$ according to an analytical estimation in (22), but rather causes (23) to substantially deviate, see Figure 23. The values of γ that are used during the measurement are derived from (18) by setting $G_{BC} = 0.42$ and $K = \begin{bmatrix} 2 & 4 & 6 & 8 \end{bmatrix}^T$.

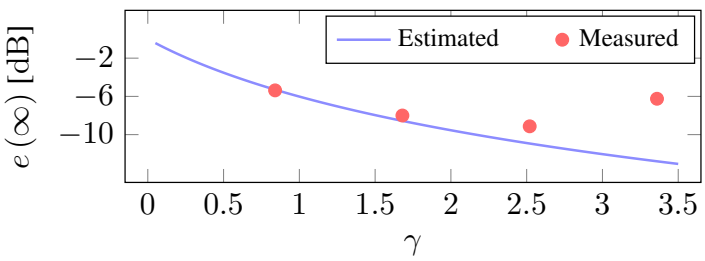

Figure 23: Performance of a set of proportional regulators K, when G_{BC} is tied to the ELBE beam response of 0.42 ps/%, but γ is intentionally varied.

The performance degradation observed on the real machine exposes the principal drawback of proportional regulators, namely the absence of a bandwidth specification. These regulators apply their regulating action across the whole frequency spectrum, which may cause an interference with other control system components, e.g. actuators. In particular, the RF actuator described in Section 1.1.2 exhibits dynamics with a bandwidth of $35\,\mathrm{kHz}$ and a gain margin of $11.6\,\mathrm{dB}$. With no bandwidth specification the proportional regulator becomes part of the actuator dynamics and, thus, relies on the actuator gain margin. So theoretically, setting $\gamma \approx 3.8$ would consume the gain margin completely and turn the system unstable. Yet practically, strong plant oscillations appear above $10\,\mathrm{kHz}$ already when $\gamma \approx 3.36$, see Figure 24. When integrating the resulting rms noise, the strong oscillation above $10\,\mathrm{kHz}$ results in a large integration step, and compared to a less aggressive regulator, this step completely negates the applied regulation effort.

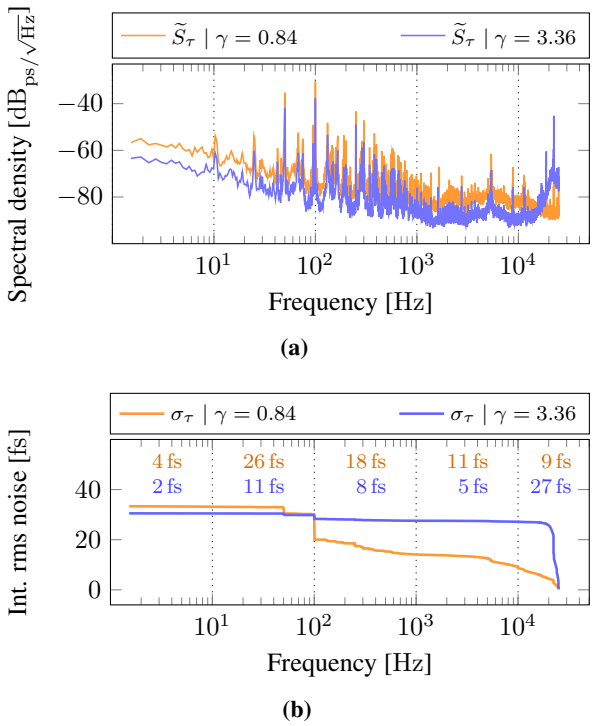

*Figure 24: Regulation of a $50\,\mathrm{kHz}$ electron beam at ELBE using a proportional regulator, when $\gamma \approx 3.36$. **(a)** A pronounced plant oscillation is triggered above $10\,\mathrm{kHz}$, which **(b)** results in a large integration step.*

In this case, an ad hoc solution would be a trade-off between the noise suppression and plant stability. For example, setting $\gamma \approx 2.52$ achieves a suppression of the rms noise by a factor of 3, i.e. only $22\,\mathrm{fs}$ rms noise remains, while causing a moderate plant oscillation, see Figure 25. Even though there is still an integration step, it is not as big as when $\gamma \approx 3.36$. The impact on the final rms noise is thus small.

The displayed trade-off gives rise to the problem of finding a regulation approach that is able to achieve good noise suppression without compromising the plant stability. In comparison to the displayed settings of the proportional regulator, the new approach should perform similarly to $\gamma \approx 0.84$ in the high-frequency range, but preferably better

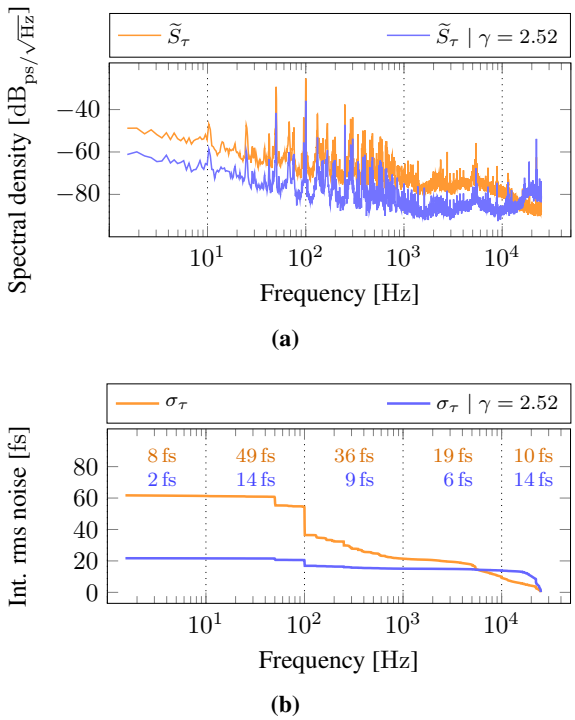

Figure 25: *Regulation of a* 50 kHz *electron beam at ELBE using a proportional regulator.* ***(a)*** *Setting* $\gamma \approx 2.52$ *causes a moderate oscillation above* 10 kHz. ***(b)*** *Nevertheless, the set* γ *allows to suppress the integrated rms noise by a factor of 3.*

than $\gamma \approx 2.52$ in the low-frequency range. Therefore, in this work, the aim is to take the actual noise explicitly into account. This means shifting the focus of attention from the analytical formulation to the size of a concrete disturbance signal. So contrary to the proportional regulator, the new regulator K will try to compensate the impact of a known disturbance d on the process variable τ. Obviously, the updated beam-based regulator will have to ensure

- Proper bandwidth definition in order to decouple the new regulator dynamics from the LLRF loop, i.e. the actuator
- Natural ability to incorporate a dynamical disturbance model inside the regulator design
- Correspondence between the regulator performance criterion and the goal to suppress the rms value of electron beam fluctuations

These requirements are satisfied by employing a disturbance model-based design that is expressed in terms of the $\mathcal{H}_2$ mixed-sensitivity problem [69, 40]. On the one hand, the $\mathcal{H}_2$ regulator design represents a frequency-dependent optimization procedure. On the other hand, the designed regulator is expected not only to stabilize the plant model, but also to minimize the rms fluctuations of the model output. Since the $\mathcal{H}_2$ norm of a model is directly related to the rms value of its output, minimizing such norm matches well the given physical problem.

3.2 Disturbance Model-Based Design

The modeling of disturbance for the new beam-based regulator is based on arrival time data presented in Figure 10. This allows the design to better match the given real-world problem. Consequently, a transfer function G_d is introduced to define the dynamics of a stochastic disturbance d that acts on an electron bunch arrival time τ. That is to say, this disturbance model is interpreted as a filter that shapes a theoretical white noise signal into the frequency content of the measured arrival time data. The rms amount modeled by G_d is adjusted with the help of (13), while setting $f_1 = 1$ Hz and $f_2 = 3.5$ kHz for a 50 kHz electron beam. Choosing 3.5 kHz as the upper integration limit has a couple of reasons. First, the majority of the noise resides below 1 kHz [42], and this can be used as a design constraint. Second, the designed $\mathcal{H}_2$ regulator aims to achieve decoupling from the LLRF dynamics [44], and this is accomplished by targeting a regulation bandwidth of 3.5 kHz, i.e. one order of magnitude lower than the 35 kHz bandwidth of the LLRF. Therefore, by choosing the locations of poles and zeros to reflect the frequency-domain shape of measured electron bunch arrival time noise, the transfer function G_d can be defined as

$$G_d(s) = \alpha \frac{s + z_0}{(s + p_0)(s + p_1)}, \tag{25}$$

where z_0 denotes the location of a zero at 500 rad/s, and where p_0 and p_1 are two pole locations at 50 rad/s and 5000 rad/s, respectively. Scalar $\alpha = 4.2021$ is used to satisfy (13).

Therefore, the norm $\|G_d\|_2$ yields 0.059 ps rms, which is, indeed, the majority of the noise when compared to the overall noise of 0.062 ps rms. Accordingly, $G_d(s)$ represents a specifically scaled second-order dynamical system with a 20 dB/decade roll-off after 1 kHz, see Figure 26.

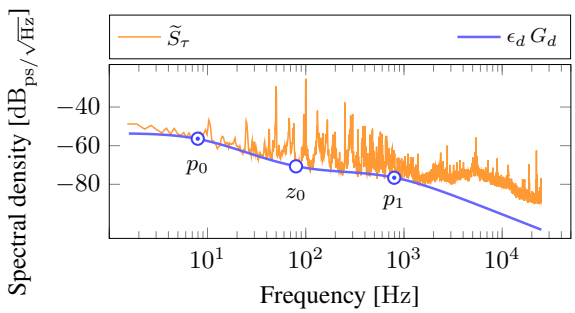

Figure 26: Designing the disturbance model G_d to match the electron bunch arrival time noise up to 1 kHz. An extra parameter $\varepsilon_d = 0.25$ aligns the slopes.

3.2.1 Using $\mathcal{H}_2$ Mixed-Sensitivity Problem

By using G_d as a design specification, the new beam-based regulator K is aimed at reducing the sensitivity of τ to rms perturbations coming from d. Such interpretation enables the formulation of this beam-based regulation in terms of the $\mathcal{H}_2$ mixed-sensitivity problem, see Figure 27.

According to such formulation, models G_d and G_n define the transfer functions of the electron beam disturbance d and the sensor measurement noise n, respectively. In addition, frequency weights W_S and W_{KS} help shaping the regulator performance and produce error signals w_S and w_{KS} that are used by an optimization procedure. Finally, as shown below, a specific bandwidth is defined to decouple the designed regulator from the LLRF

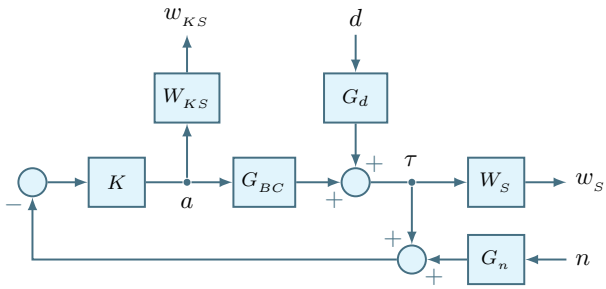

Figure 27: Regulation of an electron bunch arrival time expressed in terms of the $\mathcal{H}_2$ mixed-sensitivity problem.

dynamics. This allows to omit the RF field control loop from the design and continue using G_{BC} as the plant model.

Moreover, by putting G_d into the context of the $\mathcal{H}_2$ mixed-sensitivity problem the τ signal can be expressed as

$$\tau = \underbrace{(1+L)^{-1}}_{S} G_d \, d \,, \tag{26}$$

where again $L = G_{BC}K$ and denotes the open-loop transfer function, and where S is a closed-loop transfer function, called the sensitivity function. Inspection of (26) shows that the sensitivity to disturbance input d can be reduced by properly shaping S in frequency domain, see Figure 28.

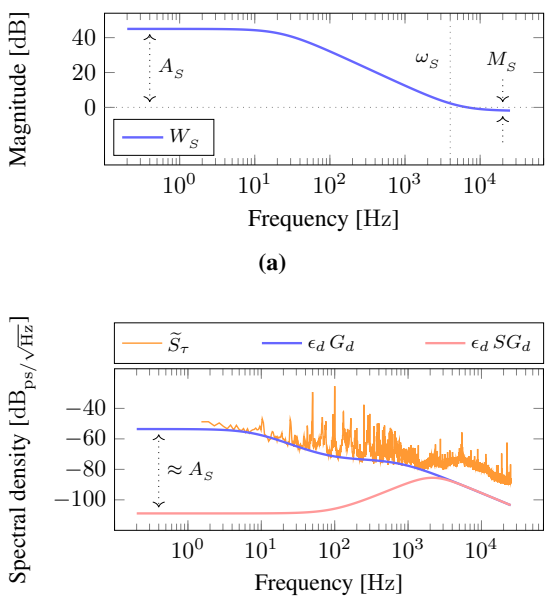

*Figure 28: Shaping the sensitivity function S using **(a)** a frequency weight W_s to **(b)** suppress the disturbance model G_d into its shaped closed-loop counterpart SG_d. For demonstration purposes, the extra parameter $\varepsilon_d = 0.25$ aligns the slopes.*

Specifically, the shaping of S is performed using a frequency weight

$$W_S(s) = \frac{\frac{s}{M_S} + \omega_S}{s + \omega_S A_S}, \tag{27}$$

where $W_S(s)$ is a first-order low-pass filter, and where A_S and M_S define the low- and high-frequency gains, respectively. Parameter ω_S specifies an approximate bandwidth of the designed regulator. A typical guideline [69, 40] is to make S small in the low-frequency range to achieve better disturbance rejection. For this purpose, the low-frequency gain A_S specifies the desired suppression of G_d.

Another relevant closed-loop transfer function is related to the regulating signal a. This signal is generated by the beam-based regulator K as a response to a perturbed electron bunch arrival time τ. Since the generated signal is used to manipulate the amplitude setpoint of the RF cavity field, the goal is to limit the control energy in order to avoid sensitivity to any unmodeled RF dynamics. This is accomplished by shaping a so-called input sensitivity function KS, which represents a link between the disturbance input d and regulating signal a, namely

$$a = KSG_d\, d\,. \tag{28}$$

Similar to the shaping of S, the input sensitivity function KS is shaped using a frequency weight

$$W_{KS}(s) = \frac{s + \omega_{KS} A_{KS}}{\frac{s}{M_{KS}} + \omega_{KS}}, \tag{29}$$

where $W_{KS}(s)$ is a first-order high-pass filter, and where A_{KS} and M_{KS} define the low- and high-frequency gains, respectively. Again, the parameter ω_{KS} is linked to the regulator bandwidth. The main objective is to increase the high-frequency roll-off of the closed-loop transfer function KSG_d by increasing the high-frequency gain M_{KS}. The steeper the roll-off, the less action is applied by the regulator beyond its bandwidth. Meanwhile, the low-frequency range of KSG_d follows the shape of the disturbance model G_d with a magnitude offset defined by G_{BC}^{-1}, see Figure 29.

The sensor measurement noise model G_n is used to regularize a so-called sensor singularity at $\omega = \infty$. The fact is that the optimization procedure assumes that the sensor measurement τ has noise at every frequency, $\omega = \infty$ included. Yet the actual disturbance model G_d is defined by a strictly proper transfer function, such that

$$\omega \to \infty: \quad G_d(j\omega) \to 0. \tag{30}$$

Consequently, to eliminate the singularity, the sensor measurement τ is redefined as $\tau + G_n n$, where G_n is a small non-zero constant. Interestingly, G_n can also be used as an effective bandwidth tuning knob. Together with ω_S and ω_{KS}, this parameter establishes the following regulator tuning procedure

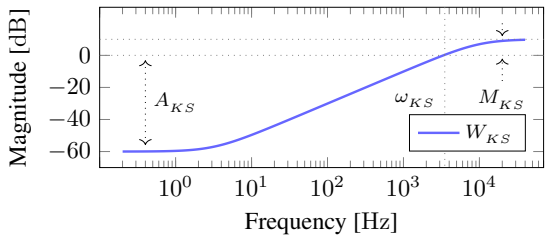

(a)

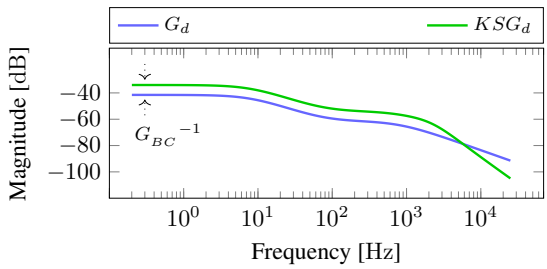

(b)

*Figure 29: Shaping the input sensitivity function KS using **(a)** a frequency weight W_{KS} to **(b)** increase the high-frequency roll-off of a closed-loop transfer function KSG_d.*

1. Set parameters A_S, M_S, A_{KS} and M_{KS} to a desired specification, e.g.

A_S	Desired suppression of low-frequency noise by 60 dB
M_S	Typical selection of 2 dB [69], which is a boundary for the maximum peak magnitude of S at high frequencies
A_{KS}	Typical setting of -100 dB to ensure that the cost function is dominated by A_S at low frequencies [69]
M_{KS}	Initial selection of 2 dB

2. Set parameters ω_S and ω_{KS} about equal to a bandwidth requirement and keep $\omega_S \leq \omega_{KS}$, e.g. $\omega_S = \omega_{KS} = 22\,000$ rad/s ≈ 3.5 kHz

3. Adjust the scalar G_n to align the bandwidth of the complimentary sensitivity function T, see Appendix 1, with the bandwidth requirement

4. Adjust the above parameters to improve correspondence with the desired specification

Following this, Table 6 summarizes design parameters and estimations for a regulator that targets a bandwidth of about 3.5 kHz and a low-frequency noise suppression of roughly 60 dB. Note that during the tuning procedure some of the initial parameter settings changed in order to satisfy the ultimate goals for the bandwidth and suppression.

Table 6: $\mathcal{H}_2$ regulator design parameters and estimations.

Parameter	Value	Remark
G_{BC}	0.42 ps/%	
G_n	0.00018	
A_S	0.0063	-44 dB
M_S	1.26	2 dB
ω_S	$21\,000$ rad/s	3.3 kHz
A_{KS}	0.001	-60 dB
M_{KS}	1.41	3 dB
ω_{KS}	$22\,000$ rad/s	3.5 kHz
$\|G_d\|_2$	0.059 ps	rms amount of expected noise
$\|SG_d\|_2$	0.021 ps	rms amount of residual noise
$\|KSG_d\|_2$	0.14 %	rms amount of regulation effort

Meanwhile, the synthesis of the $\mathcal{H}_2$ regulator is performed by a MATLAB function `h2syn` from the Robust Control Toolbox [4]. As the main input, the function expects a state-space model that resembles an interconnection of the blocks and signals displayed in Figure 27, but with no regulator K to close the loop. As such, the interconnected model features inputs $\begin{bmatrix} d & n & a \end{bmatrix}^T$ and outputs $\begin{bmatrix} w_S & w_{KS} & \tau \end{bmatrix}^T$. This kind of interconnection is usually called a generalized, or augmented, plant. One possible way to prepare the generalized plant is to create the required block interconnection in Simulink, populate these blocks with model data and then use a MATLAB function `linmod` [46] to extract a model of the generalized plant. Since the extracted model is in a state-space form, it is represented by matrices A, B, C and D, which denote the system, input, output and feedforward matrices, respectively. For the purpose of synthesizing the regulator K for this generalized plant, the function `h2syn` attempts to solve an optimization task. It amounts to finding a stabilizing regulator K that is able to minimize the $\mathcal{H}_2$ norm of a transfer function from the disturbance signal d to the error signals w, i.e.

$$\begin{bmatrix} w_S \\ w_{KS} \end{bmatrix} = \begin{bmatrix} W_S S G_d \\ W_{KS} K S G_d \end{bmatrix} d. \tag{31}$$

Along with a state-space model of the synthesized regulator K, the function `h2syn` produces a full-state feedback gain K_u and an observer gain L_x, both returned as matrices. Each of these gains is produced by solving an algebraic Riccati equation, see Appendix 2. In addition, the manual regularization, which is applied with the help of the scalar G_n, allows to switch off the automatic one applied by the function `h2syn`. Finally, the result of the regulator synthesis can be visualized in terms of the most relevant transfer functions, see Figure 30.

As can be seen, the combination of S and KS sensitivity functions, often referred to as S/KS, plays the main role in shaping the desired behavior of the presented $\mathcal{H}_2$ mixed-sensitivity problem. Of course, this shaping adds a certain overhead to the design, because now the plant model is not merely the scalar G_{BC}, but the generalized plant, which includes the second-order disturbance model G_d, as well as the first-order shaping filters W_S and W_{KS}. As a result, there is a plant with four states, which essentially have no physical relation to the real machine and, thus, can not be directly measured. To resolve this issue, the regulator K relies on state observation. That is, the regulator consists of two parts,

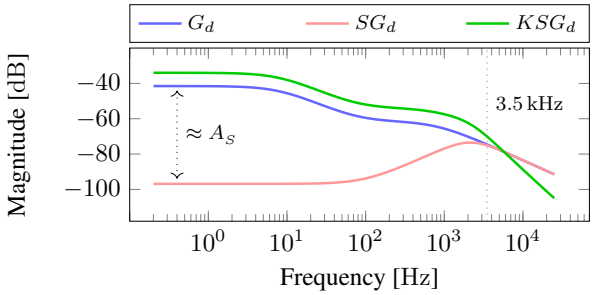

Figure 30: $\mathcal{H}_2$ regulator visualized in terms of its transfer functions. The closed-loop transfer functions SG_d and KSG_d are clearly tailored to the disturbance model G_d.

namely 1) a dynamical state observer system, which estimates the state vector $\widehat{x}$, and 2) the above-mentioned full-state feedback matrix K_u, which uses the estimated states to produce an optimal control signal a. A simplified observer-based structure is illustrated in Figure 31. The matrices A, B and C are derived from the state-space representation of the generalized plant obtained by the function `linmod`.

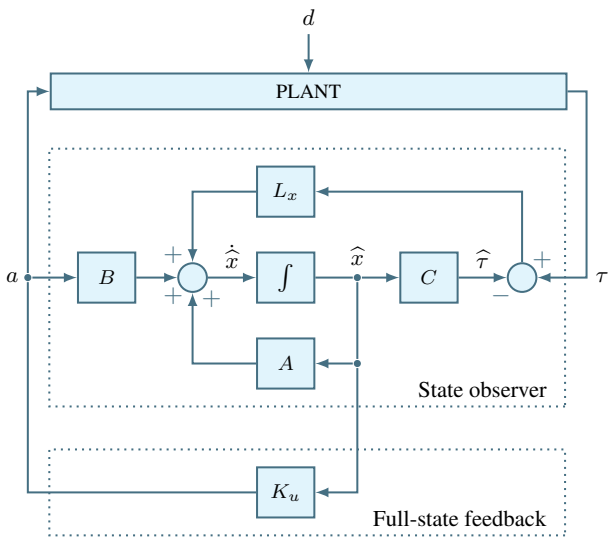

Figure 31: Simplified observer-based structure of the regulator K designed in terms of the $\mathcal{H}_2$ mixed-sensitivity problem.

Mathematically, the displayed observer-based structure is expressed in a state-space form as

$$\dot{\widehat{x}} = A\widehat{x} + Ba + L_x(\tau - C\widehat{x}), \tag{32}$$

$$a = K_u\widehat{x}. \tag{33}$$

Converted to discrete-time forms, (32) and (33) can be implemented on a real-time feasible digital platform. A concrete example is provided in Chapter 4. Such implementation allows to close the loop on the real machine and, thus, validate the concept of the proposed beam-based regulation.

3.2.2 Evaluation at ELBE

To evaluate the performance of the $\mathcal{H}_2$ regulator, measurements on the CW linac ELBE were conducted. The layout of the measurement setup was equivalent to the proportional scheme displayed in Figure 19. Accordingly, the bunch compressor was configured as shown in Table 4. The compressed electron bunches with a bunch charge of 225 pC were then measured by the BAM with a time resolution of 4 fs rms. The $\mathcal{H}_2$ regulator was implemented as described in Chapter 4. Importantly, gain γ, which is displayed in Figure 36, was adjusted during the measurement to improve the regulator performance. The result of this measurement demonstrated that the $\mathcal{H}_2$ regulator was able to achieve good noise suppression without triggering the plant oscillations, see Figure 32. Specifically, the residual noise amounted to 19 fs rms, and the majority of it came from frequency ranges, where the regulator was not active, i.e. above 1 kHz.

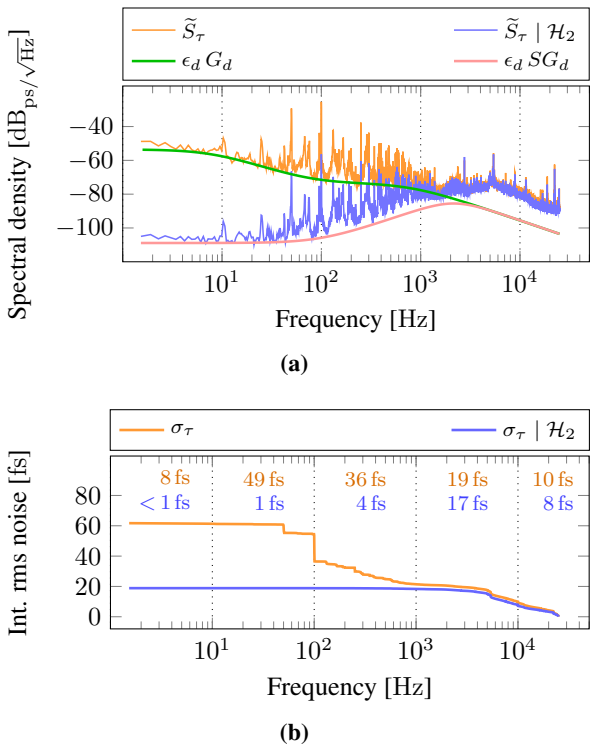

Figure 32: *Regulation of a* 50 kHz *electron beam at ELBE using the* $\mathcal{H}_2$ *regulator.* ***(a)*** *In frequency domain, machine data exhibits correspondence with the model. For demonstration purposes, scalar* $\varepsilon_d = 0.25$ *aligns the slopes.* ***(b)*** *Simultaneously, integrated rms noise data show that the regulator achieves good noise suppression below* 1 kHz.

To better appreciate the achieved regulation of the electron bunch arrival time one can view the result in time domain, see Figure 33. Indeed, large low-frequency fluctuations disappeared as the $\mathcal{H}_2$ regulator counteracted them, whereas small high-frequency ones prevailed. Such is the outcome of applying a band-limited regulator that acts on low-frequency range.

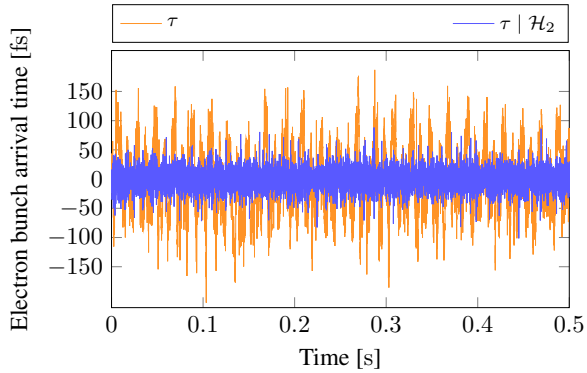

Figure 33: Regulation of a $50\,\mathrm{kHz}$ *electron beam at ELBE as observed in time domain. The beam fluctuations are reduced using the* $\mathcal{H}_2$ *regulator.*

Moreover, the demonstrated correspondence between the model and arrival time data, both in open- and closed-loop cases, also applied to the regulation effort data. That is, the frequency-domain data of the regulating signal a follows the magnitude frequency response of the KSG_d transfer function up to $1\,\mathrm{kHz}$. After this frequency, however, a flattens, as τ ascends to the peak located at approximately $5\,\mathrm{kHz}$. Once τ starts its descent, a can finally demonstrate the designed high-frequency roll-off, see Figure 34. Also, the estimated parameters from Table 6 turn out to be more conservative, than the measurements. That is, the integration of a yields $0.13\,\%$ rms, whereas the estimated parameter is $0.14\,\%$ rms.

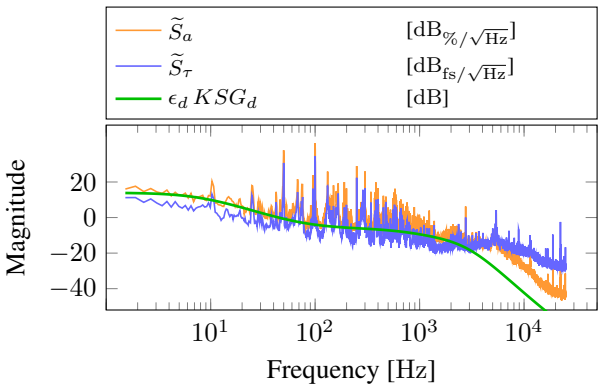

Figure 34: Regulation effort to stabilize a $50\,\mathrm{kHz}$ *electron beam at ELBE using the* $\mathcal{H}_2$ *regulator. For demonstration, scalar* $\varepsilon_d = 0.25$ *aligns* KSG_d *with the slope of* a*.*

Therefore, the absence of the plant oscillations indicates a successful validation of the $\mathcal{H}_2$ regulator with respect to its decoupling from the LLRF dynamics. Compared to the proportional beam-based feedback method, the $\mathcal{H}_2$ regulator not only leaves the high frequencies intact, but also shows superior suppression within its band of frequencies, see Figure 35.

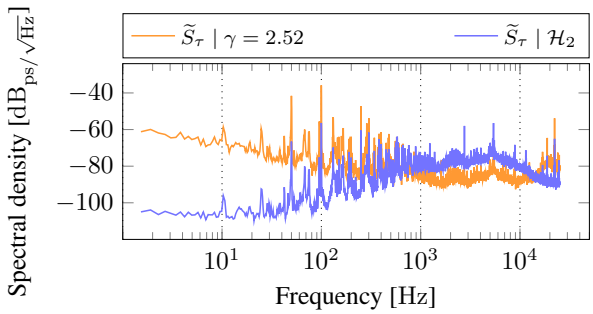

(a)

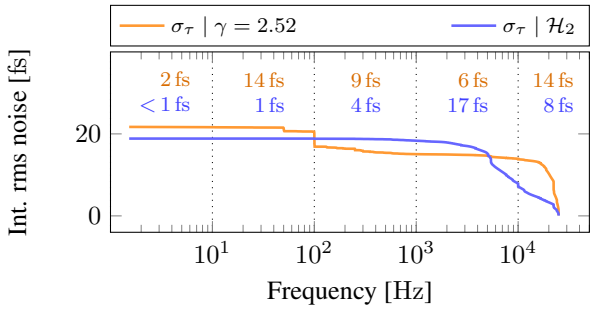

(b)

Figure 35: *Comparing performance between the proportional beam-based feedback method with $\gamma \approx 2.52$ and the $\mathcal{H}_2$ regulator.* ***(a)*** *The frequency domain clearly shows the different behaviors of both regulators depending on the frequency range.* ***(b)*** *This difference can also be seen while examining the band-limited amounts of the integrated rms noise.*

3.3 Conclusions

In this chapter, an improvement for a commonly used proportional beam-based regulator was proposed and evaluated. The improvement was expected to resolve unwanted plant oscillations that are typically caused by the proportional regulator due to its coupling with the dynamics of an RF cavity actuator. To improve the state of the art, a new design was based on a disturbance model derived from measured electron bunch arrival time data. The insight acquired from the data helped determine the right regulation bandwidth, which, in turn, was supposed to facilitate the above-mentioned decoupling. The regulator design was then formulated in the context of an $\mathcal{H}_2$ mixed-sensitivity problem. Finally, the regulator was evaluated on the CW linac ELBE and compared to its proportional counterpart. The corresponding results demonstrated the ability of the designed regulator to achieve the decoupling and, thus, leave the plant stability intact. This also allowed the new regulator to achieve slightly better noise suppression, compared to the proportional case.

Moreover, the designed regulator showed excellent agreement between the model and measurements. The decision taken in Chapter 2 to base the disturbance modeling on the actual beam noise has, therefore, the following favorable consequences

- Residual noise can be estimated in size and frequency-domain shape
- Required regulation effort can be predicted and accounted for

Of course, this result is not possible without a real-time feasible implementation [43] that can efficiently host a high-order state-space regulator and, at the same time, handle a fast beam-based feedback. For this reason, Chapter 4 goes into the details of digital logic and presents the FPGA-based implementation of the designed beam-based regulator.

4 Implementing a High-Order State-Space Regulator for Fast Beam-Based Feedback

In this chapter, the implementation of a high-order state-space regulator for a fast beam-based feedback is presented. To achieve real-time execution, the presented solution is implemented on a powerful FPGA board. The structure of the chapter is as follows. First, the structure of a digital beam-based regulator is shown. Then, integration with the given MTCA.4 digital platform is discussed both from hardware and software perspectives. After that, a more in-depth discussion of a firmware architecture for the beam-based regulator is presented. Specifically, the application of systolic arrays for the purpose of implementing a state-space regulation algorithm is described in detail. Finally, the implemented solution is verified with the help of a specially designed hardware/software testbench.

4.1 Toward Digital Beam-Based Regulator

Discrete-time versions of (32) and (33) are used to implement a beam-based regulator. In the given case, however, G_{BC} is static, so there is a direct feedthrough in the design. This leads to a non-zero matrix D, which has to be taken into account. So mathematically, the full structure is expressed in a discrete-time state-space form as

$$x[k+1] = Ax[k] + Bu[k] + L_x e_x[k], \tag{34}$$
$$u[k] = K_u x[k] + L_u e_u[k], \tag{35}$$

where

$$e_x[k] = y[k] - Cx[k] - Du[k], \tag{36}$$
$$e_u[k] = y[k] - Cx[k] - Du[k-1], \tag{37}$$

where L_u is an observer gain produced by a MATLAB function `h2syn`, and where a feedforward matrix D is derived from a generalized plant. For further details see Section 3.2.1. In order to alleviate an FPGA-based implementation of this structure [43], (34) and (35) are rearranged based on variables $x[k]$, $y[k]$ and $u[k-1]$. This yields a new set of matrices

$$\Theta = A + BK_u - BL_uC - L_xC - L_xDK_u + L_xDL_uC, \tag{38}$$
$$\Upsilon = BL_u + L_x - L_xDL_u, \tag{39}$$
$$\Phi = L_xDL_uD - BL_uD, \tag{40}$$
$$\Xi = K_u - L_uC, \tag{41}$$
$$\Psi = L_u, \tag{42}$$
$$\Omega = L_uD, \tag{43}$$

and since the new matrices can be evaluated offline, (34) and (35) can be rewritten as

$$x[k+1] = \Theta x[k] + \Upsilon y[k] + \Phi u[k-1], \tag{44}$$
$$u[k] = \Xi x[k] + \Psi y[k] - \Omega u[k-1]. \tag{45}$$

Following this, the cascaded control loops displayed in Figure 19 are elaborated with the matrix interconnection of a digital beam-based regulator, see Figure 36. The new matrices are also augmented by gains γ and β, where the former is an additional gain to adjust the regulator performance, whereas the latter is a simple placeholder currently set as $\beta = 1$. Block z^{-1} represents a unit delay that registers signals, such as state x and regulation output u. Finally, note that the implementation part of this work concretizes the actuator device by defining the TESLA cavity C4 as the RF actuator.

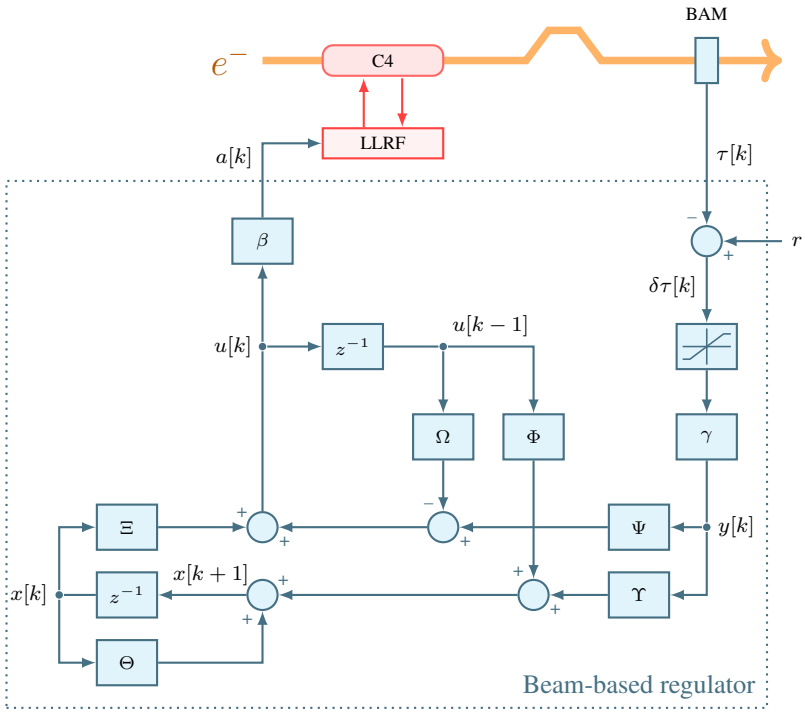

Figure 36: Cascaded control loops of a bunch compressor showing the internal structure of a digital beam-based regulator.

Furthermore, the LLRF control system demonstrated in Figure 4 is extended by a set-point modulation logic M, see Figure 37. The modulation logic is defined as

$$\begin{bmatrix} \Delta r_I \\ \Delta r_Q \end{bmatrix} = \frac{1}{100} \begin{bmatrix} r_I \\ r_Q \end{bmatrix} a, \tag{46}$$

where a denotes a change in the RF field amplitude expressed in percent units, and where r_I and r_Q are the RF field setpoints in I and Q, respectively. Factor $\frac{1}{100}$ is required to convert the amplitude change in percent to a relative error $\frac{\Delta A}{A}$ [33]. This factor could also be applied on the regulator side, but in this case the small resulting number would suffer from underflows caused by the fixed-point data type in use by the LLRF implementation. Specifically, the FPGA-based [71] implementation of the LLRF control system uses fixed-point data type formatted as (1, 18, 10), where the fixed-point format is specified as

$$(\text{sign, word length, word fraction length}). \tag{47}$$

So before sending the regulator output to the LLRF control system, a signal value of, for example, $a = 0.1$ could be factored to $\frac{\Delta A}{A} = 0.001$, which would be very close to the given fixed-point precision of $2^{-10} \approx 9.8 \cdot 10^{-4}$. Consequently, to avoid an immediate loss of precision due to the used data format, this factor is applied last, and on the LLRF side.

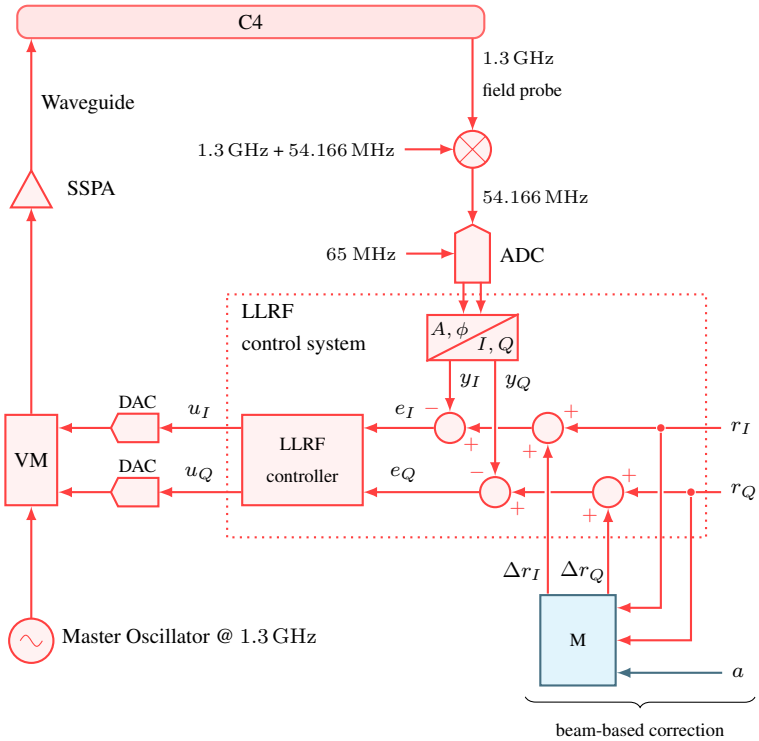

Figure 37: LLRF control system of the ELBE RF station C4, extended by a beam-based setpoint correction.

The displayed LLRF control system is based on the MTCA.4 digital platform. In fact, the BAM sensor uses this digital platform as well. Most importantly, this platform also suits the current implementation, both in terms of hardware and software. So, in this work, it is chosen to stick to the existing technology.

4.2 Integration with MTCA.4 Digital Platform

The fact that the regulator is going to be incorporated into the given digital platform sets a few important conditions: 1) the use of custom FPGA boards and 2) compliance with a firmware framework developed in VHDL [9]. As a result, the regulator implementation is carried out on a specific data processing and telecommunication board, called advanced mezzanine card (AMC) TCK7 [48]. The board features a high-performance FPGA device XC7K420T from Xilinx. To help leveraging the features of this board, the given firmware framework provides support for

- Interfacing with external software through a PCI Express connection
- Communicating with other FPGA boards using low-latency links
- Saving diagnostic data to memory

So there are three major responsibilities of the AMC TCK7 board, namely 1) to receive data from BAM FPGA, 2) process this data and 3) send the result to LLRF FPGA. So while the processing is done inside the XC7K420T chip, the receiving/sending occurs through the low-latency links (LLL) that are driven by 10-Gigabit small form-factor pluggable (SFP) optical transceivers. Measurement signals τ and regulation signals a are transferred via these LLL facilities. Similarly, the initialization of the processing stage happens through a register-based HW/SW internal interface (II) that is driven by the PCI Express (PCIe) connection. This interface is used by external software to set the values of gain matrix elements, setpoints, etc. In addition, the processing stage needs to save diagnostic data. For this reason, a data acquisition (DAQ) facility is used to dump data to double-data rate (DDR) memory. To sum up, Figure 38 illustrates a general block diagram that shows the beam-based regulator in the context of the MTCA.4 hardware environment.

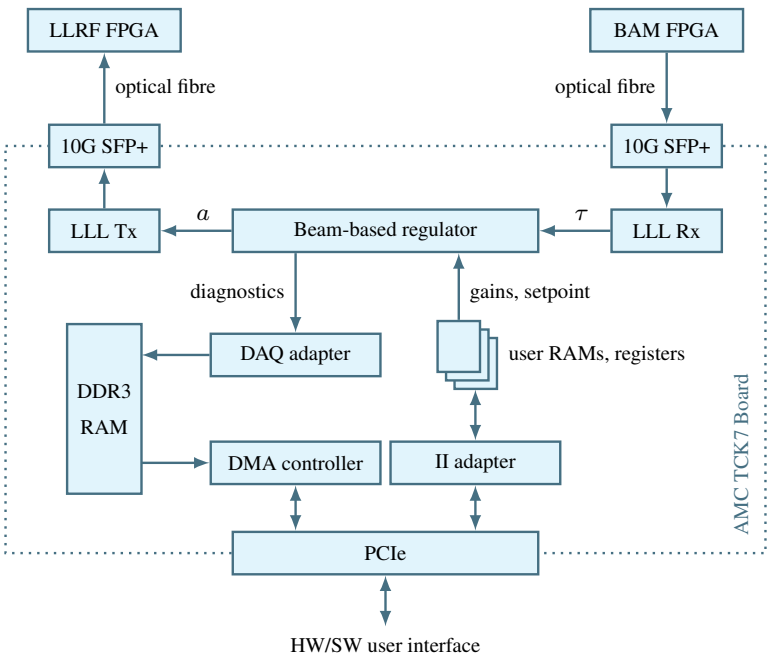

Figure 38: Beam-based regulator implemented in the context of a MTCA.4 hardware environment.

The complexity of the presented hardware system underscores the importance of a software-based user interaction. Hence the necessity to establish a HW/SW interface that is able to facilitate initialization, control and other user related tasks.

4.2.1 Hardware/Software Interface

The MTCA.4 technology uses a special software framework [32] to support the PCIe-based communication between the related hardware and software. Specifically, this framework provides the necessary application programming interface (API) to establish the register-based HW/SW interface. By writing and reading these registers the user is able to interact with the beam-based regulator FPGA, and Figure 39 depicts a basic user interaction as a unified modeling language (UML) use case diagram.

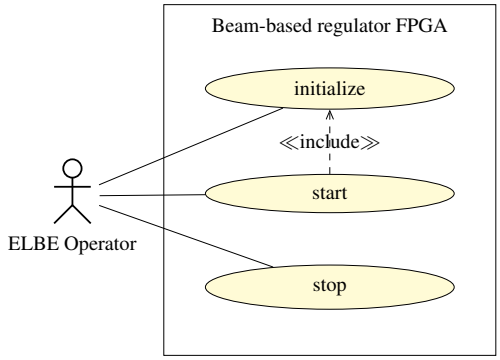

Figure 39: UML use case diagram summarizing user interaction with the FPGA board of a beam-based regulator.

Along with the basic use case to initialize the gain data when the application starts, a more sophisticated variant is to allow updating this data when the regulation is already running. Imagine a use case when the operator wants to tune the gain γ in real time. The difficulty is related to the fact that ELBE is operated in CW mode, so there are no pauses long enough to permit a plain data overwrite. Moreover, it is reasonable to assume that updating the gain data separately, i.e. regardless of the algorithm state as a whole, will lead to erroneous algorithm results. Hence the necessity to update the gains 1) all at once and 2) at a proper time instant. Essentially, the second requirement suggests a hardware-side implementation that is based on a finite-state machine (FSM). In the meantime, the first requirement is fulfilled on the software side by first making a time-consuming write of the entire data from the software to intermediate hardware buffers and then triggering a fast data update on the hardware side. Figure 40 demonstrates this concept with the help of a UML sequence diagram.

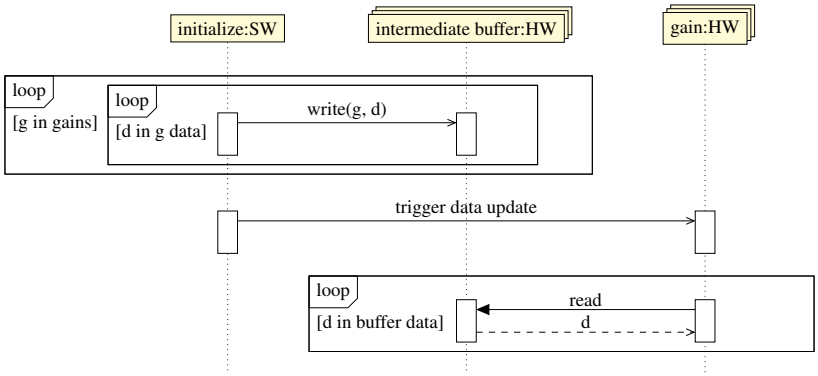

Figure 40: UML sequence diagram demonstrating the concept of (re)initialization of gain data.

The starting and stopping use cases are both based on the manipulation of the same flag to enable feedback data propagation to the regulation algorithm. This one-bit flag, called CTL_ENA, is set to 1 to enable regulation. Fundamentally, this defines an event-driven behavior of the algorithm implementation, i.e. when the algorithm receives no data, the regulation idles, see Figure 41. This is true for both the $\mathcal{H}_2$ and proportional cases.

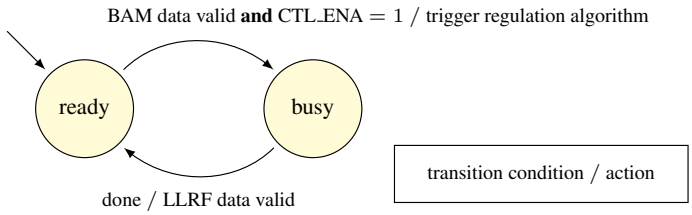

Figure 41: State diagram showing the effect of CTL_ENA flag on regulator state transitions.

Another important flag is responsible for the selection of a beam-based regulator during runtime. Since the aim is to compare the performance of the $\mathcal{H}_2$ and proportional regulators, then a one-bit CTL_SEL flag enables the necessary selection. Together with other control-related registers, CTL_SEL and CTL_ENA form the essential part of the HW/SW interface, see Table 7.

Table 7: Registers of a hardware/software interface for a beam-based regulator.

Name	Width	Count	R/W	Description
CTL_H2_GAIN_X2DX	18	16	R/W	Interm. buffer for Θ
CTL_H2_GAIN_Y2DX	18	4	R/W	Interm. buffer for Υ
CTL_H2_GAIN_IU2DX	18	4	R/W	Interm. buffer for Φ
CTL_H2_GAIN_X2U	18	4	R/W	Interm. buffer for Ξ
CTL_H2_GAIN_Y2U	18	1	R/W	Interm. buffer for Ψ
CTL_H2_GAIN_IU2U	18	1	R/W	Interm. buffer for Ω
CTL_H2_GAIN_U2P	18	1	R/W	Interm. buffer for β
CTL_H2_GAIN_P2Y	18	1	R/W	Interm. buffer for γ
CTL_H2_GAINS_UPD_TRG	1	1	R/W	Trigger to update gains
CTL_H2_STATUS	32	1	R	Status of algorithm
CTL_P_GAIN	18	1	R/W	Proportional gain K_p
CTL_REF	25	1	R/W	Reference signal r
CTL_LIM	25	1	R/W	Limit $\delta\tau_{lim}$ for signal $\delta\tau$
CTL_SEL	1	1	R/W	Selection of regulators
CTL_ENA	1	1	R/W	Enable regulation
DAQ_ENA	1	1	R/W	Enable DAQ
LLL_RX_STATUS	1	1	R	Receiver link status
LLL_TX_STATUS	1	1	R	Transmitter link status
CLK_FREQ	32	3	R	Clock counters

The displayed widths of signals and gains adhere to a custom fixed-point data format. This format is derived by analyzing computational resources available on the given FPGA chip.

4.2.2 Fixed-Point Analysis of Regulator Signals and Gains

An efficient implementation of (44) and (45) requires a design that uses specialized circuits provided by an FPGA, namely digital signal processor (DSP) slices. These high-speed circuits support a number of mathematical functions, including multiplication and addition, and therefore can accelerate a compute-intensive design. According to a data sheet [78], the XC7K420T device features 1680 DSP slices, where each DSP48E1 slice [77] contains a

pre-adder, a 25×18 multiplier, an adder, and an accumulator. Consequently, the 25- and 18-bit widths of the multiplier operands are employed to differentiate between two types of data in the current design:

- signals flowing through the regulator, e.g. from $y[k]$ to $u[k]$
- gain matrix values that modify the signals

The signals and gains are assigned to 25-bit and 18-bit words, respectively, thus prioritizing the precision of the signal data. Apart from the precision, the 25-bit signal word needs to allocate enough bits for the integer part to avoid overflows inside the regulator. This issue is addressed by defining

$$|a_{max}| \approx 1, \tag{48}$$

i.e. the maximum magnitude of the regulation signal a is limited to about $1\,\%$. As demonstrated in Section 3.2.2, this amount of regulation effort is sufficient to achieve good noise suppression. Otherwise, a considerable action taken by the regulator can result in a drastic change of the signal driving the cavity, which, in turn, has a high probability to trigger the ELBE protection system to switch off the accelerator. It is therefore reasonable to limit the regulation signal. To enable such limitation though, the allowed maximum deviation of the BAM sensor output should be close to

$$|\delta\tau_{max}| \approx G_{BC}\,|a_{max}| \approx 0.42, \tag{49}$$

given $G_{BC} = 0.42\,\mathrm{ps}/\%$. For this reason, the block diagram illustrated in Figure 36 features a saturation block, which implements

$$\delta\tau = \begin{cases} \delta\tau, & \text{if } \delta\tau < \delta\tau_{lim} \\ \delta\tau_{lim}, & \text{otherwise} \end{cases}, \tag{50}$$

where $\delta\tau_{lim} = 0.5$. Therefore, when $\gamma = 1$, one bit should be enough to represent the integer part of the signal. To allow experimental variation in γ, e.g. from 1 to 10, four bits are allocated, and, thus, according to the format specified in (47) the signal data type becomes (1, 25, 20).

In contrast, the fixed-point data type for gains is derived by examining the magnitudes of values stored in (38)–(43). In this context, consider the 4th-order digital $\mathcal{H}_2$ regulator

$$\Theta = \begin{bmatrix} 0.6930 & -0.2026 & 0.0751 & -0.0446 \\ 0.0034 & 0.9941 & 0.0023 & -0.0013 \\ 0.0193 & 0.0177 & 0.9905 & 0.0041 \\ -0.3269 & -0.4181 & -0.3098 & 0.7213 \end{bmatrix},$$

$$\Xi = \begin{bmatrix} -0.6539 & -0.8361 & -0.6196 & 0.3683 \end{bmatrix},$$

$$\Upsilon = \begin{bmatrix} -0.3607 \\ -0.0108 \\ -0.4669 \\ 0.2974 \end{bmatrix}, \qquad \Phi = \begin{bmatrix} -0.0303 \\ -9.0993 \cdot 10^{-4} \\ 0.0028 \\ 0.1249 \end{bmatrix},$$

$$\Psi = 0.5948 \ , \qquad \Omega = -0.2498 \ .$$

Depending on the magnitude range of a particular matrix, the gain data type can vary its precision. For example, the maximum magnitude among the matrix values constituting the gain Θ is 0.9941. Hence, zero bits are assigned to the integer part, one bit represents the sign, and 17 bits can be allocated to the fraction part, thus yielding a precision of $2^{-17} = 7.6294 \cdot 10^{-6}$. Following this, Table 8 displays various fixed-point data types assigned to the regulator matrices.

Table 8: Gain matrices with value magnitude ranges and assigned fixed-point data types.

Gain	Min. magnitude	Max. magnitude	Fixed-point data type
Θ	-0.0013	0.9941	(1, 18, 17)
Ξ	0.3683	-0.8361	(1, 18, 17)
Υ	-0.0108	-0.4669	(1, 18, 17)
Φ	$-9.0993 \cdot 10^{-4}$	0.1249	(1, 18, 17)
Ψ	0.5948	0.5948	(1, 18, 17)
Ω	-0.2498	-0.2498	(1, 18, 17)
γ	1	1	(1, 18, 13)
β	1	1	(1, 18, 13)

The data type of γ is chosen as (1, 18, 13) to enable the above-mentioned experimental tuning. Likewise the data type of β, even though there are no plans at the moment to change it from its default value 1. Also, the BAM and LLRF signals have fixed-point data types (0, 18, 15) and (1, 18, 10), respectively, so the regulator implementation must perform proper conversions when receiving or sending low-latency link data.

The described usage of DSP48E1 circuits to perform mathematical operations, such as multiplication, represents integration with the given hardware on the lowest level of this implementation. Meanwhile, the highest level requires integration as well. This time, with the given VHDL firmware framework.

4.2.3 Top-Level Architecture of VHDL Firmware Framework

The top-level architecture of the VHDL firmware framework divides on-chip logic into board and application compartments. The former manages the board specific features, including low-level communication interfaces and clock generation, whereas the latter defines the application logic. Both compartments are then united inside a top level VHDL entity. Figure 42 depicts such architecture as a general block diagram and uses color codes to demarcate new regulator logic from the given framework.

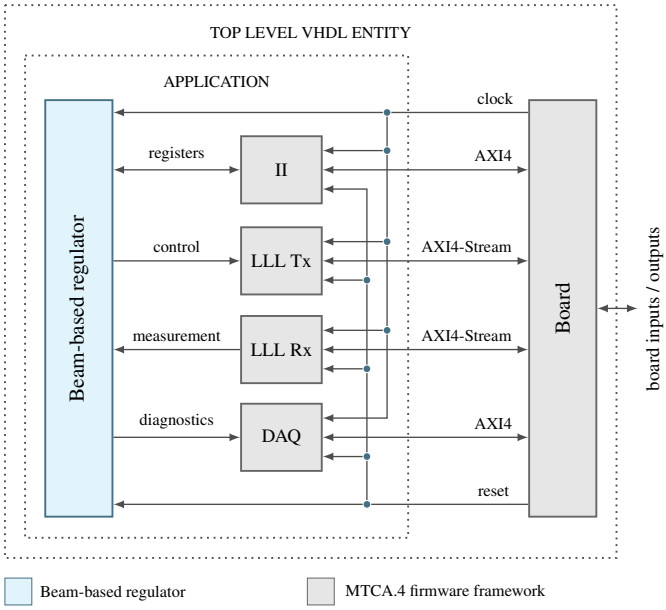

Figure 42: Structure of a top-level VHDL entity as defined by the given VHDL firmware framework.

The presented hardware/software analysis is sufficient to start the implementation. In this work, the aim is to keep new hardware logic as generic as possible. That is to say, most of new VHDL code is not bound to any specific technology and could, in principle, be ported to other digital platforms.

4.3 Using DSP48E1 for Proportional Regulator

The new regulator logic, which is demarcated in Figure 42, contains implementations of both $\mathcal{H}_2$ and proportional regulators. During runtime, the selection of one of them is carried out with the help of the one-bit register CTL_SEL, which is listed in Table 7. This register controls the multiplexing of data streams that feed the regulators, see Figure 43. Since the regulators are defined as event-driven, a properly directed data stream activates the right regulator.

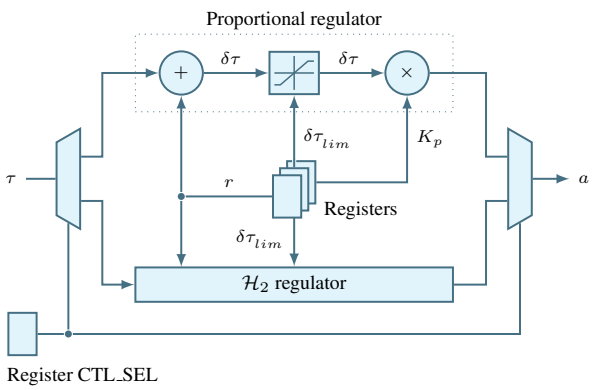

Figure 43: Register CTL_SEL is responsible for the selection of regulators.

The presented block diagram reveals the internal structure of the implemented proportional regulator. This structure contains an adder, a saturation block, and a multiplier. The adder is configured to add a negated version of BAM signal τ to reference signal r. The produced error signal $\delta\tau$ is then limited according to (50). Finally, the error is multiplied by the proportional gain K_p. From the implementation point of view, the necessary multiplication logic is implemented in terms of a DSP48E1 slice that is inferred from a corresponding VHDL code, see Listing 1. The use of signed values in the displayed VHDL source is recommended by the user guide of the DSP48E1 slice [77]. Functions **resize** and **shift_right**, as well as type **signed**, come from the VHDL *numeric_std* package [28].

Listing 1: Inference of a DSP48E1 slice for the multiplication of two signal values.

```
--! register arguments
if  i.data_valid = '1' and reg.data_rdy = '1' then
    v.data := signed(i.data);
    v.gain := signed(i.gain);
end if;

--! perform multiplication (infers DSP48E1)
v.mul := reg.gain * reg.data;

--! extract product data adhering to data format
v.prod := resize(
    shift_right(reg.mul, gain_frac_size),
    fxp_data_size
);
```

4.4 State-Space Implementation for $\mathcal{H}_2$ Regulator

DSP48E1 slices build the foundation of this state-space implementation. Yet compared to the simple proportional algorithm described earlier, the state-space formalism involves matrix-vector multiplications, hence a more complex digital circuit is required. Here, systolic arrays are used due to their ability to execute these mathematical operations in a massively parallel manner.

4.4.1 Systolic Array Structure

Systolic arrays are grid-like interconnections of data processing elements, or nodes, that are driven by data to perform some specific uniform operation. In particular, a properly organized data flow can drive an array of multiply-accumulate nodes, or MACs, in order to implement a matrix-vector multiplication. Figure 44 demonstrates an example of a node interconnection that computes the product $c = Ab$, where b and c are 2×1 input and output vectors, respectively, and where A is a 2×2 matrix. In this straightforward systolic implementation the number of nodes corresponds to the size of the output vector c. This allows to parallelize the computation of individual output vector elements and to keep the computation results local to the nodes. Consequently, when the data finishes propagating through this interconnection in a wave-like manner, the nodes will store a fully computed output vector.

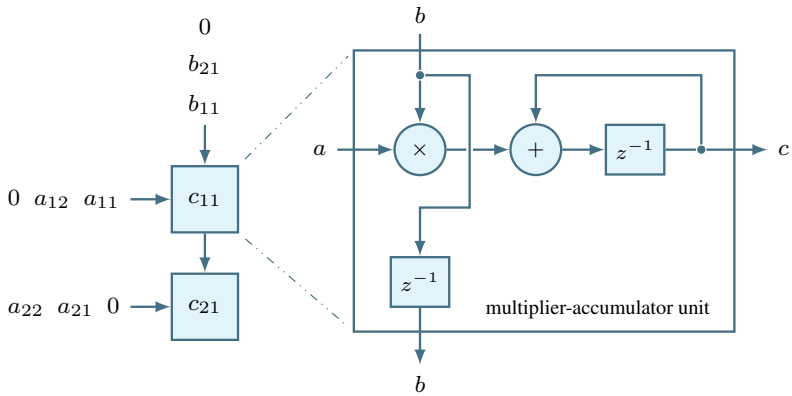

Figure 44: Example structure of a systolic array for multiplying a 2×1 vector b by a 2×2 matrix A. The zero padding of data is explained later in the text.

In fact, a DSP48E1 slice can be configured to perform the multiply-accumulate operation in the form of $a \cdot b + c$, where a and b are 25-bit and 18-bit signals, respectively, and where accumulation with c is sign-extended to 48 bits. Notably, by adhering to these signal widths, a MAC unit can be mapped to a single DSP slice on an FPGA, thus leading to the optimal use of FPGA resources. A VHDL code that is able to infer such a slice is displayed in Listing 2.

Listing 2: Inference of a DSP48E1 slice for a multiply-accumulate operation.

```
--! register arguments
if  i.data_valid = '1' and reg.data_rdy = '1' then
    v.gain  := signed(i.gain);
    v.data  := signed(i.data);
    v.acc_i := shift_left(
        resize(signed(i.acc), acc_size),
        gain_frac_size
    );
end if;

--! multiply data by gain
v.mul := reg.gain * reg.data;

--! sign-extend multiplication result to accumulator width
v.mul_ext := resize(reg.mul, acc_size);

--! accumulate result (infers DSP48E1)
v.acc_o := reg.acc_i + reg.mul_ext;

--! extract mac result data adhering to data format
v.mac := resize(
    shift_right(reg.acc_o, gain_frac_size),
    fxp_data_size
);
```

Still, the operation of systolic arrays relies on a properly organized data flow. This includes not only directing the right data to the right node, but also formatting this data in the right manner—note how the data in Figure 44 is padded with zeros. The padding ensures correct computation inside the nodes, but also increases the size of a single data flow to

$$\text{data flow size} = \text{gain row size} + \text{gain column size} - 1. \tag{51}$$

Following this, a specially designed circuit is required to drive the systolic arrays with data.

4.4.2 Data Flow To Drive Systolic Arrays

In this work, a specially developed digital circuit, which is responsible for a data flow to drive systolic arrays, is called a data channel, and multiple data channels compose a data stream. As shown in Figure 45, this circuit plays a central role in a VHDL entity, called gain, that is designed as part of this work to manage the regulator gains.

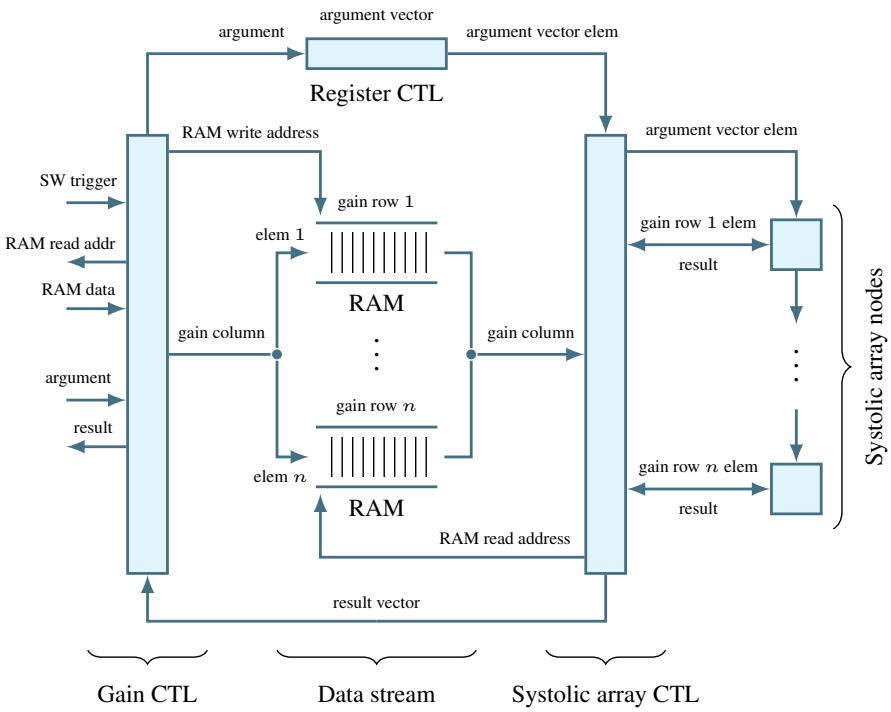

Figure 45: Gain entity schematic showing internal data flows.

Inside the data stream circuit, the data is structured based on its type. The gain is treated as a two-dimensional matrix and is organized into matrix rows. These rows are represented by separate data channels implemented as RAMs. Such organization facilitates the gain data throughput, because it allows to write or read an entire matrix column in a single clock cycle. This also places a requirement on the software to write the gain data to intermediate RAM buffers in a column-major order. After a software trigger, the gain controller will rely on the proper format of the intermediate data in order to initialize the internal data channels column by column. Unlike the gain, the signal is placed into

a register-based memory. Again, this allows to register an incoming signal, i.e. the gain argument, in a single clock cycle. Along with the gain column, the signal vector element is then fed into the systolic array to perform the necessary computation. Once the computation is over, the results from each systolic array node are assembled into a result vector which is then propagated to the gain entity output.

In the context of this regulation algorithm, the gain entity has two main functions: 1) (re)initialize the data of a certain gain, and 2) apply this gain to incoming argument data. Clearly, both functions rely on data coming from the level of application, so it is reasonable to expand the data flow concept and model the application of the beam-based regulator accordingly.

4.4.3 Application Modeling in Terms of Data Flows

Application data can be divided into three main flows, namely initialization, regulation and diagnostics:

Initialization Before the algorithm of this regulator can be run, the initialization of gain data needs to be carried out. Since this data is transferred from CPU software, the data values are received by the firmware through II communication. In fact, a single gain can be represented by a matrix with multiple values, so a receiver should be RAM-based. According to the discussion in Section 4.2, this RAM is expected to serve as an intermediate buffer that is first written by the software and then, after a software trigger, read by actual gain logic. Once such initialization is complete, the regulation data flow becomes enabled.

Regulation The regulation data flow starts from the reception of a BAM sensor measurement coming over a dedicated low-latency link. Provided the regulator algorithm is not busy at the moment and the regulation is enabled by the user, see Figure 41, the new measurement triggers the computation of a new control signal. Otherwise, the received measurement is dropped. Such behavior ensures that the algorithm always sees up-to-date measurements. When the algorithm is indeed triggered, the data starts flowing to gains and further to sums. Once the regulation algorithm is complete, the new control signal is transmitted over a dedicated low-latency link to the LLRF actuator.

Diagnostics The diagnostics saves the regulation data, including the BAM sensor measurements and the corresponding control signals. Importantly, the BAM data is saved even if the regulator is disabled. This allows to diagnose the open-loop behavior of the system.

To sum up, Figure 46 illustrates a functional schematic of the beam-based application. Note that the illustrated firmware blocks belong to the new regulator logic, hence the corresponding color code. In this context, the additional Rx and Tx blocks act as adapters between the framework and the regulator in order to to establish a properly registered ready/valid handshake—a flow control technique [14] that is used throughout the entire regulator logic. Note also that for the sake of brevity the diagram omits the transformation from signal $\tau[k]$ to $y[k]$ and from $u[k]$ to $a[k]$. Finally, the diagram makes the central role of a finite-state machine obvious.

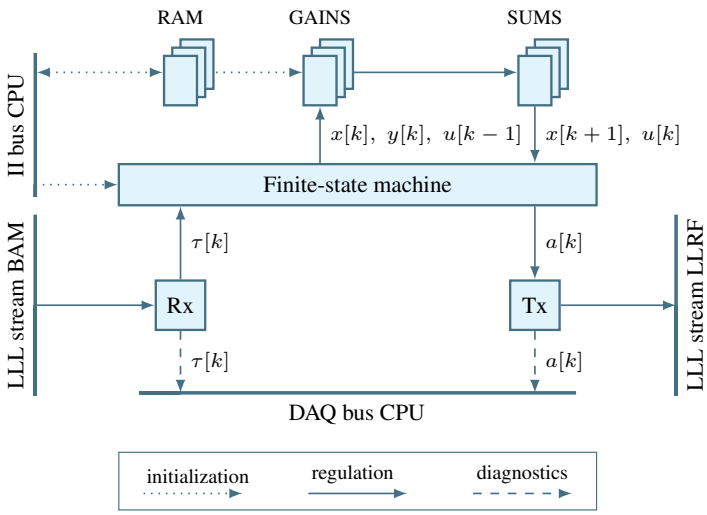

Figure 46: Schematic illustrating the main data flows inside the application of a beam-based regulator.

4.4.4 Finite-State Machine

One of the reasons for involving an FSM to manage the regulator algorithm is inspired by the analogy between a discrete-time state-space form of the regulator and a Mealy state machine [12]. Specifically, a hardware implementation of the Mealy machine is composed of combinational and sequential logic blocks. The combinational logic takes the current state together with input and computes the next state and output. The next state is then saved, or registered, by the sequential logic. The process repeats during the next iteration. Accordingly, Figure 47 depicts an FSM of the state-space regulator, where sequential logic block z^{-1} registers the regulator state, and where combinational logic blocks $f(\cdot)$ and $g(\cdot)$ implement expressions (44) and (45), respectively.

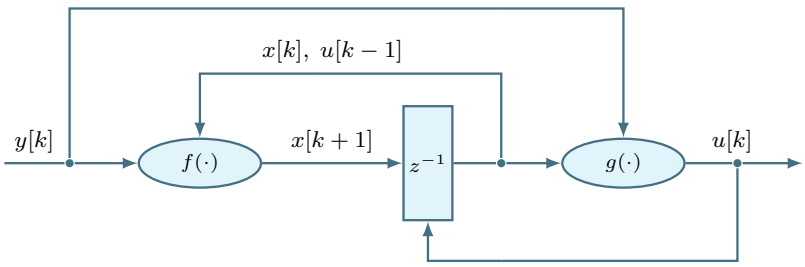

Figure 47: Discrete-time state-space regulator visualized as a Mealy FSM.

Unfolding this FSM approach, Figure 48 demonstrates a state diagram that captures the essential parts of the regulator behavior. Once the regulation algorithm is triggered, $f(\cdot)$ and $g(\cdot)$ will be executed in parallel. Yet $f(\cdot)$ will take significant time to process its longest operation, i.e. Θx. So it is possible to get the result of $g(\cdot)$ and initiate the sending of LLRF data before $f(\cdot)$ completes. Hence, a busy state with two stages.

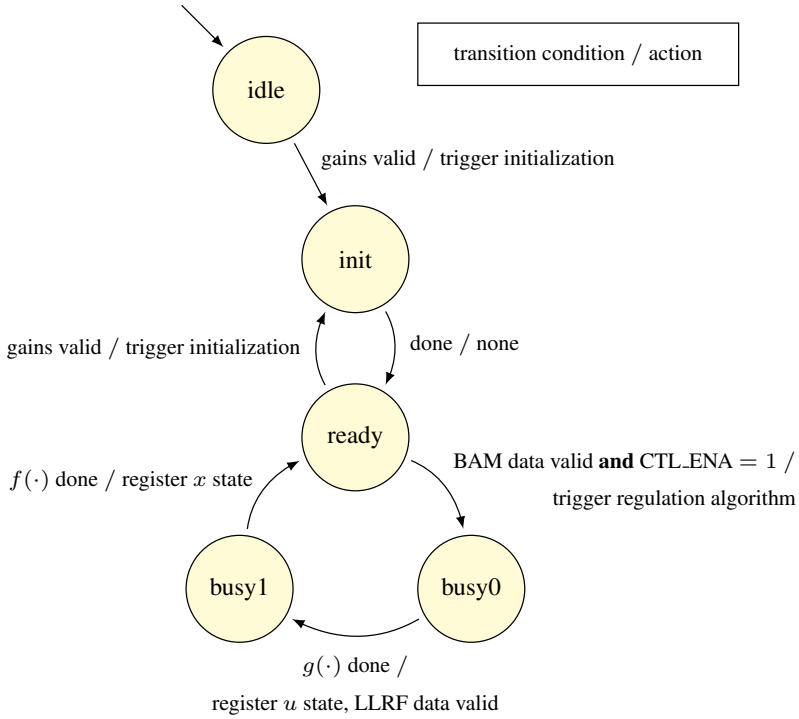

Figure 48: State diagram showing the operation of a beam-based regulator FSM.

Undoubtedly, the presented data flow architecture introduces some amount of overhead into the implementation. This is especially true for the data stream circuit that features data padding. Therefore, evaluation of both algorithm latency and the usage of FPGA resources is of utmost priority.

4.4.5 Evaluation of Latency and Usage of FPGA Resources

The latency of the presented implementation is evaluated by measuring simulation time that the algorithm spends in the busy states. Given a clock frequency of $240\,\mathrm{MHz}$, this latency shows the time that the algorithm needs in order to respond to an incoming BAM measurement. Moreover, the fixed-point implementation is compared to a floating-point one. The latter uses a 32-bit single precision data type [30] and relies on an IP from Xilinx [79] to perform multiplication and addition. Figure 49 shows such comparison. Note how the timing of low-order implementations is dominated by the latency of the data flow architecture.

In addition, there is a difference between the latency of fixed- and floating-point implementations. This comes from the fact that these implementations use different amounts of FPGA resources, namely DSP48E1 slices, in order to perform multiplication and addition. For example, a fixed-point sum represents a trivial element-wise summation of argument vectors and, thus, does not need DSP resources. On the contrary, its floating-point counterpart uses two slices for one sum unit, see Table 9.

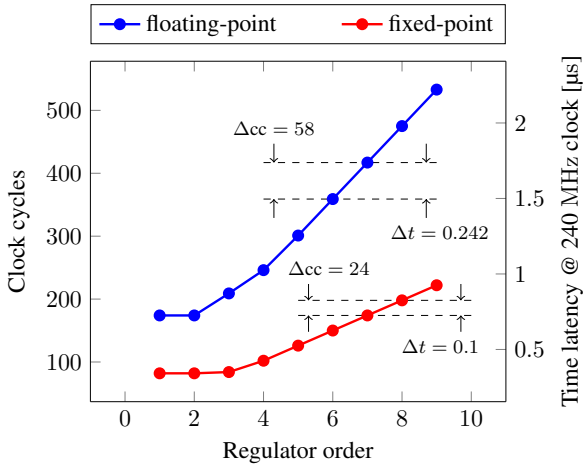

Figure 49: Latency of the regulator busy states under various orders and data types.

Table 9: Use of DSP resources by the two main computation units of the state-space algorithm.

Unit	Implementation	DSPs	Clock cycles	Total DSPs for 7th order
MAC	fixed-point	1	5	26
	floating-point	4	22	104
Sum	fixed-point	none	3	none
	floating-point	2	14	18

Finally, it can be argued that applying the proposed data flow architecture to scalar operations, such as $\gamma \cdot \delta\tau$, is far beyond what is required. Hence, the unwanted overhead. This is a reasonable point provided the system does not change in the future. Yet there are plans to extend the system in order to regulate the compression and energy of the electron bunches. In this case, the current architecture can be easily scaled to implement the required mathematical operation, e.g.

$$\begin{bmatrix} y_\tau \\ y_E \\ y_C \end{bmatrix} = \begin{bmatrix} \gamma_\tau & 0 & 0 \\ 0 & \gamma_E & 0 \\ 0 & 0 & \gamma_C \end{bmatrix} \cdot \begin{bmatrix} \delta\tau \\ \delta E \\ \delta C \end{bmatrix}, \tag{52}$$

where E and C denote the energy and compression of the electron bunches, respectively. This underscores the scalability of the current digital solution. Meanwhile, the correctness of this solution can be verified using a special digital testbench.

4.5 Firmware Verification

The correctness of the regulator implementation is verified by assembling a digital setup, which involves an FPGA with the beam-based regulator connected to an additional FPGA that serves as a testbench. Along with the verification of the state-space implementation, the usage of the separate FPGA allows testing low-latency link communication. The installation can be observed in Figure 50. The two FPGAs are inserted into a MTCA.4 crate leaving only their front panels exposed. As can be seen, these panels feature SFP slots that are used to interconnect the two devices using optical cables.

Figure 50: MTCA.4 crate with two installed FPGAs serving as a testbench.

In principle, the testbench operation can be outlined as follows

1. Sending a stimulus to an FPGA that features the implementation of a beam-based regulator
2. Receiving a response
3. Comparing the received response with the one generated by a floating-point MATLAB simulation

The floating-point MATLAB simulation is run offline and its responses are saved. Then, during the testbench operation, the MATLAB responses are loaded into the testbench for comparison. Since the FPGA and MATLAB are driven by the same stimulus, i.e. measured BAM data, both responses are expected to be identical to a certain degree of precision. Figure 51 summarizes the outlined testbench operation. Then, the testbench operation produces a result that is depicted in Figure 52. The result indicates correspondence between the FPGA and MATLAB responses. The result can also be viewed as a difference between the FPGA and MATLAB data, see Figure 53. It is important to note that, compared to the proportional regulator, the response mismatch of the $\mathcal{H}_2$ regulator grows. Essentially, the assembled testbench represents an open-loop system, i.e. the output of the testbench regulator has no effect on the next BAM data sample. Since the $\mathcal{H}_2$ regulator has state, the open-loop scenario leads to accumulation of the mismatch between the two responses. Nevertheless, Chapter 3 demonstrated that the issue poses no problem when the regulator closes the feedback loop on the real machine.

4.6 Conclusions

In this chapter, the implementation of a high-order state-space regulator for a fast beam-based feedback was presented. The real-time execution was achieved by implementing the digital regulator on a powerful Kintex-7 FPGA chip from Xilinx. In this context, the ability of FPGA-based solutions to execute operations in a massively parallel manner enabled an efficient implementation of the regulator in its state-space form. Specifically, digital

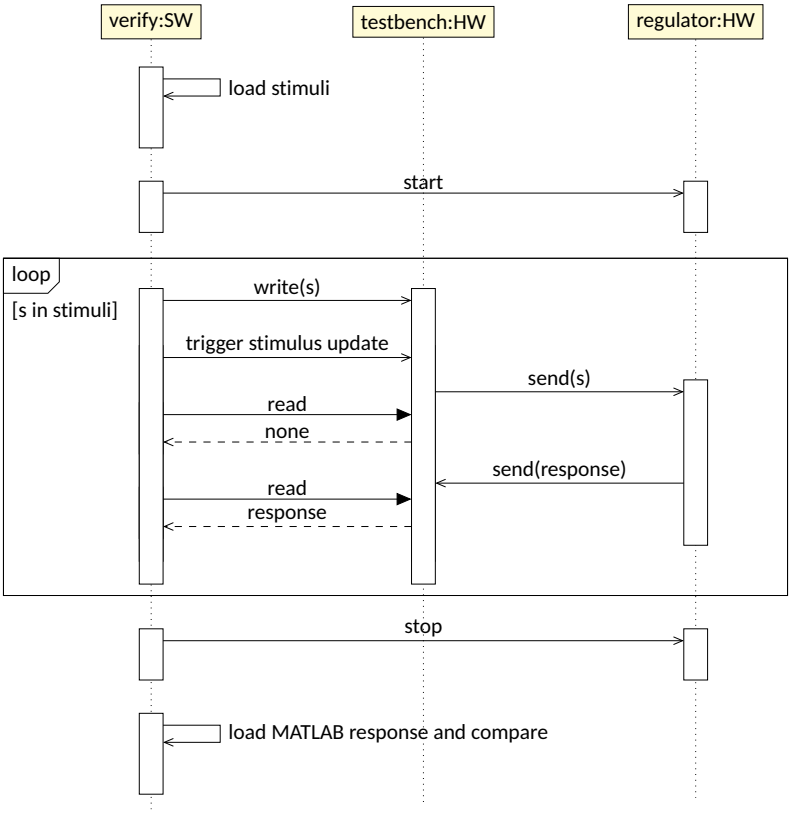

Figure 51: UML sequence diagram showing the operation of a testbench for a beam-based regulator.

circuits, called systolic arrays, were used to parallelize the corresponding matrix-vector multiplications. Furthermore, specific solutions were required to support the continuous-wave operation of the machine. Since there are no time pauses in this type of operation, there had to be a mechanism that allows safe updates of the regulator gains at any time instant. This resulted in the application of finite-state machines. Finally, the implementation was verified with the help of a specially designed hardware/software testbench, and the result of this testbench indicated the correctness of the implementation. This was an essential step before validating the regulator on the real machine, as described in Chapter 3.

In addition to presenting the overall digital architecture, this work demonstrated that the usage of data types with fixed-point precision is a viable solution for this kind of regulation problems. Compared to its floating-point counterpart, the fixed-point implementation not only results in faster digital circuits, but also encourages a more thorough system analysis.

Finally, even though the systolic arrays added data management overhead into the design, it was shown that the design can easily be scaled in terms of the regulator orders, inputs and outputs. Thus, future work is supported by the scalability of the presented architecture.

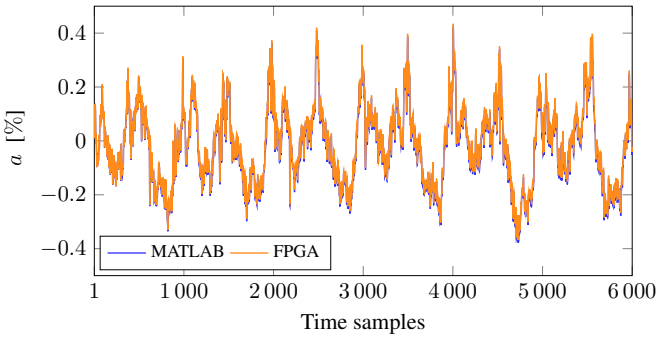

(a)

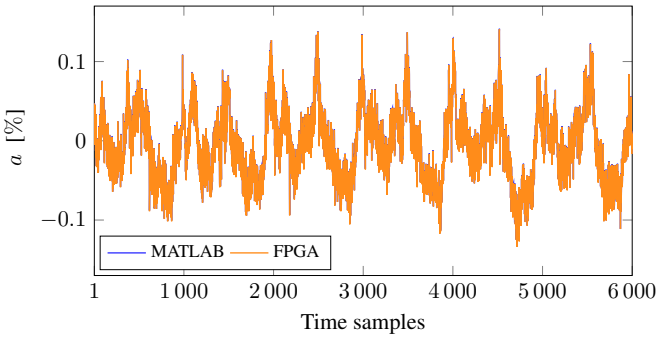

(b)

*Figure 52: Comparison of MATLAB and FPGA responses for **(a)** the $\mathcal{H}_2$ and **(b)** proportional regulators.*

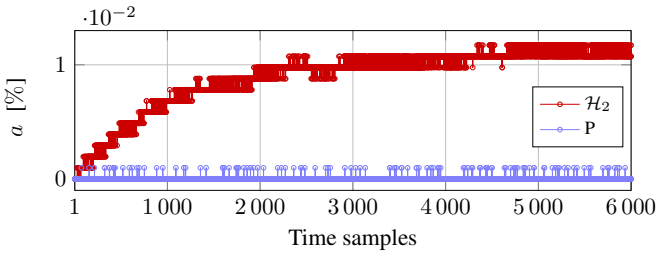

(a)

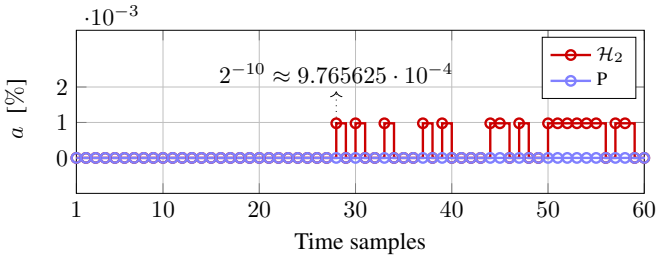

(b)

Figure 53: *Comparison of FPGA and MATLAB responses for the $\mathcal{H}_2$ and proportional regulators.* ***(a)*** *The difference between the data shows that the state of the $\mathcal{H}_2$ regulator accumulates a data mismatch over time.* ***(b)*** *When zoomed, the data reveals that the $\mathcal{H}_2$ implementation is able to produce about 30 matching responses, before the least significant fraction bit flips. The magnitude of the bit flip corresponds to the precision of the fixed-point data type (1, 18, 10) used by the LLRF controller.*

Conclusions

This work was carried out at the intersection of three disciplines, namely accelerator physics, control theory and digital logic. In general, such intersections allow treating a research problem from various perspectives, and this may lead to unexpected findings. For example, this work revealed that some of these disciplines, i.e. the accelerator physics and control theory, treat terms, which are critical for this work, in a fundamentally different manner. The term nonlinear dynamics, which is used in the accelerator domain to describe the behavior of a bunch compressor, has nothing to do with a dynamical system from the control point of view. Chapter 2 showed that the bunch compressor is a static system. A simulation model, which was created in Simulink, demonstrated that any dynamics observed downstream of the bunch compressor were defined by noise acting on this static system. Hence the importance to consider this noise and model it appropriately.

The noise modeling that was presented in Chapters 2 and 3 helped to answer a research question regarding the appropriateness of using an RF noise to model disturbance for the given regulation task. It was shown that this noise constitutes only a minor contribution to the actual electron bunch arrival time noise observed downstream of the bunch compressor. Thus, the RF noise reflects the actual one neither in size, nor in frequency-domain shape. Moreover, the model of the RF noise turned out to be rather high-order, which was undesired with respect to subsequent implementation. For all of these reasons, it was decided to use the actual noise for the disturbance modeling.

The modeling insight, that the rms value of the given noise can be expressed as the $\mathcal{H}_2$ norm of the corresponding dynamical system, was another finding in this interdisciplinary work. Following this, a physical problem to minimize the rms noise in the accelerator domain could be translated into a specific regulation method in the control domain. Chapter 3 described the design of a beam-based regulator in the context of the $\mathcal{H}_2$ mixed-sensitivity problem. This formulation allowed to incorporate the established dynamical disturbance model into the regulator design and set the rms minimization as the design goal. In turn, such disturbance model-based design immediately resolved the bandwidth issue of a slow SRF cavity that was used as the actuator. Furthermore, the proper bandwidth definition helped to avoid the fundamental limitation of proportional beam-based regulators, i.e. coupling with the LLRF control loop that can result in unwanted plant oscillations. The evaluation on the continuous-wave linear accelerator ELBE demonstrated the efficiency of the proposed beam-based regulator. Compared to its proportional counterpart, the disturbance model-based regulator could achieve the decoupling and suppress the electron bunch arrival time noise by a factor of three. This degree of suppression could only be achieved by the proportional regulator, while triggering the unwanted plant oscillations. In addition, the proposed design showed excellent agreement between the model and measured data. The presented modeling could thus be used to predict the amounts of residual noise and required regulation effort. In case of the proportional regulator, such predictions were problematic due to the above-mentioned limitation. This outstanding result not only fulfilled one of the research goals, but ultimately led to the main thesis of this work, i.e.

> A single regulation stage, which is installed in a continuous-wave linear accelerator and features a disturbance model-based beam-based regulator, has a potential to outperform a commonly used proportional regulator, without compromising the plant stability.

Of course, this result could not be possible without the digital logic. This discipline introduced an additional degree of freedom into this work and, thus, allowed to implement the designed high-order state-space regulator as a real-time feasible solution. In this context, Chapter 4 showed a digital logic design that was written in VHDL and deployed on a powerful Kintex-7 FPGA chip from Xilinx. Despite being commonly regarded as an implementation detail, this part of the work answered a few important research questions as well. In particular, the advantages and drawbacks of using fixed-point data types were presented and compared to their floating-point counterparts. The conclusion was that the given task could benefit from the usage of fixed-point arithmetic, because faster and smaller circuits outweighed an increased labor to analyze and configure the fixed-point data types. In addition, it was shown that the designed digital architecture could be easily reconfigured in terms of the regulator orders, inputs and outputs. In other words, the flexibility of the state-space form in the control domain was reflected as a scalability in the digital domain. This means that the developed solution not only served as a demonstrator in this work, but is also ready to be extended for future research.

Future Research

This work extended the knowledge regarding the stability of continuous-wave linear accelerators. This opens a possibility for the growing CW community, including the upcoming Dresden Advanced Light Infrastructure (DALI) [26], to take these results and build new research on top of them. In the mean time, a number of relevant problems for such research is outlined below. Solving these problems not only broadens the feedback strategy of the current beam-based regulator, but also ensures its routine operation.

Regulation of high-frequency noise Increasing the bandwidth of the designed beam-based regulator may seem as a natural way to suppress the noise even more. However, doing so will degrade the performance, as the regulator will start amplifying the high-frequency noise instead of suppressing it. The reason is that the bandwidth specification of 3.5 kHz is leveraged in this work in two ways: 1) to neglect the actuator dynamics and 2) to neglect the disturbance dynamics in the high-frequency range. Both simplify the design at the cost of introducing unmodeled dynamics. Such dynamics have no gain and phase margin information, so increasing the bandwidth will force the regulator into a frequency region, where an insufficient phase margin turns a negative feedback into a positive one. Hence the amplification of the high-frequency noise. For this reason, the current design must strictly adhere to the specified bandwidth. And the evaluation on the real machine showed that this is a viable approach that can achieve good results. Still, the remaining 19 fs of rms noise raise a question of addressing the frequency range, where the designed regulator is not active. As the first potential solution, the current feedback strategy could be complemented by feed-forward techniques that involve simple notch filtering or a more sophisticated active noise control [62, 39]. Another solution could be to employ a normal conducting cavity that features a significantly wider bandwidth, which allows targeting the high-frequency noise [52, 54]. Compared to the first approach, the second one is more challenging, because it requires the installation of an additional cavity into the beamline.

Regulation of electron bunch compression The developed beam-based regulator modulates the energy of an electron bunch in order to change its arrival time. But such energy modulation can also impact the compression of the bunch. For this reason, the

beam-based regulator should be extended to support the regulation of the bunch compression. In turn, such extension necessitates answering the following research questions: what kind of sensors are available to sense the compression; can these sensors handle the current bunch repetition rate; what kind of data interface these sensors have; how is compression noise allocated in frequency domain; can this noise be modeled using a second-order dynamical system; what actuation is required to efficiently regulate the compression; how to tune the regulator to avoid performance degradation, when both amplitude and phase of an RF field are used for actuation.

Elimination of slow drifts The electron bunch arrival time, which is measured downstream of the magnetic chicane, depends on many parameters in the upstream beamline, and these parameters tend to drift over time. At the same time, the operating range of a beam-based regulator is limited to avoid considerable changes of RF variables, because these can trigger the machine protection system. It is thus of highest priority to eliminate these drifts in order to ensure routine operation of the beam-based regulator. The solution could require additional control strategies.

Investigation of high-frequency noise coming from SRF gun The SRF gun is one of the sources contributing to the initial arrival time noise. If this noise source makes a significant contribution to the high-frequency range, then the designed beam-based regulator, which focuses on the low-frequency range, will not be able to compensate the fast fluctuations. Investigating the causes of the high-frequency noise can, thus, improve the predictability of the final noise and ensure reliable beam-based regulation.

References

[1] A. Angelovski, A. Kuhl, M. Hansli, A. Penirschke, S. M. Schnepp, M. Bousonville, H. Schlarb, M. K. Bock, T. Weiland, and R. Jakoby. High bandwidth pickup design for bunch arrival-time monitors for free-electron laser. *Phys. Rev. ST Accel. Beams*, 15:112803, 2012.

[2] A. Arnold, H. Büttig, D. Janssen, T. Kamps, G. Klemz, W. Lehmann, U. Lehnert, D. Lipka, F. Marhauser, P. Michel, K. Möller, P. Murcek, C. Schneider, R. Schurig, F. Staufenbiel, J. Stephan, J. Teichert, V. Volkov, I. Will, and R. Xiang. A high-brightness SRF photoelectron injector for FEL light sources. *Nucl. Instrum. Methods Phys. Res. A, Accel. Spectrom. Detect. Assoc. Equip.*, 593(1):57–62, 2008.

[3] P. Ashenden. *The Designer's Guide to VHDL*. Morgan Kaufmann Publishers, San Francisco, CA, USA, third edition, 2008.

[4] G. Balas, A. Packard, M. Safonov, and R. Chiang. Next generation of tools for robust control. In *Proc. 2004 Am. Control Conf.*, pages 5612–5615, 2004.

[5] A. Bellandi, Ł. Butkowski, B. Dursun, A. Eichler, Ç. Gümüş, M. Kuntzsch, A. Nawaz, S. Pfeiffer, H. Schlarb, C. Schmidt, K. Zenker, and J. Branlard. Online Detuning Computation and Quench Detection for Superconducting Resonators. *IEEE Trans. Nucl. Sci.*, 68(4):385–393, 2021.

[6] S. Boyd and C. Barratt. *Linear Controller Design: Limits of Performance*. Prentice-Hall Inc., Hoboken, New Jersey, USA, 1991.

[7] R. Brinkmann, E. Schneidmiller, J. Sekutowicz, and M. Yurkov. Prospects for CW and LP operation of the European XFEL in hard X-ray regime. *Nucl. Instrum. Methods Phys. Res. A, Accel. Spectrom. Detect. Assoc. Equip.*, 768:20–25, 2014.

[8] J. Burke, D. Henrion, A. Lewis, and M. Overton. HIFOO - A MATLAB package for fixed-order controller design and $\mathcal{H}_\infty$ optimization. In *Proc. 5th IFAC Symp. Robust Control Des.*, pages 339–344, 2006.

[9] Ł. Butkowski, T. Kozak, P. Predki, R. Rybaniec, and B. Yang. FPGA Firmware Framework for MTCA.4 AMC Modules. In *Proc. 15th Int. Conf. Accelerator and Large Exp. Phys. Control Syst.*, pages 876–880, 2015.

[10] R. Calaga, A. Alekou, F. Antoniou, R. B. Appleby, L. Arnaudon, K. Artoos, G. Arduini, V. Baglin, S. Barriere, H. Bartosik, P. Baudrenghien, I. Ben-Zvi, T. Bohl, A. Boucherie, O. S. Brüning, K. Brodzinski, A. Butterworth, G. Burt, O. Capatina, S. Calvo, T. Capelli, M. Carlà, F. Carra, L. R. Carver, A. Castilla-Loeza, E. Daly, L. Dassa, J. Delayen, S. U. De Silva, A. Dexter, M. Garlasche, F. Gerigk, L. Giordanino, D. Glenat, M. Guinchard, A. Harrison, E. Jensen, C. Julie, T. Jones, F. Killing, A. Krawczyk, T. Levens, R. Leuxe, B. Lindstrom, Z. Li, A. MacEwen, A. Macpherson, P. Menendez, T. Mikkola, P. Minginette, J. Mitchell, E. Montesinos, G. Papotti, H. Park, C. Pasquino, S. Pattalwar, E. C. Pleite, T. Powers, B. Prochal, A. Ratti, L. Rossi, V. Rude, M. Therasse, R. Tomás, N. Stapley, I. Santillana, N. Shipman, J. Simonin, M. Sosin, J. Swieszek, N. Templeton, G. Vandoni, S. Verdú-Andrés, M. Wartak, C. Welsch, D. Wollman, Q. Wu, B. Xiao, E. Yamakawa, C. Zanoni, F. Zimmermann, and A. Zwozniak. First demonstration of the use of crab cavities on hadron beams. *Phys. Rev. Accel. Beams*, 24:062001, Jun 2021.

[11] M. Chen, J.-C. Deinert, B. Green, Z. Wang, I. Ilyakov, N. Awari, M. Bawatna, S. Germanskiy, T. V. A. G. de Oliveira, G. Geloni, T. Tanikawa, M. Gensch, and S. Kovalev. Pulse- and field-resolved THz-diagnostics at 4th generation lightsources. *Opt. Express*, 27(22), 2019.

[12] A. Clements. *Principles of Computer Hardware*. Oxford University Press Inc., New York, NY, USA, fourth edition, 2006.

[13] A. Demir and A. L. Sangiovanni-Vincentelli. Simulation and Modeling of Phase Noise in Open-Loop Oscillators. In *Proc. Custom Integr. Circuits Conf.*, pages 453–456, 1996.

[14] G. Dimitrakopoulos, A. Psarras, and I. Seitanidis. *Microarchitecture of Network-on-Chip Routers: A Designer's Perspective*. Springer Science + Business Media, New York, NY, USA, 2015.

[15] Dimtel, Inc. LLRF9. Available online: `https://www.dimtel.com/products/llrf9`, 2015. Accessed: 2023-01-30.

[16] dSPACE GmbH. SCALEXIO. Available online: `https://www.dspace.com/en/pub/home/products/hw/simulator_hardware/scalexio.cfm`, 2022. Accessed: 2023-01-30.

[17] P. Emma. X-Band RF Harmonic Compensation for Linear Bunch Compression in the LCLS. Technical note, Report No. LCLS-TN-01-1, Stanford Linear Accelerator Center, Stanford University, Stanford, California, USA, 2001.

[18] P. Emma. *Handbook of Accelerator Physics and Engineering*, chapter Bunch Compression, pages 334–337. World Scientific Publishing Co. Pte. Ltd., Hackensack, New Jersey, USA, second edition, 2013.

[19] G. Feldhaus and A. Roth. A 1 MHz to 50 GHz Direct Down-Conversion Phase Noise Analyzer With Cross-Correlation. In *Proc. 2016 Eur. Frequency and Time Forum*, pages 1–4, 2016.

[20] J. Galayda. The Linac Coherent Light Source-II Project. In *Proc. 5th Int. Particle Accelerator Conf.*, pages 935–937, 2014.

[21] P. Gessler, M. Bock, M. Felber, K. Hacker, F. Ludwig, H. Schlarb, B. Schmidt, S. Schulz, and J. Szewinski. Real-Time Sampling and Processing Hardware for Bunch Arrival-Time Monitors at FLASH and XFEL. In *Proc. 32nd Int. Free Electron Laser Conf.*, pages 585–587, 2010.

[22] B. Green, S. Kovalev, V. Asgekar, G. Geloni, U. Lehnert, T. Golz, M. Kuntzsch, C. Bauer, J. Hauser, J. Voigtlaender, B. Wustmann, I. Koesterke, M. Schwarz, M. Freitag, A. Arnold, J. Teichert, M. Justus, W. Seidel, C. Ilgner, N. Awari, D. Nicoletti, S. Kaiser, Y. Laplace, S. Rajasekaran, L. Zhang, S. Winnerl, H. Schneider, G. Schay, I. Lorincz, A. A. Rauscher, I. Radu, S. Mährlein, T. H. Kim, J. S. Lee, T. Kampfrath, S. Wall, J. Heberle, A. Malnasi-Csizmadia, A. Steiger, A. S. Müller, M. Helm, U. Schramm, T. Cowan, P. Michel, A. Cavalleri, A. S. Fisher, N. Stojanovic, and M. Gensch. High-Field High-Repetition-Rate Sources for the Coherent THz Control of Matter. *Sci. Rep.*, 6(1):22256, 2016.

[23] H. A. Hafez, S. Kovalev, J.-C. Deinert, Z. Mics, B. Green, N. Awari, M. Chen, S. Germanskiy, U. Lehnert, J. Teichert, Z. Wang, K.-J. Tielrooij, Z. Liu, Z. Chen, A. Narita, K. Müllen, M. Bonn, M. Gensch, and D. Turchinovich. Extremely efficient terahertz high-harmonic generation in graphene by hot Dirac fermions. *Nature*, 561(7724):507–511, 2018.

[24] H. A. Hafez, S. Kovalev, K.-J. Tielrooij, M. Bonn, M. Gensch, and D. Turchinovich. Terahertz Nonlinear Optics of Graphene: From Saturable Absorption to High-Harmonics Generation. *Adv. Optical Mater.*, 8(3):1900771, 2020.

[25] G. Heinzel, A. Rüdiger, and R. Schilling. Spectrum and spectral density estimation by the Discrete Fourier transform (DFT), including a comprehensive list of window functions and some new flat-top windows. Report, Max-Planck-Institut für Gravitationsphysik, 2002.

[26] M. Helm, S. Winnerl, A. Pashkin, J. M. Klopf, J.-C. Deinert, S. Kovalev, P. Evtushenko, U. Lehnert, R. Xiang, A. Arnold, A. Wagner, S. M. Schmidt, U. Schramm, T. Cowan, and P. Michel. The ELBE infrared and THz facility at Helmholtz-Zentrum Dresden-Rossendorf. *Eur. Phys. J. Plus*, 138(2):158, 2023.

[27] M. Heuer, G. Lichtenberg, S. Pfeiffer, H. Schlarb, C. Schmidt, and H. Werner. Modeling of the Master Laser Oscillator Phase Noise for the European XFEL using Fractional Order Systems. In *Proc. 19th IFAC World Congr.*, pages 9235–9240, 2014.

[28] IEEE Standard 1076-2019. IEEE Standard for VHDL Language Reference Manual. Standard, 2019.

[29] IEEE Standard 1139-2008. IEEE Standard Definitions of Physical Quantities for Fundamental Frequency and Time Metrology—Random Instabilities. Standard, 2009.

[30] IEEE Standard 754-2019. IEEE Standard for Floating-Point Arithmetic. Standard, 2019.

[31] J.-W. Jang, S. Choi, and V. Prasanna. Energy- and time-efficient matrix multiplication on FPGAs. *IEEE Trans. Very Large Scale Integr. VLSI Syst.*, 13(11):1305–1319, 2005.

[32] M. Killenberg, S. Marsching, L. Petrosyan, A. Piotrowski, and C. Schmidt. Drivers and Software for MTCA.4. In *Proc. 5th Int. Particle Accelerator Conf.*, pages 3137–3139, 2014.

[33] W. Koprek, C. Behrens, M. K. Bock, M. Felber, P. Gessler, K. Hacker, H. Schlarb, C. Schmidt, B. Steffen, S. Wesch, S. Schulz, and J. Szewinski. Intra-train Longitudinal Feedback for Beam Stabilization at FLASH. In *Proc. 32nd Int. Free Electron Laser Conf.*, pages 537–543, 2010.

[34] S. Kovalev, B. Green, T. Golz, S. Maehrlein, N. Stojanovic, A. S. Fisher, T. Kampfrath, and M. Gensch. Probing ultra-fast processes with high dynamic range at 4th-generation light sources: Arrival time and intensity binning at unprecedented repetition rates. *Struct. Dyn.*, 4(2):024301, 2017.

[35] S. Kovalev, Z. Wang, J.-C. Deinert, N. Awari, M. Chen, B. Green, S. Germanskiy, T. V. A. G. de Oliveira, J. S. Lee, A. Deac, D. Turchinovich, N. Stojanovic, S. Eisebitt, I. Radu, S. Bonetti, T. Kampfrath, and M. Gensch. Selective THz control of magnetic order: new opportunities from superradiant undulator sources. *J. Phys. D: Appl. Phys.*, 51(11):114007, 2018.

[36] M. Kuntzsch, M. Gensch, U. Lehnert, P. Michel, R. Schurig, and J. Teichert. Jitter Analysis at CW Repetition Rate With Large Spectral Range and High Resolution. In *Proc. 4th Int. Beam Instrum. Conf.*, pages 43–45, 2015.

[37] M. Kuntzsch, R. Steinbrück, R. Schurig, M. Hierholzer, M. Killenberg, C. Schmidt, M. Hoffmann, C. Iatrou, J. Rahm, I. Rutkowski, and M. Grzegrzółka. MicroTCA.4-Based LLRF for CW Operation at ELBE - Status and Outlook. In *Proc. 6th Int. Beam Instrum. Conf.*, pages 101–103, 2017.

[38] M. Kuntzsch, K. Zenker, A. Maalberg, A. Schwarz, M. Czwalinna, and J. Kral. Update of the Bunch Arrival Time Monitor at ELBE. In *Proc. 13th Int. Particle Accelerator Conf.*, pages 260–262, 2022.

[39] S. Kuo and D. Morgan. Active noise control: a tutorial review. *Proc. IEEE*, 87(6):943–973, 1999.

[40] H. Kwakernaak. $\mathcal{H}_2$-Optimization—Theory and Applications to Robust Control Design. In *Proc. 3rd IFAC Symp. Robust Control Des.*, pages 437–448, 2000.

[41] U. Lehnert, P. Michel, R. Schurig, A. Aksoy, P. Evtushenko, and J. Krämer. Bunch Compression of the Low-energy ELBE Electron Beam for Super-radiant THz Sources. In *Proc. 5th Int. Particle Accelerator Conf.*, pages 1123–1125, 2014.

[42] A. Maalberg, M. Kuntzsch, and E. Petlenkov. Simulation of RF Noise Propagation to Relativistic Electron Beam Properties in a Linear Accelerator. In *Proc. 21st IFAC World Congr.*, pages 348–354, Jul 2020.

[43] A. Maalberg, M. Kuntzsch, and E. Petlenkov. Real-Time Regulation of Beam-Based Feedback: Implementing an FPGA Solution for a Continuous Wave Linear Accelerator. *Sensors*, 22(16):6236, Aug 2022.

[44] A. Maalberg, M. Kuntzsch, and E. Petlenkov. Regulation of the Linear Accelerator ELBE Exploiting Continuous Wave Mode of a Superconducting RF Cavity. In *Proc. 2022 Am. Control Conf.*, pages 5346–5353, Jun 2022.

[45] A. Maalberg, M. Kuntzsch, K. Zenker, and E. Petlenkov. Regulation of electron bunch arrival time for a continuous-wave linac: Exploring the application of the $\mathcal{H}_2$ mixed-sensitivity problem. *Phys. Rev. Accel. Beams*, 26:072801, Jul 2023.

[46] MathWorks. linmod: Extract continuous-time linear state-space model around operating point. Available online: `https://se.mathworks.com/help/simulink/slref/linmod.html`, 2023. Accessed: 2023-03-31.

[47] P. Michel. The radiation source ELBE at the Forschungszentrum Dresden-Rossendorf. In *2008 IEEE Nucl. Sci. Symp. Conf. Rec.*, pages 3078–3080, 2008.

[48] N.A.T. Data Processing AMC Module for MTCA & ATCA. Available online: `https://nateurope.com/product/namc-tck7/`, 2018. Accessed: 2023-01-05.

[49] A. Neumann, W. Anders, O. Kugeler, and J. Knobloch. Analysis and active compensation of microphonics in continuous wave narrow-bandwidth superconducting cavities. *Phys. Rev. ST Accel. Beams*, 13:082001, Aug 2010.

[50] N. Nise. *Nise's Control Systems Engineering*. John Wiley & Sons, Ltd, Chichester, West Sussex, England, global edition, 2015.

[51] S. Pfeiffer. *Symmetric Grey Box Identification and Distributed Beam-Based Controller Design for Free-Electron Lasers*. PhD thesis, Hamburg University of Technology, 2014.

[52] S. Pfeiffer, J. Branlard, Ł. Butkowski, M. Hierholzer, M. Hoffmann, K. Honkavaara, H. Schlarb, C. Schmidt, S. Schreiber, M. Vogt, J. Zemella, and M. Fakhari. Status Update of the Fast Energy Corrector Cavity at FLASH. In *Proc. 29th Linear Accelerator Conf.*, pages 112–114, 2018.

[53] S. Pfeiffer, J. Branlard, M. Hoffmann, and C. Schmidt. Advanced LLRF System Setup Tool for RF Field Regulation of SRF Cavities. In *Proc. 19th Int. Conf. RF Superconductivity*, pages 1063–1067, 2019.

[54] S. Pfeiffer, Ł. Butkowski, M. Czwalinna, B. Dursun, C. Gerth, B. Lautenschlager, H. Schlarb, and C. Schmidt. Longitudinal Intra-train Beam-Based Feedback at FLASH. In *Proc. 39th Free Electron Laser Conf.*, pages 346–349, 2019.

[55] S. Pfeiffer, G. Lichtenberg, C. Schmidt, H. Schlarb, and H. Werner. Design of an Optimal and Robust Controller for a Free-Electron Laser Exploiting Symmetries of the RF-System. In *Proc. 51st IEEE Conf. Decision Control*, pages 4253–4258, 2012.

[56] S. Pfeiffer, C. Schmidt, M. K. Bock, H. Schlarb, W. Jałmużna, G. Lichtenberg, and H. Werner. Fast Feedback Strategies for Longitudinal Beam Stabilization. In *Proc. 2012 Int. Particle Accelerator Conf.*, 2012.

[57] S. Pfeiffer, C. Schmidt, G. Lichtenberg, and H. Werner. Grey Box Identification for the Free Electron Laser FLASH exploiting Symmetries of the RF-System. In *Proc. 18th IFAC World Congr.*, pages 10770–10775, 2011.

[58] S. Pfeiffer, H. Werner, C. Schmidt, and H. Schlarb. Distributed Controller Design for a Free-Electron Laser. In *Proc. 2013 Am. Control Conf.*, pages 6553–6558, 2013.

[59] A. Popov, H. Werner, and M. Millstone. Fixed-structure discrete-time $\mathcal{H}_\infty$ controller synthesis with HIFOO. In *Proc. 49th IEEE Conf. Decision Control*, pages 3152–3155, 2010.

[60] F. Qiu, S. Michizono, T. Miura, T. Matsumoto, N. Liu, and S. B. Wibowo. Real-time cavity simulator-based low-level radio-frequency test bench and applications for accelerators. *Phys. Rev. Accel. Beams*, 21:032003, 2018.

[61] A. Rezaeizadeh, T. Schilcher, and R. S. Smith. Adaptive robust control of longitudinal and transverse electron beam profiles. *Phys. Rev. Accel. Beams*, 19:052802, 2016.

[62] R. Rybaniec, K. Przygoda, W. Cichalewski, V. Ayvazyan, J. Branlard, Ł. Butkowski, S. Pfeiffer, C. Schmidt, H. Schlarb, and J. Sekutowicz. FPGA-Based RF and Piezocontrollers for SRF Cavities in CW Mode. *IEEE Trans. Nucl. Sci.*, 64:1382–1388, 2017.

[63] T. Schilcher. *Vector Sum Control of Pulsed Accelerating Fields in Lorentz Force Detuned Superconducting Cavities*. PhD thesis, Hamburg University, 1998.

[64] H. Schlarb. Techniques for Pump-Probe Synchronisation of Fsec Radiation Pulses. In *Proc. 2005 Particle Accelerator Conf.*, pages 59–63, 2005.

[65] C. Schmidt. *RF System Modeling and Controller Design for the European XFEL*. PhD thesis, Hamburg University of Technology, 2010.

[66] C. Schmidt, M. Bock, W. Koprek, S. Pfeiffer, H. Schlarb, and W. Jałmużna. Feedback Strategies for Bunch Arrival Time Stabilization at FLASH Towards 10 fs. In *Proc. 33rd Int. Free Electron Laser Conf.*, pages 531–534, 2011.

[67] C. Schmidt, G. Lichtenberg, W. Koprek, W. Jałmużna, H. Werner, and S. Simrock. Parameter estimation and tuning of a multivariable RF controller with FPGA technique for the Free Electron Laser FLASH. In *Proc. 2008 Am. Control Conf.*, pages 2516–2521, 2008.

[68] S. Schulz, I. Grguraš, C. Behrens, H. Bromberger, J. T. Costello, M. K. Czwalinna, M. Felber, M. C. Hoffmann, M. Ilchen, H. Y. Liu, T. Mazza, M. Meier, S. Pfeiffer, P. Predki, S. Schefer, C. Schmidt, U. Wegner, H. Schlarb, and A. L. Cavalieri. Femtosecond all-optical synchronization of an X-ray free-electron laser. *Nature Communications*, 6(1):5938, 2015.

[69] S. Skogestad and I. Postlethwaite. *Multivariable Feedback Control: Analysis and Design*. John Wiley & Sons, Ltd, Chichester, West Sussex, England, second edition, 2005.

[70] J. St. John, C. Herwig, D. Kafkes, J. Mitrevski, W. Pellico, G. Perdue, A. Quintero-Parra, B. Schupbach, K. Seiya, N. Tran, M. Schram, J. M. Duarte, Y. Huang, and R. Keller. Real-time artificial intelligence for accelerator control: A study at the Fermilab Booster. *Phys. Rev. Accel. Beams*, 24:104601, 2018.

[71] Struck Innovative Systeme. SIS8300-L2 MTCA.4 Digitizer. Available online: `https://www.struck.de/sis8300-l2.html`, 2023. Accessed: 2023-02-19.

[72] H. Vennekate, A. Arnold, P. Lu, P. Murcek, J. Teichert, and R. Xiang. Emittance compensation schemes for a superconducting rf injector. *Phys. Rev. Accel. Beams*, 21:093403, Sep 2018.

[73] E. Vogel. High gain proportional rf control stability at TESLA cavities. *Phys. Rev. ST Accel. Beams*, 10:052001, 2007.

[74] T. Walter, F. Ludwig, K. Rehlich, and H. Schlarb. Novel Crate Standard MTCA.4 for Industry and Research. In *Proc. 4th Int. Particle Accelerator Conf.*, pages 3633–3635, 2013.

[75] S. B. Wibowo, T. Matsumoto, S. Michizono, T. Miura, F. Qiu, and N. Liu. Digital low level rf control system for the International Linear Collider. *Phys. Rev. Accel. Beams*, 21:082004, 2018.

[76] A. Wolski. *Beam Dynamics in High Energy Particle Accelerators*. Imperial College Press, London, England, 2014.

[77] Xilinx. 7 Series DSP48E1 Slice: User Guide. Available online: `https://docs.xilinx.com/v/u/en-US/ug479_7Series_DSP48E1`, 2018. Accessed: 2023-01-06.

[78] Xilinx. 7 Series FPGAs Data Sheet: Overview. Available online: `https://docs.xilinx.com/v/u/en-US/ds180_7Series_Overview`, 2020. Accessed: 2023-01-06.

[79] Xilinx. Floating-Point Operator v7.1: LogiCORE IP Product Guide. Available online: `https://docs.xilinx.com/v/u/en-US/pg060-floating-point`, 2020. Accessed: 2023-02-02.

[80] K. Zenker, Ç. Gümüş, M. Hierholzer, P. Michel, S. Pfeiffer, H. Schlarb, C. Schmidt, R. Schurig, R. Steinbrück, and M. Kuntzsch. MicroTCA.4-Based Low-Level RF for Continuous Wave Mode Operation at the ELBE Accelerator. *IEEE Trans. Nucl. Sci.*, 68(9):2326–2333, 2021.

[81] Z. Zhao, D. Wang, Z. Yang, and L. Yin. SCLF: An 8-GeV CW SCRF Linac-Based X-Ray FEL Facility in Shanghai. In *Proc. 38th Int. Free Electron Laser Conf.*, pages 182–184, 2018.

[82] F. Zhou, C. Adolphsen, A. Benwell, G. Brown, D. H. Dowell, M. Dunning, S. Gilevich, K. Grouev, G. Huang, B. Jacobson, X. H. Liu, A. Miahnahri, F. Sannibale, J. Schmerge, and T. Vecchione. Commissioning of the SLAC Linac Coherent Light Source II electron source. *Phys. Rev. Accel. Beams*, 24:073401, Jul 2021.

[83] R. Ziemer and W. Tranter. *Principles of Communications*. Wiley Publishing, 7 edition, 2014.

Acknowledgements

The author wishes to express his deep gratitude to his supervisors Dr. Michael Kuntzsch and Prof. Dr. Eduard Petlenkov for their support and guidance throughout the thesis work; colleagues Dr. Klaus Zenker and Dr. Ulf Lehnert for their help during the commissioning on the ELBE accelerator; control experts Dr. Sven Pfeiffer and Dr. Christian Schmidt from the Deutsches Elektronen-Synchrotron (DESY) for helpful advice; VHDL developers Cagil Gümüs, Burak Dursun and Łukasz Butkowski from DESY for their help with the MTCA.4 firmware framework.

The author would also like to thank his family for their strong support.

This work was partially funded by the Estonian Research Council grant PRG658.

Abstract

Improving Beam-Based Regulation for Continuous-Wave Linear Accelerators with a Disturbance Model-Based Design

The present thesis is devoted to improving the temporal resolution of time-resolved accelerator-based experiments. Due to the fact that this temporal resolution is largely determined by the accelerator stability, specifically by the stability of the underlying electron beam, this work concentrates on the analysis, design and implementation of regulation algorithms in order to enhance the temporal stability of the electron beam. In this context, Chapter 2 investigates the problem of exploiting radio frequency noise for the purpose of modeling an electron beam disturbance. The investigation shows that a disturbance model that is based on the radio frequency noise may become unnecessarily high-order, and even so, does not fully reflect the actual electron beam noise measured on the accelerator. Following this, Chapter 3 describes the design of a beam-based regulator that features a disturbance model that is derived from the measured electron beam noise data. The designed regulator is successfully evaluated on the continuous-wave linear accelerator ELBE. The presented results demonstrate that a single regulation stage, which is installed in a continuous-wave linear accelerator and features a disturbance model-based beam-based regulator, has a potential to outperform a commonly used proportional regulator, without compromising the plant stability. Finally, Chapter 4 presents a real-time feasible implementation of a high-order beam-based regulator that is ready to be employed for fast beam-based feedback.

Kokkuvõte

Pidevlaine lineaarsete kiirendite kiire põhise reguleerimise täiustamine häiringu mudelil põhineva sünteesi abil

Käesolev väitekiri on pühendatud ajas lahendatavate kiirendipõhiste katsete ajalise resolutsiooni parendamisele. Tulenevalt asjaolust, et selle ajalise lahendamise täpsuse määrab suuresti kiirendi stabiilsus, täpsemalt selle aluseks oleva elektronkiire stabiilsus, keskendub see töö reguleerimisalgoritmide analüüsile, disainile ja rakendamisele, et suurendada elektronkiire ajalist stabiilsust. Selles kontekstis uuritakse peatükis 2 raadiosagedusmüra ärakasutamist elektronkiire häirete modelleerimiseks. Uurimine näitab, et raadiosagedusliikul müral põhinev häiremudel võib muutuda tarbetult kõrge järguliseks ja isegi nii ei kajasta see täielikult kiirendil mõõdetud tegelikku elektronkiire müra. Pärast seda, kirjeldatakse peatükis 3 kiirel põhineva regulaatori sünteesi, mis sisaldab endas häiremudelit, mis on tuletatud mõõdetud elektronkiire müraandmetest. Projekteeritud regulaatorit hinnatakse edukalt pidevlaine lineaarkiirendil ELBE. Esitatud tulemused näitavad, et üks regulatsiooniaste, mis on paigaldatud pidevlaine lineaarsesse kiirendisse ja sisaldab häiremudelil põhinevat kiire põhist regulaatorit, omab potentsiaali ületada tavaliselt kasutatavat proportsionaalset regulaatorit, ilma kiirendi stabiilsust kahjustamata. Lõpuks, peatükis 4 tutvustatakse reaalajas teostatavat kõrge järgulist kiire põhist regulaatori rakendamist, mis on valmis kiire kiirel põhineva tagasiside jaoks.

Appendix 1 Sensitivity Functions S and T

Consider a single-input single-output feedback control system displayed in Figure 54 [69].

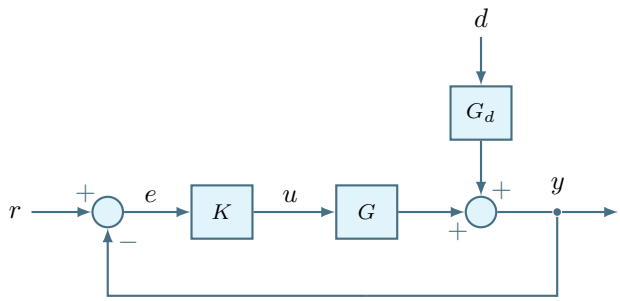

Figure 54: Block diagram of a feedback control system.

The output y is written as

$$y = GK(r - y) + G_d d, \tag{53}$$

where G and y denote the plant model and its output, G_d and d are the disturbance model and its input, and where K and r denote the controller model and the reference input, respectively. Then, (53) can be rewritten as

$$(1 + GK)y = GKr + G_d d, \tag{54}$$

and hence the closed-loop response becomes

$$y = \underbrace{(1 + GK)^{-1} GK}_{T} r + \underbrace{(1 + GK)^{-1}}_{S} d, \tag{55}$$

where S and T are the sensitivity and complimentary sensitivity functions, which characterize the sensitivity of y to disturbance d and reference r, respectively. The term complimentary sensitivity for T follows from the identity

$$S + T = 1. \tag{56}$$

So according to (55), reference tracking is obtained with $T \approx 1$ and disturbance rejection with $S \approx 0$, see Figure 55.

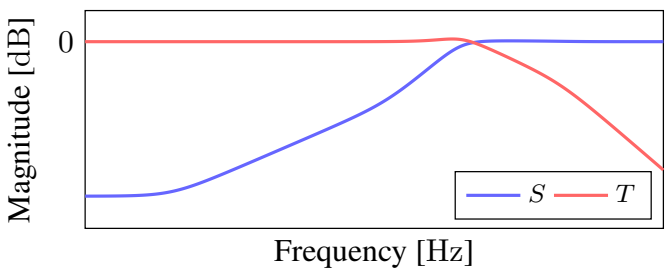

Figure 55: Example of a magnitude frequency response for sensitivity functions S and T.

Appendix 2 Algebraic Riccati Equation

The algebraic Riccati equation is considered here in the context of a linear quadratic regulator (LQR), because the latter is responsible for the full-state feedback in the observer-based structure of an $\mathcal{H}_2$ regulator.

The LQR problem is defined for a linear system $\dot{x} = Ax + Bu$ with a system matrix A, input matrix B and a non-zero initial state $x(0) \neq 0$ as finding a control signal $u(t)$ which takes the system to the zero state $x(\infty) = 0$ in an optimal manner. The problem is solved by minimizing a quadratic cost function

$$J = \int_0^\infty \left(x^T Q x + u^T R u\right) \mathrm{dt}, \tag{57}$$

where Q and R are constant weighting matrices that penalize the state error and control effort, respectively. The first step to solve this optimization problem is to manipulate the cost function by introducing a symmetric matrix $X = X^T$ as follows

$$J = x_0^T X x_0 - x_0^T X x_0 + \int_0^\infty \left(x^T Q x + u^T R u\right) \mathrm{dt},$$

where x_0 is the initial state of the system. Since the introduced terms cancel each other out, they do not change the cost function. Then, the negative term can be moved into the integral, where it transforms to a derivative

$$\frac{\mathrm{d}}{\mathrm{dt}}\left(x^T X x\right) = \dot{x}^T X x + x^T X \dot{x} = (Ax + Bu)^T X x + x^T X (Ax + Bu).$$

The transformation steps involve the product rule and substituting $\dot{x}$ with the linear system definition. Thus, the cost function becomes

$$J = x_0^T X x_0 + \int_0^\infty \left[(Ax + Bu)^T X x + x^T X (Ax + Bu) + x^T Q x + u^T R u\right] \mathrm{dt},$$

and then

$$J = x_0^T X x_0 + \int_0^\infty \left[x^T A^T X x + u^T B^T X x + x^T X A x + x^T X B u + x^T Q x + u^T R u\right] \mathrm{dt}.$$

Now, the terms $x^T(\cdot)x$ can be grouped together, which yields

$$J = x_0^T X x_0 + \int_0^\infty \left[x^T \left(A^T X + X A + Q\right) x + u^T R u + x^T X B u + u^T B^T X x\right] \mathrm{dt}. \tag{58}$$

Finally, by completing the square (58) can be rewritten as

$$J = x_0^T X x_0 + \int_0^\infty \left[x^T \left(A^T X + XA + Q - XBR^{-1}B^T X \right) x + \right.$$
$$\left. \left(u + R^{-1}B^T Xx \right) R \left(u + R^{-1}B^T Xx \right) \right] \mathrm{dt}. \tag{59}$$

Remember that the idea is to minimize the cost function J by finding the control signal u that optimally brings the state x to zero. According to (59), the only term that depends on u is the second term inside the integral. But this term can be brought to zero by setting

$$u + R^{-1}B^T Xx = 0 \Rightarrow u = -R^{-1}B^T Xx, \tag{60}$$

which denotes the full-state feedback $u = -Kx$, where $K = R^{-1}B^T X$. Now to find X the first term inside the integral must be set to zero, namely

$$A^T X + XA + Q - XBR^{-1}B^T X = 0, \tag{61}$$

and this represents the algebraic Riccati equation.

Appendix 3

I

A. Maalberg, M. Kuntzsch, and E. Petlenkov. Simulation of RF Noise Propagation to Relativistic Electron Beam Properties in a Linear Accelerator. In *Proc. 21st IFAC World Congr.*, pages 348–354, Jul 2020

Available online at www.sciencedirect.com

ScienceDirect

IFAC PapersOnLine 53-2 (2020) 348–354

Simulation of RF Noise Propagation to Relativistic Electron Beam Properties in a Linear Accelerator

Andrei Maalberg *,** **Michael Kuntzsch** * **Eduard Petlenkov** **

* *Helmholtz-Zentrum Dresden-Rossendorf, 01328 Dresden, Germany (e-mail: {a.maalberg, m.kuntzsch}@hzdr.de)*

** *Department of Computer Systems, Tallinn University of Technology, 19086 Tallinn, Estonia (e-mail: {andrei.maalberg, eduard.petlenkov}@taltech.ee)*

Abstract: The control system of the superconducting electron linear accelerator ELBE is planned to be upgraded by a beam-based feedback. As the design of the feedback algorithm enters its preliminary stage, the problem of analyzing the contribution of various disturbances to the development of the electron beam instabilities becomes highly relevant. In this paper we exploit the radio frequency (RF) phase and amplitude noise data measured at ELBE to create a behavioral model in Simulink. By modeling the interaction between a RF electromagnetic field and an electron bunch traversing a bunch compressor we analyze how the addition of RF noise impacts the electron beam properties, such as energy, duration and arrival time.

Copyright © 2020 The Authors. This is an open access article under the CC BY-NC-ND license (http://creativecommons.org/licenses/by-nc-nd/4.0)

Keywords: Electron Linear Accelerator; Bunch Compression; RF Noise; Simulink Model

1. INTRODUCTION

Particle accelerators are one of the most valuable tools to conduct large-scale research nowadays. The opportunities provided by such tools are used in a number of research centers around the world, including the one located in Dresden, Germany—Helmholtz-Zentrum Dresden-Rossendorf, or HZDR. An Electron Linear accelerator for beams with high Brilliance and low Emittance (ELBE) is operated at HZDR in continuous wave (CW) mode providing a versatile light source for scientific experiments. Represented by a beam of ultra-short photon pulses this light source is generated using accelerated electrons. By illustrating a fraction of the schematic layout of ELBE Figure 1 presents the path from the creation of electrons to their acceleration to the generation of photons.

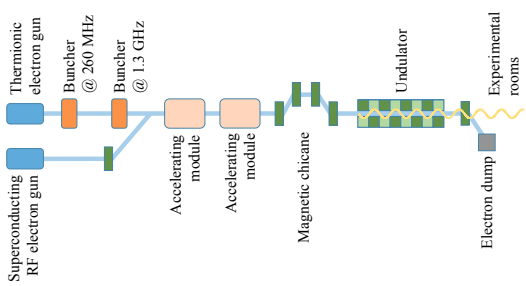

Fig. 1. Schematic layout of ELBE

In order to achieve acceptable quality of the generated photon pulses the properties of the electron beam, such as the energy, the arrival time and the electron bunch duration, must fulfill certain stability requirements. The process of stabilization is performed by controlling the amplitude and phase of the accelerating RF field, because these parameters actively participate in the beam acceleration process and thus affect the above-mentioned properties. Typically though this control scheme accounts neither for the electron beam measurements, nor other sources of instabilities, e.g. the noise contribution from the electron gun. Consequently, such control scheme has its limitations (Schmidt (2010)). A more robust way would be to control the beam properties by introducing a beam-based feedback. In this extended scheme the controller that controls its dedicated RF field—a local low-level radio frequency (LLRF) controller—takes the beam measurements into account. There exists a number of beam-based feedback designs in the field of linear accelerators (Rezaeizadeh et al. (2015); Pfeiffer (2014)), and each of them may greatly depend on the characteristics of its corresponding accelerator machine. As the existing control scheme at ELBE is planned to be upgraded by a beam-based feedback, the characteristics of this linear accelerator, including CW operation mode, superconductivity of RF cavities and high electron bunch repetition rate, need to be examined in order to have a proper understanding of the system in terms of control engineering.

The preliminary examination shows that the controlled variables, i.e. the amplitude and phase of the accelerating RF field, can be heavily constrained by the bandwidth of the corresponding RF cavity. For example, a superconducting cavity is essentially a band-pass filter with a very narrow bandwidth of a couple hundred hertz (Schilcher (1998)). Consequently, considering a bunch repetition rate in the order of 10 MHz the bunch-by-bunch control becomes practically infeasible. Furthermore, this work shows that the bandwidth of the actual disturbances that act

2405-8963 Copyright © 2020 The Authors. This is an open access article under the CC BY-NC-ND license.
Peer review under responsibility of International Federation of Automatic Control.
10.1016/j.ifacol.2020.12.184

on the electron beam is well below 1 MHz with one of the major contributors being the RF cavity itself. Of course, the ultimate disturbance coverage is not complete without considering 1) the beam arrival time instabilities coming from the electron gun and 2) the beam-RF interactions commonly referred to as the beam loading (Garoby (1992)). Nevertheless, 1) we show that the methods developed in this work can be extended to incorporate the beam arrival time instabilities and 2) we leave the beam loading effect for our subsequent works. Therefore, we believe that by analyzing the contribution of RF cavity noise to the development of electron beam instabilities we can make the first step to designing a beam-based feedback algorithm capable of compensating these instabilities more efficiently.

This paper is organized as follows: Section 2 explores the noise data measured at ELBE. Sections 3 and 4 deal with the analytic modeling of RF noise and linear accelerator respectively. In Section 5 a Simulink model is built allowing to simulate the interaction between a RF electromagnetic field and an electron bunch. Simulation results are presented in Section 6. Finally, Section 7 concludes the paper.

2. MEASUREMENT DATA

The data demonstrated in Figure 2 was measured using a Rohde & Schwarz Phase Noise Analyzer (Feldhaus and Roth (2016)) at one of the superconducting RF (SRF) cavities installed at ELBE. This data shows the closed loop noise behavior of the accelerating RF field, and since the latter is an important region of interaction between an electron beam and an accelerator, the presented data can be exploited as first principles in order to build a simulation model that will help analyze the behavior of the beam under various RF noise conditions. Additionally, the significance of this data comes from the fact that it represents the noise behavior of a cavity under the influence of a local digital LLRF controller. This is important from the point of view of the future beam-based feedback algorithm which will have to account for these local LLRF controllers and cooperate with them.

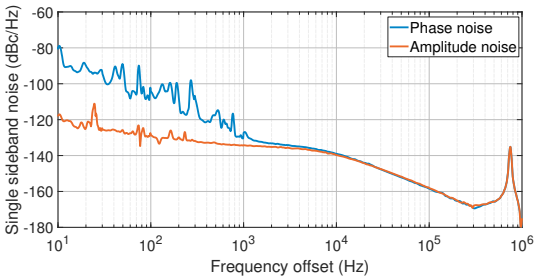

Fig. 2. Single sideband cavity noise measured at ELBE

2.1 Data Analysis

An ideal RF signal would be represented by a single spectral line. Typically, however, the spectral representation will contain a spread of spectral lines both below and above the carrier frequency. These additional spectral components, or sidebands, are caused by unwanted amplitude and phase fluctuations. According to the standard (IEEE Standard 1139-2008 (2009)), Figure 2 depicts the spectral components of both the phase and amplitude noise as

$$10\log\left(\frac{1}{2}S_\phi(f)\right), \qquad 10\log\left(\frac{1}{2}S_a(f)\right), \tag{1}$$

where $S_\phi(f)$ and $S_a(f)$ are one-sided spectral densities of the phase and amplitude fluctuations respectively.

Structurally, the phase and amplitude noise frequency data presented in Figure 2 contain two components: 1) a shape profile that decays with certain slopes as the frequency offset increases and 2) a number of spikes, or spurs, along this profile. In fact, the first one corresponds to the *random* noise component, while the second one is the result of *deterministic* noise sources.

The slopes of the random components present in the measured data can be defined by piecewise-linear approximation as shown in Table 1. Even though it is clear that in the low frequency range the power of the amplitude fluctuations is much lower than the one of the phase, in the higher frequency range the shape profiles start to coincide. This is one of the reasons not to neglect amplitude noise in the current analysis.

Table 1. Random noise slopes of measured data

Phase noise	
Frequency range	dB/dec
10 Hz – 1 kHz	–23.75
1 kHz – 10 kHz	0
10 kHz – 1 MHz	–24

Amplitude noise	
Frequency range	dB/dec
10 Hz – 100 Hz	–10
100 Hz – 10 kHz	0
10 kHz – 1 MHz	–24

The spurs of the deterministic components come from specific periodic sources, including voltage ripple at 50 Hz and vacuum pump vibrations at 10 and 24 Hz. The large spur at ca. 750 kHz corresponds to the $^8/_9\,\pi$ fundamental mode of a TESLA cavity (Vogel (2007)). Importantly, the fact that these noise sources are identifiable can later be leveraged to the advantage of the future beam-based feedback algorithm.

Finally, Figure 3 illustrates the noise of a RF signal in the time domain. Later in this paper it will become clear how these RF fluctuations can have a direct impact on an accelerated electron beam.

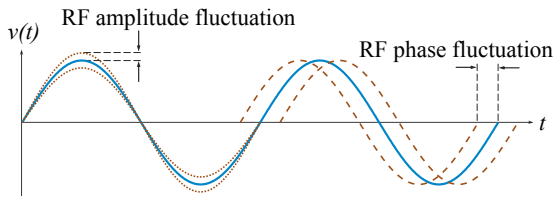

Fig. 3. RF noise in time domain

3. RF NOISE MODELING

A noisy sinusoidal oscillator waveform can be represented as (Demir and Sangiovanni-Vincentelli (1996))

$$v(t) = (A_c + \alpha(t))\cos(2\pi f_c t + \varphi(t) + \phi_0), \tag{2}$$

where A_c is the amplitude and f_c is the frequency of the carrier, ϕ_0 is the initial phase, while $\alpha(t)$ and $\varphi(t)$ are

zero-mean random processes representing the amplitude and phase noise of the oscillator waveform respectively. Therefore, by extracting the random noise definition from (2) and augmenting it with a deterministic zero-mean component we model the amplitude and phase noise as

$$A_n(t) = \alpha(t) + \sum_{i=1}^{n} A_{d_i} \sin(2\pi f_{d_i} t), \tag{3}$$

$$\phi_n(t) = \varphi(t) + \sum_{i=1}^{n} A_{d_i} \sin(2\pi f_{d_i} t), \tag{4}$$

where $A_n(t)$ and $\phi_n(t)$ are the amplitude and phase noise terms acting on the RF electromagnetic field respectively, while A_d is the amplitude and f_d is the frequency of a deterministic noise signal. From (3) and (4) it is now obvious that the RF noise profile observed in Figure 2 shall be modeled by the random processes $\alpha(t)$ and $\varphi(t)$, while the spurious content of the measured RF noise shall be the responsibility of the deterministic sine wave sums.

4. LINEAR ACCELERATOR MODELING

In this paper a linear accelerator shall be modeled in terms of a bunch compressor. Figure 4 schematically demonstrates this concept.

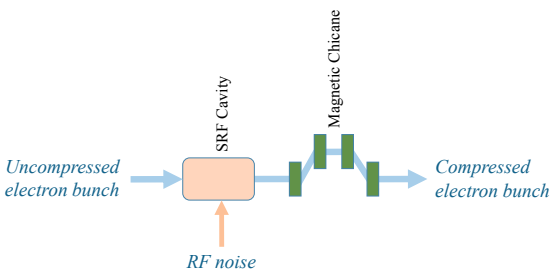

Fig. 4. Schematic of bunch compressor concept

The importance of bunch compression in this context is that the concept describes the interaction between the electron beam and important accelerator structures, namely the RF cavity and the magnetic chicane. Therefore, bunch compression provides a suitable way to analyze the propagation of RF noise to the electron beam. Before going into the modeling details though, it is important to explain why and when longitudinal electron beam dynamics can be expressed using static maps.

4.1 Usage of Static Maps

Unlike a synchrotron where the circulating particles exhibit an inherently periodic longitudinal motion—the so called synchrotron oscillation, a linear accelerator is a single-pass machine, and thus the particles exhibit little to none periodicity in their longitudinal motion (Wille (2000)). Moreover, in case of linear machines that operate with electrons, the latter require relatively low acceleration energies in order to reach the relativistic regime (Rosenzweig (2003)). In this regime the particles travel with almost the speed of light, the space charge effect that makes the particles repel each other becomes negligible, and hence the longitudinal motion inside an electron bunch becomes effectively *'frozen'*. All this leads to the fact that the longitudinal motion of relativistic electrons inside a linear accelerator can be described using static maps.

4.2 Bunch Compression

The process of bunch compression is twofold: 1) first an energy chirp is introduced into the particle distribution of an electron bunch by accelerating the latter off-crest in a RF cavity and 2) then this energy chirp is used to vary the path lengths of the particles in a magnetic chicane in order to bring the particles closer together (Chao et al. (2013)).

When an electron bunch is accelerated off-crest the particles in the head of the bunch see less RF amplitude compared to the particles arriving in the tail of the bunch. This time-energy correlation results in a certain energy distribution along the bunch—the energy chirp. Figure 5 illustrates the off-crest acceleration together with the phase space representation of the resulting energy chirp.

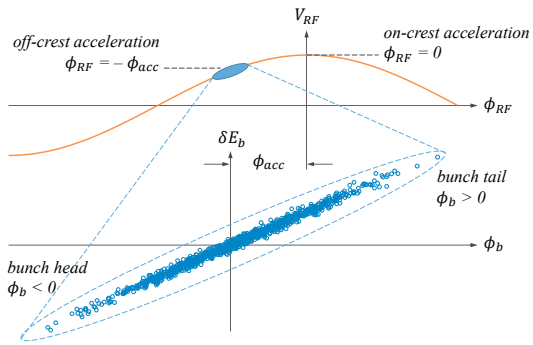

Fig. 5. RF off-crest acceleration and energy chirp

Therefore, mathematically such acceleration and, hence, the RF cavity stage of the bunch compression can be described using the following expression

$$E_f = E_i + eV\cos(\phi), \tag{5}$$

where E_f and E_i are the final and initial energies of the electron bunch particles respectively, V is the amplitude and ϕ is the phase of the RF electromagnetic field, and finally e is the electron charge. From (5) it becomes immediately clear how RF fluctuations demonstrated in Figure 3 can start propagating to the electron bunch.

The second stage of the bunch compression, i.e. the magnetic chicane, uses a static magnetic field to bend the trajectories of the electron bunch particles depending on their energy. The magnets of the chicane are arranged in such a way that the particles with a higher energy take a shorter path through the chicane, while the particles with a lower energy take a longer path. Considering that the energy chirp is imprinted such that the head of the bunch has less energy than the tail results in a situation that the delayed head lets the tail catch up with it, hence the compression of the bunch. The energy dependent path deviation is expressed mathematically as follows

$$z_f = z_i + R_{56}\frac{\Delta E}{E_0}, \tag{6}$$

where z_f and z_i are the final and initial positions of the particles in the electron bunch w.r.t. the mean position respectively, E_0 is the nominal energy of the electron bunch expected at the magnetic chicane, while ΔE is the deviation of the particle energy from this nominal energy, and finally R_{56} is a factor that translates the energy deviation into longitudinal position deviation which is a design parameter of the magnetic chicane. Considering that the energy of the electron bunch may already be disturbed by the RF fluctuations, equation (6) demonstrates how this disturbance is further mapped to longitudinal position fluctuations.

To sum up, (5) and (6) represent the static maps which can be used to model a linear accelerator for the purpose of this paper.

5. SIMULATION MODEL

Following the discussion in Sections 3 and 4 we can now start building a Simulink model as a tool to analyze how the RF noise propagates to the electron beam.

5.1 Top Level Block Diagram

The top level view of the simulation model is depicted in Figure 6. The responsibilities of the presented Simulink blocks are divided as follows

- RF Electromagnetic Field realizes the discussion of Section 3;
- Bunch Compressor contains the necessary logic to implement the linear accelerator modeling presented in Section 4;
- Electron Bunch Timing and Phase Sum will be presented in Section 5.3;
- Beam Diagnostics encapsulates the details of deriving and then plotting the resulting beam properties.

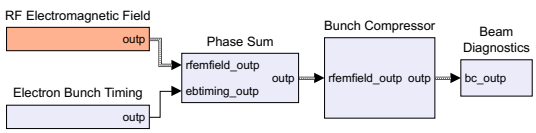

Fig. 6. Top level block diagram in Simulink

Additionally, this simulation model can be run with various parameters as shown in Table 2. Among other parameters the bunch repetition rate is of particular interest in the context of this discussion. Generally speaking, we say that an electron bunch samples the RF electromagnetic field noise, hence the bunch repetition rate is in fact the sampling frequency of this noise. Now as the main noise contribution has a bandwidth below 1 MHz, choosing a bunch repetition rate of 3.25 MHz not only conforms to the rates used at ELBE, but also respects the corresponding Nyquist frequency.

5.2 RF Electromagnetic Field

The RF electromagnetic (EM) field is modeled as a combination of the corresponding amplitude and phase parameters. Since the modeling of these parameters in the context of this paper happens to be quite similar, we start by presenting a generalized Simulink model and in the end introduce model parts that are parameter dependent.

Table 2. Parameters of simulation model

Parameter	Value	Unit
RF frequency	1.3	GHz
RF gradient	8	MV/m
RF phase	–60	degrees
Bunch repetition rate	3.25	MHz
Bunch particle number	1000	dimensionless
Bunch initial duration	3	picoseconds
Bunch initial energy	18	MeV
Bunch initial energy spread	37.2	keV
Magnetic chicane R_{56}	–110	millimeters

Based on (3) and (4) the generation of the RF electromagnetic field parameter, i.e. the amplitude or the phase, can be modeled in Simulink as depicted in Figure 7.

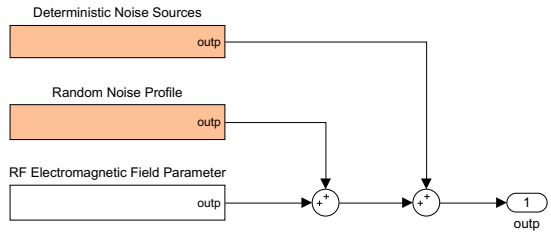

Fig. 7. Generation of RF EM field parameter in Simulink

Moreover, according to (3) and (4) we know that the deterministic noise is modeled as a sum of sine waves. Figure 8 displays a Simulink model that includes three sine wave generators for frequencies: 1) 10 Hz to denote a vacuum pump, 2) 50 Hz to describe voltage ripple and 3) 750 kHz to indicate the above-mentioned $^8/_9\ \pi$ fundamental cavity mode. These sources are represented by idealized sinusoidal waveforms with the amplitudes calculated as

$$A_i = \sqrt{\alpha 10^{\frac{M_i + \frac{N_0}{2}}{10}} w}, \tag{7}$$

where M_i is the magnitude of a spur in dBc/Hz units as observed in Figure 2, while A_i is the amplitude of the corresponding sine wave in volts, α is a dimensionless window correction factor (Harris (1978)), w is the resolution bandwidth of the spectrum analyzer in hertz, and, finally, $\frac{N_0}{2}$ is the two-sided power spectral density of a white Gaussian noise as defined in (8). In comparison, the $\frac{N_0}{2}$ constant in (7) must be specified in decibel units.

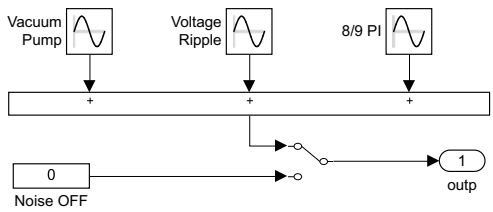

Fig. 8. Generation of deterministic RF noise in Simulink

Furthermore, from (3) and (4) we also remember that the random component, i.e. $\alpha(t)$ or $\varphi(t)$, is a zero-mean

random process that represents the corresponding amplitude and phase noise. Obviously, such definition can be modeled as a white Gaussian noise filtered according to the measured shape presented in Figure 2. Consequently, this concept can be implemented in Simulink as demonstrated in Figure 9.

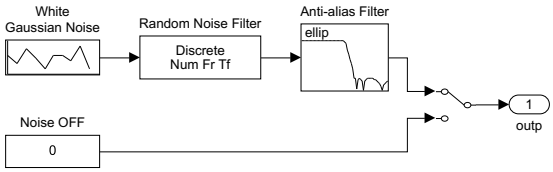

Fig. 9. Generation of random RF noise in Simulink

The variance of the white Gaussian noise is specified as (Ziemer and Tranter (2014))

$$\sigma^2 = 2\frac{N_0}{2}B, \tag{8}$$

where B is the bandwidth of the noise profile in hertz, while $\frac{N_0}{2}$ is the two-sided power spectral density of the white noise process in watts, and since we are only interested in a one-sided spectrum we double this constant. In this simulation we use variance with $\frac{N_0}{2}$ constant being equal to 1.

Regarding the random noise filter, Table 1 shows that the measured random noise shapes have regions with slopes that cannot be precisely described by the linear time-invariant (LTI) systems that adhere to the $n{\cdot}20$ dB/dec rule with $n \in \mathbb{Z}$. Still, such problems have been solved before using fractional order modeling (Heuer et al. (2014)). Therefore, we define a fractional order transfer function for the amplitude noise using FOMCON toolbox (Tepljakov et al. (2019)) as

$$W_a(s) = 1.44 \cdot 10^{-2} \frac{\left(s^{0.82} + 6.28 \cdot 10^2\right)}{\left(s^{0.75} + 62.8\right)\left(s^{1.124} + 1.8 \cdot 10^5\right)}. \tag{9}$$

Likewise, the phase noise shape filter is defined by its fractional order transfer function as

$$W_\phi(s) = 6.18 \cdot 10^{-2} \frac{\left(s^{1.05} + 1.257 \cdot 10^4\right)}{\left(s^{1.1} + 62.8\right)\left(s^{1.115} + 2.2 \cdot 10^5\right)}. \tag{10}$$

In this work both transfer functions were tuned empirically. Figures 10 and 11 show the magnitude frequency response of (9) and (10) respectively. The corresponding measured RF noise shapes are added to these Figures in order to validate the filter shapes.

5.3 Electron Bunch Timing

The arrival time of relativistic electron bunches can be related to phase in radians as

$$\phi_{bunch}(t) = t_{arr} \cdot \omega(t), \tag{11}$$

where $\omega(t)$ is the angular frequency of the arriving electron bunches, while t_{arr} is the arrival time itself. Conceptually, this electron bunch phase is very important since it directly affects the accelerating RF phase. By extending (5) this concept can be analytically expressed as

$$E_f = E_i + eV\cos\left(\phi_{RF} + \phi_{bunch}\right). \tag{12}$$

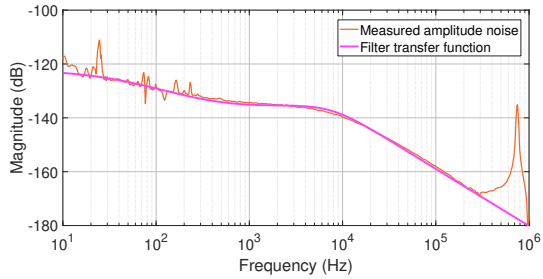

Fig. 10. Bode plot of random amplitude noise filter

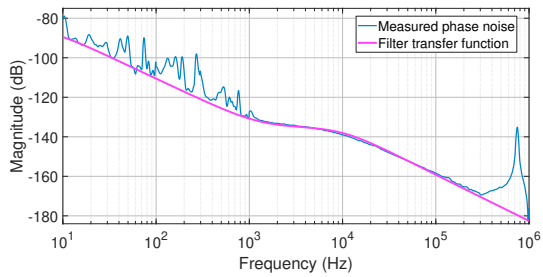

Fig. 11. Bode plot of random phase noise filter

In terms of Simulink modeling this phase sum concept is implemented in Phase Sum block seen in Figure 6.

Now, regarding the electron bunch phase, or timing, block Electron Bunch Timing displayed in Figure 6 models this input beam parameter as illustrated in Figure 12. In the presented block diagram we can clearly see the reuse of the methods developed in Section 5.2. Consequently, the noise placeholders allow straightforward extension of the model by beam arrival time instabilities.

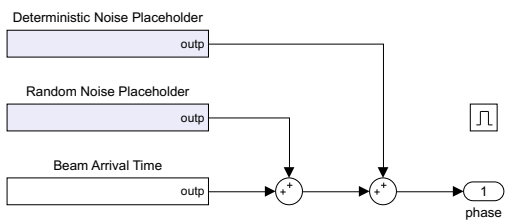

Fig. 12. Simulink model of electron bunch timing

5.4 Bunch Compressor

Modeling (5) and (6) using Simulink blocks results in a bunch compressor model demonstrated in Figure 13. While blocks RF Cavity Map and Magnetic Chicane Map implement the corresponding analytic expressions, block Electron Bunch Gun simply outputs an electron bunch in a phase space representation, i.e. two vectors with a Gaussian distribution: 1) for the particle longitudinal positions inside the bunch w.r.t. the mean position and 2) for the absolute energies of these particles. The size of these phase space vectors corresponds to the number of particles specified in Table 2.

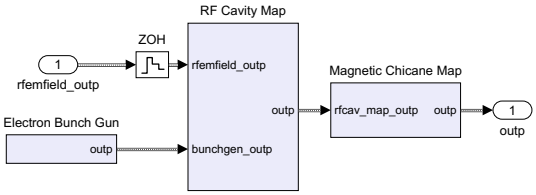

Fig. 13. Bunch compressor modeled in Simulink

Furthermore, block ZOH, i.e. zero-order hold, makes the bunch compressor model effectively discrete. The sampling frequency corresponds to the specified bunch repetition rate in Table 2. Indeed, by letting the bunch compressor model periodically sample the RF electromagnetic field with the actual bunch repetition rate we mimic how an electron bunch travels through this accelerator structure sampling potential RF disturbances along the way.

5.5 Beam Diagnostics

As stated in Section 5.4 the electron bunches emitted by Electron Bunch Gun block have phase space representation. When traversing RF Cavity and Magnetic Chicane blocks this initial electron phase space will change resulting in a final phase space which corresponds to a compressed electron bunch. Consequently, when Beam Diagnostics block receives these compressed electron bunches, the derivation of the bunch energy, arrival time and duration becomes merely a manipulation of the final phase space representation using formulae (13), (14) and (15) respectively

$$\langle E \rangle = \frac{1}{n} \sum_{i=1}^{n} E_i, \tag{13}$$

$$\langle t \rangle = \frac{1}{c} \frac{1}{n} \sum_{i=1}^{n} z_i, \tag{14}$$

$$\sigma_t = \frac{1}{c} \sqrt{\frac{1}{n-1} \sum_{i=1}^{n} (z_i - \langle z \rangle)^2}, \tag{15}$$

where E_i is the absolute energy of the i-th particle inside an electron bunch in electron-volts and $\langle E \rangle$ is the mean energy of the whole ensemble of particles; z_i is the longitudinal position of the i-th particle within an electron bunch in meters w.r.t. the mean position, c is the speed of light and $\langle t \rangle$ is the mean position converted into time in seconds; finally, σ_t is the standard deviation of the longitudinal particle positions inside the bunch converted into time in seconds.

6. SIMULATION RESULTS

The simulation model described in Section 5 produces RF noise with a frequency spectrum displayed in Figure 14. The resolution bandwidth of the spectrum analyzer was set to 1 Hz. The addition of the measured RF noise to this illustration validates the correctness of the developed RF noise shape filters. Moreover, the decibel levels of the simulated spurious content correspond to the measured ones which shows the correctness of (7). Without loss of generality the simulated spurious content is represented only by the spurs introduced in Section 5.2 plus the vacuum pump vibrations at 24 Hz for the amplitude noise.

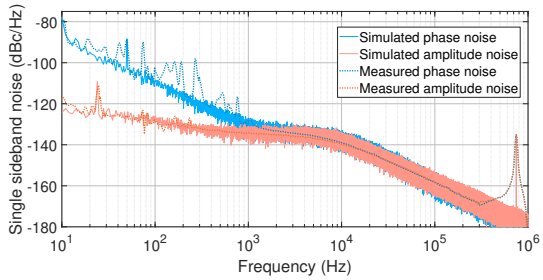

Fig. 14. Simulated RF noise frequency spectrum

Afterward, the amplitude and phase noise components were separately applied to the electron beam properties, such as energy, duration and arrival time. The resulting frequency spectra can be observed in Figures 15 and 16. The direct correspondence of these output spectra to the input one shown in Figure 14 clearly underscores the static behavior of the bunch compressor. The only detail that can change in this case is the scaling—an inherent feature of a static system. Obviously, this scaling also depends on the units of the beam properties, hence the specification of the units on the plots.

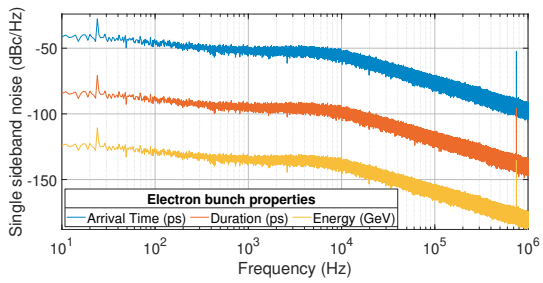

Fig. 15. RF amplitude noise applied to beam properties

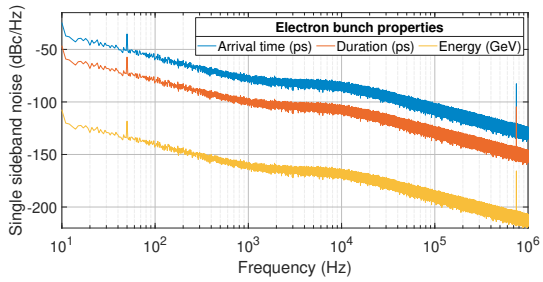

Fig. 16. RF phase noise applied to beam properties

Finally, running the simulation with both RF noise components applied to the electron beam properties produces the result presented in Figure 17. A noteworthy observation is that the energy and arrival time properties of an electron bunch seem to follow the amplitude noise dynamics, while the duration property appears to be influenced by the

phase noise dynamics. Additional sensitivity analysis may be required to explain this observation.

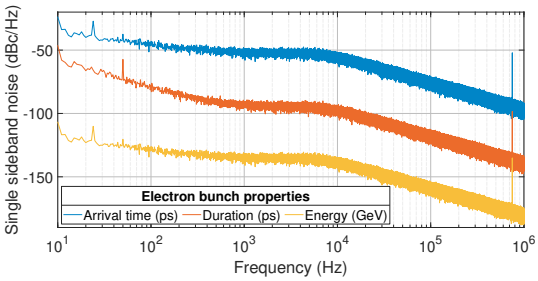

Fig. 17. RF noise applied to beam properties

7. CONCLUSIONS

A proper understanding of the contribution of RF noise to the development of electron beam instabilities is essential in order to design an efficient beam-based feedback control algorithm. Moreover, the relevance of this understanding is supported by the fact that every particle accelerator in the world, including the superconducting electron linear accelerator ELBE, is considered unique, hence no general control solution exists.

In this paper we used the RF noise data measured at one of the superconducting RF cavities installed at ELBE in order to build a Simulink model that could help analyzing the propagation of the RF noise to the electron beam properties. Using this simulation model we showed that from a control point of view an electron bunch compressor of a linear accelerator operating on relativistic particles exhibits a static behavior. Therefore, there is a direct correlation between the frequency spectra of the RF noise and the electron beam properties.

Furthermore, the presented measurement data highlighted the fact that simple LTI systems do not allow precise description of the RF phase noise shapes. Hence, fractional order modeling was used to design the noise shape filters. Admittedly, fractional order systems are appropriate candidates to describe phase noise dynamics.

As the next step we could use the insight into the RF noise frequency content to interpret the perspective beam-based feedback as a disturbance rejection control problem. By utilizing the developed RF noise filters as frequency dependent disturbance weights the control problem could be generalized to enable modern control methods, such as the $\mathcal{H}_2$ optimal control in a S/KS mixed-sensitivity design formulation. Therefore, the controller synthesis would amount to minimizing the impact of the RF disturbance on the weighted combination of the beam performance and the corresponding control effort.

8. ACKNOWLEDGMENTS

This work was supported by the Estonian Research Council grant PRG658.

REFERENCES

Chao, A.W., Mess, K.H., Tigner, M., and Zimmermann, F. (2013). *Handbook of Accelerator Physics and Engineering*. World Scientific Publishing, 2 edition.

Demir, A. and Sangiovanni-Vincentelli, A.L. (1996). Simulation and Modeling of Phase Noise in Open-Loop Oscillators. In *Proceedings of Custom Integrated Circuits Conference*, 453–456. doi:10.1109/CICC.1996.510595.

Feldhaus, G. and Roth, A. (2016). A 1 MHz to 50 GHz Direct Down-Conversion Phase Noise Analyzer with Cross-Correlation. In *2016 European Frequency and Time Forum (EFTF)*, 1–4. doi:10.1109/EFTF.2016.7477759.

Garoby, R. (1992). *Frontiers of Particle Beams: Intensity Limitations*, chapter Beam loading in RF cavities, 509–541. Springer Berlin Heidelberg. doi:10.1007/3-540-55250-2_42.

Harris, F.J. (1978). On the Use of Windows for Harmonic Analysis with the Discrete Fourier Transform. *Proceedings of the IEEE*, 66(1), 51–83. doi:10.1109/PROC.1978.10837.

Heuer, M., Lichtenberg, G., Pfeiffer, S., Schlarb, H., Schmidt, C., and Werner, H. (2014). Modeling of the Master Laser Oscillator Phase Noise for the European XFEL using Fractional Order Systems. *IFAC Proceedings Volumes*, 47(3), 9235–9240. doi:10.3182/20140824-6-ZA-1003.00775.

IEEE Standard 1139-2008 (2009). IEEE Standard Definitions of Physical Quantities for Fundamental Frequency and Time Metrology—Random Instabilities. Standard, IEEE Standards Coordinating Committee 27.

Pfeiffer, S. (2014). *Symmetric Grey Box Identification and Distributed Beam-Based Controller Design for Free-Electron Lasers*. Ph.D. thesis, Hamburg University of Technology.

Rezaeizadeh, A., Schilcher, T., and Smith, R. (2015). MPC based Supervisory Control Design for a Free Electron Laser. In *Proc. 54th IEEE Conf. Decision and Control*, 1682–1686. doi:10.1109/CDC.2015.7402452.

Rosenzweig, J.B. (2003). *Fundamentals of Beam Physics*. Oxford, UK: University Press.

Schilcher, T. (1998). *Vector Sum Control of Pulsed Accelerating Fields in Lorentz Force Detuned Superconducting Cavities*. Ph.D. thesis, Hamburg University.

Schmidt, C. (2010). *RF System Modeling and Controller Design for the European XFEL*. Ph.D. thesis, Hamburg University of Technology.

Tepljakov, A., Petlenkov, E., and Belikov, J. (2019). *Handbook of Fractional Calculus with Applications*, chapter FOMCON toolbox for modeling, design and implementation of fractional-order control systems, 211–236. De Gruyter.

Vogel, E. (2007). High gain proportional rf control stability at TESLA cavities. *Physical Review Special Topics - Accelerators and Beams*, 10. doi:10.1103/PhysRevSTAB.10.052001.

Wille, K. (2000). *The Physics of Particle Accelerators: An Introduction*. Oxford University Press.

Ziemer, R. and Tranter, W. (2014). *Principles of Communications*. Wiley Publishing, 7 edition.

Appendix 4

II

A. Maalberg, M. Kuntzsch, and E. Petlenkov. Regulation of the Linear Accelerator ELBE Exploiting Continuous Wave Mode of a Superconducting RF Cavity. In *Proc. 2022 Am. Control Conf.*, pages 5346–5353, Jun 2022

2022 American Control Conference (ACC)
Atlanta, USA, June 8-10, 2022

Regulation of the Linear Accelerator ELBE Exploiting Continuous Wave Mode of a Superconducting RF Cavity

Andrei Maalberg, Michael Kuntzsch and Eduard Petlenkov

***Abstract*— Scientific experiments conducted with the help of a particle accelerator rely on the stability of the corresponding particle beam. One way of improving this stability is the application of a control method called beam-based feedback. Following this, the control system of the linear accelerator ELBE is planned to be upgraded by this feedback mechanism. This paper exploits the continuous wave operation mode of ELBE in order to reinterpret the given control problem as a disturbance rejection goal. In this context, the paper studies the influence of stochastic disturbances on electron beam arrival time, proposes and designs a control system that is capable of effectively compensating the arrival time fluctuations. Moreover, the prospective hardware implementation is taken into account when choosing the most suitable control strategy for this specific task. Finally, the simulation of the designed regulator on measured disturbance data indicates an improvement in arrival time performance.**

I. Introduction

Radio frequency (RF) particle accelerators are used for a variety of research purposes, including cancer research and high energy physics. By using RF electromagnetic fields these machines accelerate charged particles to high energies while forming the particles into well-defined beams. Subsequently, an accelerated particle beam can be utilized to create a secondary beam of ultra-short photon pulses, thus providing a light source for scientific experiments [1]. Figure 1 illustrates a conceptual schematic of such a light source.

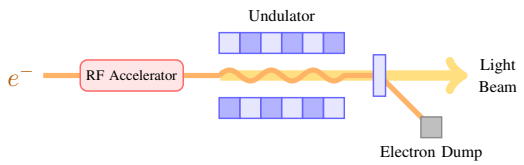

Fig. 1. Conceptual schematic of a light source

The Electron Linear accelerator for beams with high Brilliance and low Emittance (ELBE) is a versatile light source located at Helmholtz-Zentrum Dresden-Rossendorf (HZDR), Germany. As depicted in Figure 2 the general layout of ELBE THz beamline follows the conceptual schematic of a light source, namely: 1) electron bunches are first produced by an electron gun, 2) these electron bunches are then accelerated with the help of RF linacs consisting of superconducting RF cavities, and 3) photons are finally generated from these accelerated electron bunches inside an undulator.

ELBE is one of the few electron linear accelerators routinely operated in a continuous wave (CW) mode. The notion of CW refers to a specific machine operation mode in which the RF electromagnetic field that resonates inside an accelerating RF cavity is driven continuously. Compared to the more common pulsed mode, the CW allows flexible electron bunch repetition rates and high average current, thus enabling experiments that would otherwise be impossible to perform, hence the versatility.

Still, the quality of experimental results depends on the stability of the accelerated electron beam. For example, a pump-probe experiment [2] may be configured to expect an electron bunch to arrive at the undulator with precise periodicity. In case this arrival time fluctuates due to the instability of the corresponding electron beam, then this fluctuation is transferred to the subsequent secondary radiation, and the quality of the experimental data degrades. Since the process of RF acceleration is affected by various disturbances [3], including the inherent RF noise and the noise coming from the electron gun, regulation of the electron beam becomes crucial. The existing low-level RF (LLRF) control scheme installed at ELBE [4] represents the state of the art. Such controller operates only in terms of the accelerating RF field and therefore lacks any feedback from the electron beam. Consequently, the control scheme at ELBE is planned to be upgraded by a beam-based feedback (BBF) controller. This new controller must be realized as a RF cavity setpoint correction law based on the measurement data coming from the electron beam. Even though the field of linear accelerators already lists a number of BBF control designs [5], [6], [7], [8], [9], these examples target pulsed machines. Yet ELBE is operated in CW mode, so it is of interest to study the implications of this machine operation mode in the context of the given control problem.

Provided the given control problem is addressed directly, i.e. a bunch-by-bunch control is pursued, the respective controller will then need to act at least twice as fast as the corresponding bunch repetition rate, and at ELBE the CW operation allows this rate to range from 50 kHz to 26 MHz. Depending on the chosen control algorithm the digital implementation may become a challenge to meet the required sample time. More important though is the fact that this

This work was partially supported by the Estonian Research Council under Grant PRG658

A. Maalberg and M. Kuntzsch are with Helmholtz-Zentrum Dresden-Rossendorf, 01328 Dresden, Germany {a.maalberg,m.kuntzsch}@hzdr.de

E. Petlenkov is with Department of Computer Systems, Tallinn University of Technology, 19086 Tallinn, Estonia eduard.petlenkov@taltech.ee

Authorized licensed use limited to: Helmholtz-Zentrum Dresden-Rossendorf. Downloaded on September 06,2022 at 12:55:34 UTC from IEEE Xplore. Restrictions apply.

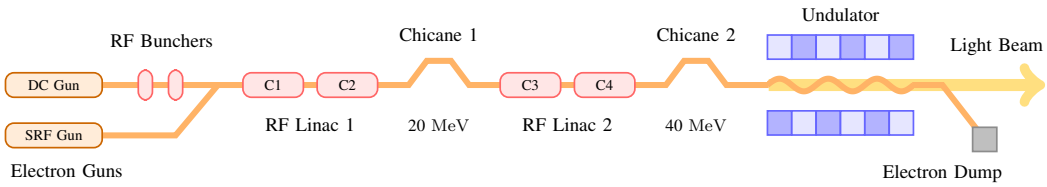

Fig. 2. General layout of ELBE

direct approach is fundamentally limited by the bandwidth of the actuator—a superconducting RF cavity has a bandwidth of a couple hundred hertz only [10]. Even when driven by a dedicated LLRF controller that pushes this bandwidth to a few kilohertz, the cavity dynamics remains a limitation.

On the other hand, CW allows treating a RF accelerator machine as a plant operating in a steady state mode. Hence, the given control problem may be reinterpreted as a regulation goal with the focus of attention moved to a particular disturbance that affects the electron beam. ELBE machine study [3] shows that among other noise sources, such as microphonics and Lorentz force detuning, RF noise makes a significant contribution to the overall electron beam noise with the major contributors residing below 1 kHz. By approximating the frequency spectra of this RF noise using fractional-order systems a subsequent study [11] builds a model that demonstrates the RF noise propagation to electron beam properties, including the beam arrival time. Consequently, when the given control problem is approached from this alternative perspective, the CW mode with its continuous operation becomes favorable as it reveals the full spectrum of disturbances, low frequency ones included. Furthermore, by targeting the actual electron beam disturbance that mostly resides in the low frequency range the bandwidth limitation dictated by the superconducting RF cavity no longer poses a problem, thus making the design and implementation of a corresponding regulator feasible. Therefore, in this paper we develop this approach further. Based on the stochastic nature of RF noise we propose an optimal $\mathcal{H}_2$ regulator design that 1) takes the disturbance model explicitly into account and 2) focuses on the compensation of beam arrival time fluctuations. Finally, we show the applicability of the proposed method by validating the designed regulator on measurement data.

The remainder of this paper is organized as follows: Section II elaborates the discussion regarding the actuator together with its inherent limitations and noise. The proposed regulator design is described in detail in Section III. Finally, Section IV concludes the paper.

II. RF Cavity as Actuator for Beam Regulation

RF accelerators use RF electromagnetic fields to accelerate charged particles. In case of ELBE the process of electron acceleration is carried out by four TESLA cavities [12]. Figure 3 illustrates a standard 9-cell TESLA cavity housing standing electromagnetic waves. Since the RF fields inside the cavity cells are phase shifted relative to each other by 180 degrees, hence the name π-mode, a relativistic electron bunch that traverses such cavity at the speed of light will see the accelerating voltage amplitude nine times in a row, thus becoming increasingly accelerated.

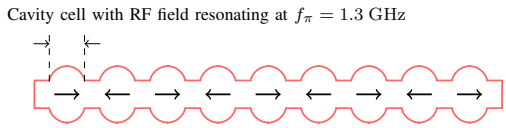

Fig. 3. TESLA cavity housing standing electromagnetic waves

The bandwidth limitation of a superconducting RF cavity comes from its inherently high quality factor. In case of ELBE a TESLA cavity resonating in π-mode at $f_\pi = 1.3$ GHz has a loaded quality factor in the range of $Q_{L\pi} \approx 6.5 \cdot 10^6$ which yields a bandwidth of

$$f_{1/2} = \frac{f_\pi}{2Q_{L\pi}} \approx 100 \text{ Hz}. \tag{1}$$

When the cavity is operated in closed-loop, the gain applied by the dedicated LLRF controller extends the closed-loop bandwidth to the range of $f_{1/2} \approx 35$ kHz which, however, is still insufficient for a direct bunch-by-bunch control.

The reinterpretation of the given control problem as a regulation goal can be performed as follows. The plan to implement the beam-based feedback as a RF setpoint correction law implies that the corresponding control scheme will involve cascaded loops. In case of ELBE it is reasonable to follow the separation of concerns principle and approximate the inner loop, i.e. the actuator, as a unity gain, e.g.

$$\tau_e = G_e \begin{bmatrix} 1 & 0 \\ 0 & 1 \end{bmatrix} \begin{bmatrix} A_{RF} \\ \phi_{RF} \end{bmatrix} = G_e G_{RF} \begin{bmatrix} A_{RF} \\ \phi_{RF} \end{bmatrix}, \tag{2}$$

where A_{RF} and ϕ_{RF} denote RF field amplitude and phase, respectively, G_{RF} is a closed-loop interconnection of a RF cavity model [13] and a LLRF controller [14], and where G_e and τ_e is an electron beam model [11] and arrival time, respectively.

Consequently, the BBF control residing in the outer loop 1) can be separated from possible changes in the LLRF controller design and 2) can concentrate exclusively on the electron beam regulation. This, however, implies that the

Authorized licensed use limited to: Helmholtz-Zentrum Dresden-Rossendorf. Downloaded on September 06,2022 at 12:55:34 UTC from IEEE Xplore. Restrictions apply.

outer loop should have a bandwidth around 3.5 kHz, i.e. one order of magnitude less than the inner loop. Simultaneously, the constrained regulator bandwidth must correspond to the bandwidth of the targeted noise to achieve the regulation goal. This underscores the necessity to analyze the frequency content of the noise, and since the RF field of the cavity is a source of instability by itself, this paper focuses on the related RF noise.

A. RF Noise

An ideal radio frequency signal does not exist in the real world, because typically amplitude and phase fluctuations contaminate the signal. As illustrated in Figure 4, these unwanted fluctuations cause the spectral representation of the signal to contain a spread of spectral lines, both below and above the carrier frequency.

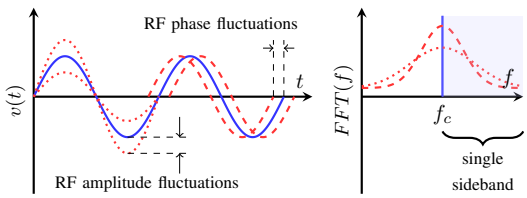

Fig. 4. RF noise in time and frequency domain

According to the standard [15], the spectral components, or sidebands, produced by RF amplitude and phase fluctuations can be represented as one-sided spectral densities S_a and S_ϕ, respectively. Figure 5 presents such spectral densities that were measured at the TESLA cavity C4 during its closed-loop operation.

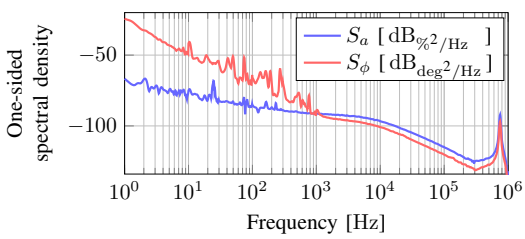

Fig. 5. RF noise frequency spectra measured at ELBE cavity C4

Structurally, the presented amplitude and phase noise frequency data contain two components [11]. These are 1) the random component represented by the spectral profile that decays with certain slopes as the frequency offset increases and 2) the deterministic component that manifests itself as a number of spurs along that profile. Except for the spur at ca. 750 kHz that is caused by the undesired $^8/_9$ π-mode of the TESLA cavity [12], the majority of the spurs are located below 1 kHz, i.e. in a relatively low frequency range. This gives rise to a question whether these low frequencies have any impact on a relativistic electron beam that passes through such TESLA cavity at the speed of light. Being of critical importance for the regulator design, this question can be answered by exemplifying the difference between a pulsed and a CW machine.

B. Example of Electron Beam in Pulsed and CW Modes

Pulsed machines, such as the free electron laser FLASH, organize the electron beam into a temporal structure called a macropulse (MP). During a limited time period dictated by the duration of an accelerating RF pulse a train of electron bunches is injected into the RF cavity. Since the individual electron bunches may be interpreted as discrete pulses, the whole structure is said to form a macropulse. This macropulse is then repeated with a certain periodicity. Furthermore, when an individual electron bunch enters the RF cavity it effectively samples the incident RF field, noise components included. Thus, the above-mentioned discrete pulses, in fact, represent sampled RF field components.

The example starts with a macropulse structure of an electron beam presented both in time and frequency domains, see Figure 6. The parameters of the temporal structure are taken from a typical FLASH configuration [16], i.e. a macropulse that is filled by 800 electron bunches with a 1 microsecond spacing is repeated every 100 milliseconds.

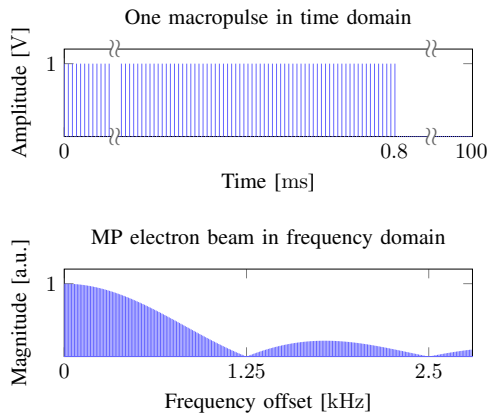

Fig. 6. Example MP structure in time and frequency domains

As can be seen, the exemplified macropulse structure can be treated as a rectangular pulse with a time length $t_{MP} = 800 \cdot 1\ \mu\mathrm{s} = 0.8$ ms. The corresponding frequency domain representation is a sinc pulse with spectrum nulls located at integer multiples of $^1/_{t_{MP}} = 1.25$ kHz. Obviously, the pulse pattern defines a spectral window that limits the signal frequencies that can be resolved using diagnostics. In addition, the signal strength decays as the frequency offset increases. So even though the bandwidth appears to cover the actual region of interest, the diagnostic performance is negatively impacted.

In contrast, the temporal structure of a CW electron beam contains no time gaps, so the RF field is sampled with steady periodicity. This allows to interpret the CW electron beam

Authorized licensed use limited to: Helmholtz-Zentrum Dresden-Rossendorf. Downloaded on September 06,2022 at 12:55:34 UTC from IEEE Xplore. Restrictions apply.

as a sampling mechanism with the corresponding Nyquist frequency. In case of ELBE this frequency is 25 kHz at the lowest bunch repetition rate which is sufficient to properly diagnose the region of interest and hence enable the regulator design. The only thing that is still missing is the way the RF signals, noise included, propagate to electron beam properties.

C. Propagation of RF Field to Electron Beam

Unlike a synchrotron where circulating particles exhibit a periodic longitudinal motion called the synchrotron oscillation, a linear accelerator represents a single pass machine, and hence the particles exhibit little to none periodicity in their longitudinal motion [11]. Moreover, electrons require relatively low acceleration energy to reach a relativistic regime. In this regime the electrons travel with almost the speed of light, the space charge effect that makes these electrons repel each other becomes negligible, and the longitudinal motion inside an electron bunch ceases to exist. Hence, the longitudinal motion of relativistic electrons inside a linear accelerator can be described using static expressions. In particular, a process called bunch compression [17] helps revealing the details of RF field propagation to electron beam properties, namely

$$\Delta\tau_e = \frac{1}{v_e} \cdot R_{56} \cdot \frac{\Delta E}{E_0}, \tag{3}$$

$$\Uparrow$$

$$E_f = E_i + e \cdot A_{RF} \cdot \cos\left(\phi_{RF} + \phi_e\right), \tag{4}$$

$$\Uparrow \qquad \Uparrow$$

$$\delta A_{RF} \qquad \delta\phi_{RF}$$

where E, e, v_e and ϕ_e are the electron energy, charge, velocity and initial arrival time, and where R_{56} and E_0 denote the design parameters of a magnetic chicane, respectively. In (4), RF field fluctuations δA_{RF} and $\delta\phi_{RF}$ start by contaminating the energy E_f received by an electron during acceleration inside a RF cavity. Next, a magnetic chicane translates the resulting energy deviation ΔE into arrival time deviation $\Delta\tau_e$, and thus the fluctuations propagate further, see (3). In case of ELBE a bunch compressor is represented by the C4 and Chicane 2, and this static system can be described using sensitivity coefficients, see Figure 7.

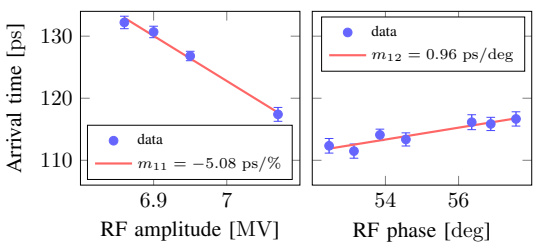

Fig. 7. ELBE sensitivity scan between RF and electron beam arrival time

The coefficients m_{11} and m_{12} were retrieved during a machine study that scanned the response of electron beam arrival time to changes in the RF field of the TESLA cavity C4. Based on these sensitivity coefficients the electron beam model G_e can be identified as a static matrix. Specifically, by considering the current regulation goal the respective propagation of RF field to electron beam arrival time amounts to

$$\tau_e = \overbrace{\begin{bmatrix} m_{11} & m_{12} \end{bmatrix}}^{G_e} \begin{bmatrix} A_{RF} + \delta A_{RF} \\ \phi_{RF} + \delta\phi_{RF} \end{bmatrix}, \tag{5}$$

thus, yielding the complete actuator

$$G = G_e\, G_{RF} = \begin{bmatrix} m_{11} & m_{12} \end{bmatrix} \begin{bmatrix} 1 & 0 \\ 0 & 1 \end{bmatrix}. \tag{6}$$

According to (6), the resulting actuator G exhibits static behavior. As a result, the following regulator design needs to take into account 1) a direct feedthrough in the system and 2) the process disturbance explicitly, because the frequency content of the latter will define the dynamics of the designed regulator.

III. Regulator Design

With the advent of digital controllers into the field of particle accelerators, the corresponding control schemes have gained not only in flexibility, but also in complexity. In case of previously used analog P controllers, the machine operators could manually tune the single gain parameter. With the new controllers such manual tuning is practically impossible [18]. Consequently, the use of optimal $\mathcal{H}_\infty$ control for the purpose of parameter optimization [18], [14], [8] appears as a reasonable choice. In this paper, however, the optimal $\mathcal{H}_2$ control is used not only for the sole purpose of parameter optimization, but because the minimization of the underlying $\mathcal{H}_2$ norm has relevant engineering implications [19] for the current disturbance rejection goal.

A. Disturbance Shaping

The given regulation problem makes it reasonable to assume that the open-loop transfer function, i.e. $L = GK$, follows the magnitude frequency response of the disturbance, namely

$$|L| \approx |G_d|, \tag{7}$$

where G_d is a disturbance shaping filter that can be derived from the existing measurement data, see Figure 5. In this context, the current work reuses the previously developed RF noise shaping filters [11], but adapts them as follows: 1) the fractional-order transfer functions are replaced by third-order integer approximations to streamline the design using existing software [20], and 2) the resulting approximations are constrained in the frequency domain by the targeted closed-loop bandwidth of 3.5 kHz. Figure 8 displays the adapted disturbance filters.

Authorized licensed use limited to: Helmholtz-Zentrum Dresden-Rossendorf. Downloaded on September 06,2022 at 12:55:34 UTC from IEEE Xplore. Restrictions apply.

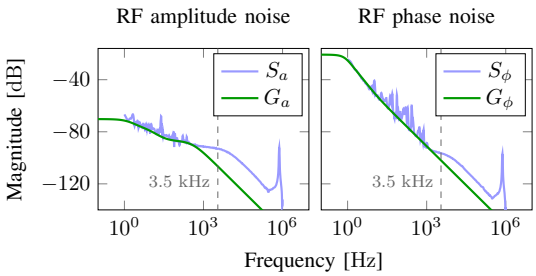

Fig. 8. RF noise approximated by shaping filters G_a and G_ϕ

Subsequently, the presented filters G_a and G_ϕ can be combined with the electron beam sensitivity model G_e yielding the required disturbance shaping filter

$$G_d = W_d\, D_e^{-1} G_e \begin{bmatrix} G_a & 0 \\ 0 & G_\phi \end{bmatrix}, \tag{8}$$

where $W_d = \alpha$, with α a scalar parameter used to emphasize disturbance rejection, and where $D_e = d_{max}$, with d_{max} a scalar parameter used for scaling. Figure 9 displays G_d with $d_{max} = 20$ fs rms, i.e. the acceptable fluctuation of electron beam arrival time.

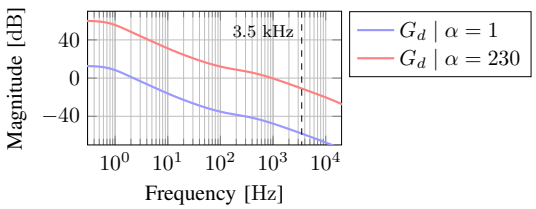

Fig. 9. Disturbance shaping filter G_d with various α to stress regulation

Being based on the RF noise dynamics, G_d inherits the random component, thus, making the modeled electron beam disturbance exhibit stochastic behavior. In fact, this aligns well with the nature of the timing jitter, i.e. the time domain fluctuations of the electron beam arrival time. This jitter is commonly expressed in terms of its rms value. But rms response of a system H driven by white nose excitation is given by its $\mathcal{H}_2$ norm [21]

$$\|H\|_2 \triangleq \left(\frac{1}{2\pi} \int_{-\infty}^{\infty} |H(j\omega)|^2 \, d\omega \right)^{1/2} \tag{9}$$

where $|H(j\omega)|$ designates the magnitude frequency response of H evaluated at frequency ω. Indeed, the presence of RF noise makes the assumption of white noise disturbances relevant in the context of the given problem [19]. This allows to meaningfully apply $\mathcal{H}_2$ regulation method [22] to stabilize the electron beam with respect to RF noise.

B. $\mathcal{H}_2$ Regulator

Table I summarizes the criteria of the designed $\mathcal{H}_2$ regulator.

TABLE I
DESIGN CRITERIA OF $\mathcal{H}_2$ REGULATOR

Design criterion	Requirement
Setpoint tracking	n/a
Disturbance rejection	colored disturbance
Closed-loop bandwidth	3.5 kHz
Discrete sample time	10 µs
Fixed-order	n/a
IO type	SISO
Transfer function optimization	rms response minimization

Setting the sample time to 10 µs gives the prospective digital implementation some timing capacity, in case the bandwidth of the synthesized regulator turns out to be somewhat greater than 3.5 kHz. Furthermore, there is no strict fixed-order requirement, because the designed regulator is going to be implemented on a fast field programmable gate array (FPGA), such as Kintex-7 from Xilinx, and 10 µs is not a challenging sample time. Nevertheless, lower-order designs are favored. In fact, this is the first reason to choose a SISO configuration, as it allows saving on frequency weights. The second reason is that the integration with the existing LLRF implementation becomes more straightforward when the SISO configuration is used. Moreover, colored disturbances coupled with the minimization of the rms response lie at the core of the given regulation problem. Compared to other control algorithm options, the choice of $\mathcal{H}_2$ regulator can be defended as follows

- PID controllers may not be efficient in handling colored disturbances and frequency dependent weighting;
- Robust controllers with uncertainty specifications can become too complex, thus negatively affecting the achievable sample times;
- $\mathcal{H}_\infty$ controllers do not reflect the stochastic specificity of the given regulation problem.

Therefore, Figure 10 displays the resulting regulator design formulated in terms of a typical S/KS mixed-sensitivity optimization problem, but with the addition of the disturbance shaping filter G_d driven by $d = \begin{bmatrix} w & v \end{bmatrix}^T$, where w and v are zero-mean white Gaussian noises with unit variance.

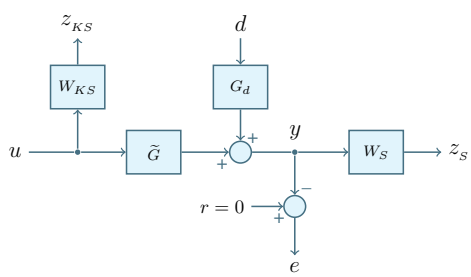

Fig. 10. Design of $\mathcal{H}_2$ regulator

Authorized licensed use limited to: Helmholtz-Zentrum Dresden-Rossendorf. Downloaded on September 06,2022 at 12:55:34 UTC from IEEE Xplore. Restrictions apply.

The presented optimization problem amounts to finding a stabilizing regulator K that minimizes the $\mathcal{H}_2$ norm of the transfer function from the disturbance signal d to the exogenous error signals $\begin{bmatrix} z_S & z_{KS} \end{bmatrix}^T$, i.e.

$$\left\| \begin{bmatrix} W_S S G_d \\ W_{KS} K S G_d \end{bmatrix} \right\|_2, \tag{10}$$

where W_S and W_{KS} are frequency weights for the output y and input u, and where S and KS denote the usual sensitivity and input sensitivity functions, respectively. According to Table I, the actuator is updated as $\widetilde{G} = G\,G_e^{-1}$, thus making $y = \tau_e$ and $u = \tau_e$, and therefore rendering K a single-input single-output regulator. Since G_e is not a square matrix, then its inverse is approximated as

$$G_e^{-1} = \begin{bmatrix} 1/m_{11} & 0 \end{bmatrix}^T. \tag{11}$$

This regulator design puts sufficient effort into shaping L with the help of G_d, hence the weight W_S is omitted, i.e. $W_S = 1$. On the contrary, the weight W_{KS} is a first-order high-pass filter with a corner frequency of 3.5 kHz. This way, W_{KS} helps limiting input magnitudes at high frequencies and thereby limiting the closed-loop bandwidth. The low frequency gain of W_{KS} is set to -100 dB to make sure that the cost function is dominated by G_d at low frequencies.

With the sample time set to 10 µs Matlab function h2syn produces a discrete 7th-order regulator. According to Figure 11, the corresponding transfer functions can be summarized as follows: 1) G_d shapes L as expected from (7), 2) SG_d demonstrates the suppression of G_d up to the closed-loop bandwidth, and 3) this closed-loop bandwidth is experimentally set slightly greater, i.e. around 4.2 kHz.

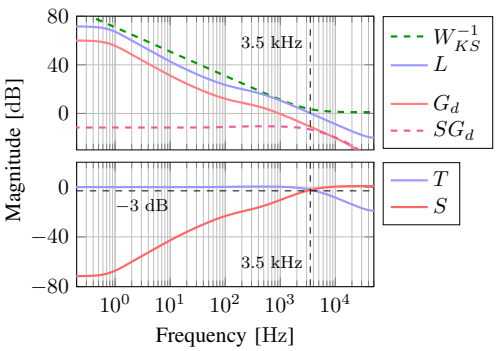

Fig. 11. Transfer functions of discrete $\mathcal{H}_2$ regulator

Moreover, the synthesized regulator has the observer form

$$x[k+1] = Ax[k] + B_2 u[k] + L_x e_x[k], \tag{12}$$
$$u[k] = K_u x[k] + L_u e_u[k], \tag{13}$$

where

$$e_x[k] = y[k] - C_2 x[k] - D_{22} u[k]. \tag{14}$$

Due to G_{RF} approximation as a unity gain, a direct feedthrough appears in the design manifesting itself as $D_{22} \neq 0$. To break the resulting algebraic loop in (13) an additional expression is introduced

$$e_u[k] = y[k] - C_2 x[k] - D_{22} u[k-1], \tag{15}$$

that uses the past control signal $u[k-1]$ to calculate the state estimation error $e_u[k]$. The synthesized regulator can now be validated through simulation.

C. Design Validation

For simulation purposes G_{RF} represents a closed-loop interconnection of a 4th-order LLRF controller and a 6th-order RF cavity model, both discrete and identified at the C4 cavity. The resulting 10th-order model has a sample rate of 1.8 MHz and an internal delay of two sample times. The outer BBF loop is formed by the designed regulator K realized in terms of (12)–(15). Above all, the arrival time disturbance that enters the system is defined by measurement data taken downstream of the C4 cavity [23], [24]. The data is a time domain signal $\delta\tau_e$ sampled at 50 kHz for one second. Figure 12 demonstrates the described simulation scheme.

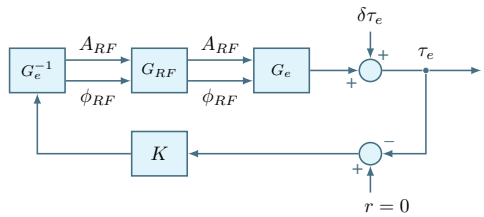

Fig. 12. Simulation scheme to validate regulator K

The simulation is run for one second, and Figure 13 displays the input and output signals of G_{RF}.

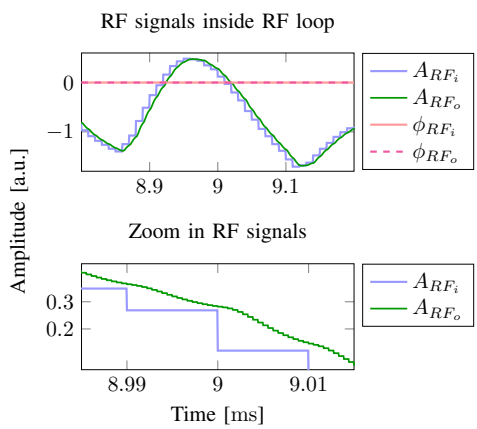

Fig. 13. Driving RF loop signals during simulation

Authorized licensed use limited to: Helmholtz-Zentrum Dresden-Rossendorf. Downloaded on September 06,2022 at 12:55:34 UTC from IEEE Xplore. Restrictions apply.

According to (11), the control is performed only in terms of A_{RF}. In addition, despite having the internal delay, G_{RF} is sufficiently fast to respond to the outer loop commands. Furthermore, Figure 14 demonstrates the performance of the designed regulation system.

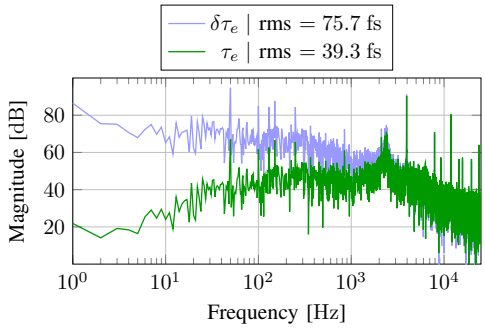

Fig. 14. Validating regulation in frequency domain

As can be seen, the frequency domain profile of the measured disturbance data $\delta\tau_e$ features 1) a random noise component with a moderate slope and 2) a number of deterministic components, including the 50 Hz spur and its harmonics. A large spur around 2.5 kHz is believed to be caused by the measurement procedure. At the same time, it is also seen how the regulator operates within its bandwidth and pushes the coincident noise profile down, thus decreasing the rms metric of the corresponding fluctuations by almost a half. On the one hand, the fact that the low frequency noise is pushed down by approximately 60 decibels corresponds to the capabilities of the designed regulator, see SG_d in Figure 11. On the other hand, the high frequency noise prevails, thus limiting the overall amount of noise that can be suppressed for this particular noise shape.

IV. Conclusions

The CW operation mode of the superconducting linear accelerator ELBE allows reinterpreting a beam-based feedback control problem as a regulation goal. By moving the focus of attention to low frequency RF noise, i.e. the disturbance that makes a significant contribution to electron beam fluctuations, the necessity to pursue a bandwidth-demanding bunch-by-bunch control can be avoided. Simultaneously, the fundamental bandwidth limitation of a superconducting RF cavity, i.e. the usual actuator in such control schemes, no longer poses a problem.

In this paper we proposed a $\mathcal{H}_2$ regulator in order to compensate electron beam arrival time fluctuations with respect to RF noise and its stochastic nature. Using the RF noise shaping filters we augmented a typical S/KS mixed-sensitivity optimization problem, such that our regulator design would take disturbance explicitly into account. The subsequent simulation study that involved measured disturbance data signified an improvement in arrival time performance.

Still, the design decision to approximate the inner RF loop as a unit gain imposed an additional bandwidth constraint on the designed outer loop regulator. In case a particular noise profile had a substantial noise portion residing in the high frequency range, the performance of the regulator could be limited. Such problem could then be solved by using normal conducting RF cavities that have a larger bandwidth that allows targeting the high frequency noise [25], [26].

Our further research will be devoted to implementing the designed regulator on an FPGA. Figure 11 indicates that a lower order of the designed regulator may be sufficient. Provided such simplified solution shows acceptable performance, the implemented algorithm may demonstrate desirable characteristics, such as a reduced usage of FPGA resources and a decreased run-time latency. Subsequently, the implemented result needs to be integrated into the existing digital framework based on MicroTCA.4 technology. Once this is done, the designed regulator can finally be evaluated in practice.

References

[1] B. Green, S. Kovalev, V. Asgekar, G. Geloni, U. Lehnert, T. Golz *et al.*, "High-Field High-Repetition-Rate Sources for the Coherent THz Control of Matter," *Sci. Rep.*, vol. 6, no. 1, 2016.

[2] H. Schlarb, "Techniques for Pump-Probe Synchronisation of Fsec Radiation Pulses," in *Proc. 2005 Particle Accelerator Conf.*, 2005.

[3] M. Kuntzsch, M. Gensch, U. Lehnert, P. Michel, R. Schurig, and J. Teichert, "Jitter Analysis at CW Repetition Rate With Large Spectral Range and High Resolution," in *Proc. 4th Int. Beam Instrumentation Conf.*, 2015.

[4] S. Pfeiffer, J. Branlard, M. Hoffmann, and C. Schmidt, "Advanced LLRF System Setup Tool for RF Field Regulation of SRF Cavities," in *Proc. 19th Int. Conf. RF Superconductivity*, 2019.

[5] S. Pfeiffer, C. Schmidt, M. K. Bock, H. Schlarb, W. Jalmuzna, G. Lichtenberg, and H. Werner, "Fast Feedback Strategies for Longitudinal Beam Stabilization," in *Proc. 2012 Int. Particle Accelerator Conf.*, 2012.

[6] W. Koprek, C. Behrens, M. K. Bock, M. Felber, P. Gessler, K. Hacker *et al.*, "Intra-train Longitudinal Feedback for Beam Stabilization at FLASH," in *Proc. 32nd Int. Free Electron Laser Conf.*, 2010.

[7] A. Rezaeizadeh, T. Schilcher, and R. Smith, "MPC based Supervisory Control Design for a Free Electron Laser," in *Proc. 54th Conf. Decision Control*, 2015.

[8] S. Pfeiffer, H. Werner, C. Schmidt, and H. Schlarb, "Distributed Controller Design for a Free-Electron Laser," in *Proc. 2013 Am. Control Conf.*, 2013.

[9] A. Rezaeizadeh, T. Schilcher, and R. S. Smith, "Adaptive robust control of longitudinal and transverse electron beam profiles," *Phys. Rev. Accel. Beams*, vol. 19, p. 052802, 2016.

[10] T. Schilcher, "Vector Sum Control of Pulsed Accelerating Fields in Lorentz Force Detuned Superconducting Cavities," Ph.D. dissertation, Hamburg University, 1998.

[11] A. Maalberg, M. Kuntzsch, and E. Petlenkov, "Simulation of RF Noise Propagation to Relativistic Electron Beam Properties in a Linear Accelerator," in *Proc. 21st IFAC World Congress*, 2020.

[12] E. Vogel, "High gain proportional rf control stability at TESLA cavities," *Phys. Rev. ST Accel. Beams*, vol. 10, p. 052001, 2007.

[13] S. Pfeiffer, C. Schmidt, G. Lichtenberg, and H. Werner, "Grey Box Identification for the Free Electron Laser FLASH exploiting Symmetries of the RF-System," in *Proc. 18th IFAC World Congress*, 2011.

[14] S. Pfeiffer, G. Lichtenberg, C. Schmidt, H. Schlarb, and H. Werner, "Design of an Optimal and Robust Controller for a Free-Electron Laser Exploiting Symmetries of the RF-System," in *Proc. 51st Conf. Decision Control*, 2012.

[15] IEEE Standard 1139-2008, "IEEE Standard Definitions of Physical Quantities for Fundamental Frequency and Time Metrology—Random Instabilities," IEEE Standards Coordinating Committee 27, Standard, 2009.

Authorized licensed use limited to: Helmholtz-Zentrum Dresden-Rossendorf. Downloaded on September 06,2022 at 12:55:34 UTC from IEEE Xplore. Restrictions apply.

[16] K. Tiedtke, A. Azima, N. von Bargen, L. Bittner, S. Bonfigt, S. Düsterer *et al.*, "The soft x-ray free-electron laser FLASH at DESY: beamlines, diagnostics and end-stations," *New J. Phys.*, vol. 11, no. 2, 2009.

[17] P. Emma, *Handbook of Accelerator Physics and Engineering*, 2nd ed. World Scientific Publishing Co. Pte. Ltd., 2013, ch. Bunch Compression, pp. 334–337.

[18] C. Schmidt, G. Lichtenberg, W. Koprek, W. Jalmuzna, H. Werner, and S. Simrock, "Parameter Estimation and Tuning of a Multivariable RF Controller with FPGA technique for the Free Electron Laser FLASH," in *Proc. 2008 Am. Control Conf.*, 2008.

[19] S. Skogestad and I. Postlethwaite, *Multivariable Feedback Control: Analysis and Design*, 2nd ed. John Wiley & Sons, Ltd, 2005.

[20] G. J. Balas, A. K. Packard, M. G. Safonov, and R. Y. Chiang, "Next generation of tools for robust control," in *Proc. 2004 Am. Control Conf.*, 2004.

[21] S. Boyd and C. Barratt, *Linear Controller Design: Limits of Performance*. Prentice-Hall, 1991.

[22] H. Kwakernaak, "$\mathcal{H}_2$-Optimization—Theory and Applications to Robust Control Design," *IFAC Proceedings Volumes*, 2000.

[23] S. Kovalev, B. Green, T. Golz, S. Maehrlein, N. Stojanovic, A. S. Fisher *et al.*, "Probing ultra-fast processes with high dynamic range at 4th-generation light sources: Arrival time and intensity binning at unprecedented repetition rates," *Struct. Dyn.*, vol. 4, no. 2, 2017.

[24] M. Chen, J.-C. Deinert, B. Green, Z. Wang, I. Ilyakov, N. Awari *et al.*, "Pulse- and field-resolved THz-diagnostics at 4th generation lightsources," *Opt. Express*, vol. 27, no. 22, 2019.

[25] S. Pfeiffer, J. Branlard, L. Butkowski, M. Hierholzer, M. Hoffmann, K. Honkavaara *et al.*, "Status Update of the Fast Energy Corrector Cavity at FLASH," in *Proc. 29th Linear Accelerator Conf.*, 2018.

[26] S. Pfeiffer, L. Butkowski, M. Czwalinna, B. Dursun, C. Gerth, B. Lautenschlager *et al.*, "Longitudinal Intra-train Beam-Based Feedback at FLASH," in *Proc. 39th Free Electron Laser Conf.*, 2019.

Authorized licensed use limited to: Helmholtz-Zentrum Dresden-Rossendorf. Downloaded on September 06,2022 at 12:55:34 UTC from IEEE Xplore. Restrictions apply.

Appendix 5

III

A. Maalberg, M. Kuntzsch, and E. Petlenkov. Real-Time Regulation of Beam-Based Feedback: Implementing an FPGA Solution for a Continuous Wave Linear Accelerator. *Sensors*, 22(16):6236, Aug 2022

sensors

MDPI

Article

Real-Time Regulation of Beam-Based Feedback: Implementing an FPGA Solution for a Continuous Wave Linear Accelerator

Andrei Maalberg [1,*], Michael Kuntzsch [1] and Eduard Petlenkov [2]

[1] Helmholtz-Zentrum Dresden-Rossendorf, 01328 Dresden, Germany
[2] Department of Computer Systems, Tallinn University of Technology, 19086 Tallinn, Estonia
* Correspondence: a.maalberg@hzdr.de

Abstract: Control applications targeting fast industrial processes rely on real-time feasible implementations. One of such applications is the stabilization of an electron bunch arrival time in the context of a linear accelerator. In the past, only the electric field accelerating the electron bunches was actively controlled in order to implicitly stabilize the accelerated electron beam. Nowadays, beam properties are specifically measured at a target position and then stabilized by a dedicated feedback loop acting on the accelerating structures. This dedicated loop is usually referred to as a beam-based feedback (BBF). Following this, the control system of the electron linear accelerator for beams with high brilliance and low emittance (ELBE) is planned to be upgraded by the BBF, and the problem of implementing a designed control algorithm becomes highly relevant. In this work, we propose a real-time feasible implementation of a high-order $\mathcal{H}_2$ regulator based on a field-programmable gate array (FPGA). By presenting simulation and synthesis results made in hardware description language (HDL) VHDL, we show that the proposed digital solution is fast enough to cover the bunch repetition rates frequently used at ELBE, such as 100 kHz. Finally, we verify the implementation by using a dedicated FPGA testbench.

Keywords: regulation; beam-based feedback; FPGA; linear accelerator; continuous wave

check for updates

Citation: Maalberg, A.; Kuntzsch, M.; Petlenkov, E. Real-Time Regulation of Beam-Based Feedback: Implementing an FPGA Solution for a Continuous Wave Linear Accelerator. *Sensors* **2022**, 22, 6236. https://doi.org/10.3390/s22166236

Academic Editor: Roberto Teti

Received: 27 July 2022
Accepted: 17 August 2022
Published: 19 August 2022

Publisher's Note: MDPI stays neutral with regard to jurisdictional claims in published maps and institutional affiliations.

Copyright: © 2022 by the authors. Licensee MDPI, Basel, Switzerland. This article is an open access article distributed under the terms and conditions of the Creative Commons Attribution (CC BY) license (https://creativecommons.org/licenses/by/4.0/).

1. Introduction

Radio frequency (RF) particle accelerators employ RF electromagnetic fields to accelerate charged particles to high energies while forming the particles into well-defined beams. A beam of accelerated particles can then be used to create a secondary radiation of ultra-short photon pulses, thus providing a light source for scientific experiments. Figure 1 illustrates a conceptual schematic of such a light source.

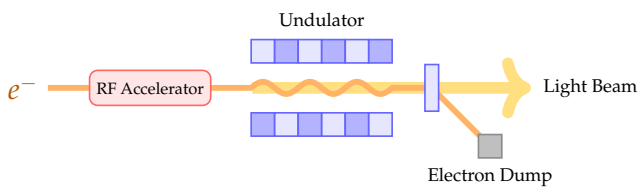

Figure 1. Conceptual schematic of an accelerator driven light source.

ELBE is a versatile light source located at Helmholtz-Zentrum Dresden-Rossendorf (HZDR), Germany. As illustrated in Figure 2, the general layout of the ELBE THz beamline follows the concept of a light source, namely: (1) electron bunches are generated by an electron gun, (2) these electron bunches are accelerated with the help of RF linacs consisting of superconducting RF cavities, and (3) photons are produced from these accelerated electron bunches inside a periodic magnetic structure, called undulator.

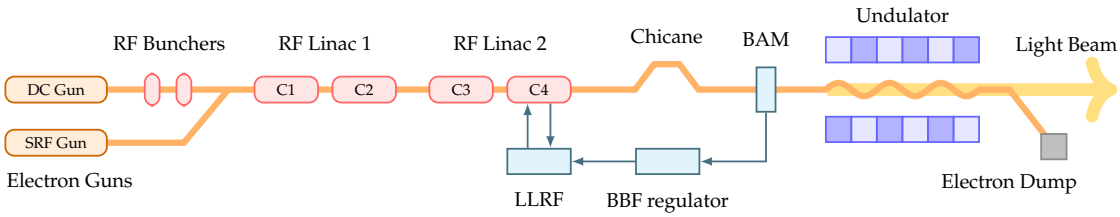

Figure 2. General layout of ELBE THz beamline featuring beam-based feedback regulation loop.

ELBE is one of the few electron linear accelerators routinely operated in a continuous wave (CW) mode. The notion of CW refers to a specific machine operation mode in which the RF electromagnetic field that resonates inside an accelerating RF cavity is driven continuously. Compared to a more common pulsed mode, CW allows flexible electron bunch repetition rates and high average current, thus enabling experiments that would otherwise be impossible to perform, hence the versatility.

Still, the quality of experimental results depends on the stability of the accelerated electron beam. For example, a time-resolved pump-probe experiment [1] may be configured to expect an electron bunch to arrive at the undulator with precise timing. In case this arrival time fluctuates due to the instability of the corresponding electron beam, this fluctuation is transferred to the subsequent secondary radiation, and the time resolution of such experiments degrades. Since the process of RF acceleration is affected by various disturbances, including RF noise inherent to RF acceleration modules and drifts caused by changes in ambient temperature, regulation of the electron beam becomes crucial.

The existing low-level RF (LLRF) controller installed at ELBE [2,3] represents the state of the art. The controller deals with stabilizing the RF field that accelerates the electron beam. However, such control scheme has no feedback from the electron beam, and thus there is no way to stabilize the electron beam directly. To overcome this limitation, the control scheme at ELBE is planned to be upgraded by a beam-based feedback (BBF) regulator, see Figure 2. This regulator is expected to minimize the impact of disturbances acting on the electron beam. In our previous work [4], we proposed a regulator design that seeks to minimize the fluctuations of beam arrival time with respect to low frequency RF noise. Due to CW mode, it was possible to target specific noise profiles, the low frequency ones included. This suggested the application of modern control techniques, such as optimal $\mathcal{H}_2$ control [5,6], which finally resulted in a high-order state-space regulator. Even though the field of linear accelerators already lists a number of BBF control designs [7–10], these examples target pulsed machines. Yet ELBE is operated in CW mode, and very few studies [11] address real-time feasible implementations targeting CW machines. Especially, when the corresponding sample times are on a sub-microsecond level.

The bunch arrival time monitor (BAM) [12–14] measures the arrival time of every electron bunch accelerated inside the machine. This implies that the sample time of the regulator must correspond to the bunch repetition rate. Since this rate may reach several megahertz, the actual sample time requirement is forced to the sub-microsecond level. Obviously, such regulator requires an efficient, yet adjustable implementation of its algorithm, thus strongly suggesting an FPGA-based solution. In fact, low latency and high reconfigurability—the outstanding features of FPGAs—facilitated the adoption of FPGA-based solutions by the accelerator community [15–18]. As a result, the LLRF controller and BAM digital signal processing are implemented on FPGAs as well, thus establishing a low-latency digital signal path on the inputs and outputs of the regulator. It is therefore natural to follow the same trend and implement the regulator in terms of an FPGA-based solution.

In this work, we aim to fill the existing gap by presenting a real-time feasible FPGA-based implementation of the BBF regulator targeting the CW ELBE accelerator. We exploit the analogy between the state-space form of a digital system and a finite-state machine (FSM) to propose a general architecture of the digital solution. This architecture is then

elaborated by introducing systolic arrays in order to deal with state-space matrix operations. Despite the fact that there are many sophisticated systolic array architectures [19–22], in this work, a straightforward systolic structure suffices that is similar to a 2-D array. Furthermore, we examine the application of fixed-point data types to the regulator algorithm. The latency of the resulting implementation is then compared to the one based on floating-point data types. Finally, by assembling a hardware testbench that involves another FPGA, we verify the output of our implementation against simulation data from Simulink.

The remainder of this paper is organized as follows: Section 2 presents the BBF loop structure at ELBE and discusses the loop elements, including the bunch arrival time regulator, the LLRF controller and the BAM sensor. The discussion aims to build a proper context for the regulator implementation. Section 3 describes the hardware and software frameworks used in this work. Following this, Section 4 introduces the resulting firmware architecture and demarcates the new regulator logic from the given framework. By moving towards internal details, Section 5 focuses on the implementation of state-space formalism and introduces important topics, such as systolic arrays and fixed-point data types. Section 6 demonstrates the hardware setup used to verify the regulator implementation and discusses the verification results. Finally, Section 7 concludes the paper.

2. Beam-Based Feedback Loop Structure at ELBE

ELBE beam-based feedback extends the existing control scheme by introducing a regulation loop involving a BAM sensor, a BBF regulator and a LLRF system of the fourth accelerating cavity (C4). This results in a new interconnection of control elements that involves cascaded loops. Figure 3 elaborates the emerging beam-based feedback structure, while making the main accent on the beam-based feedback regulator.

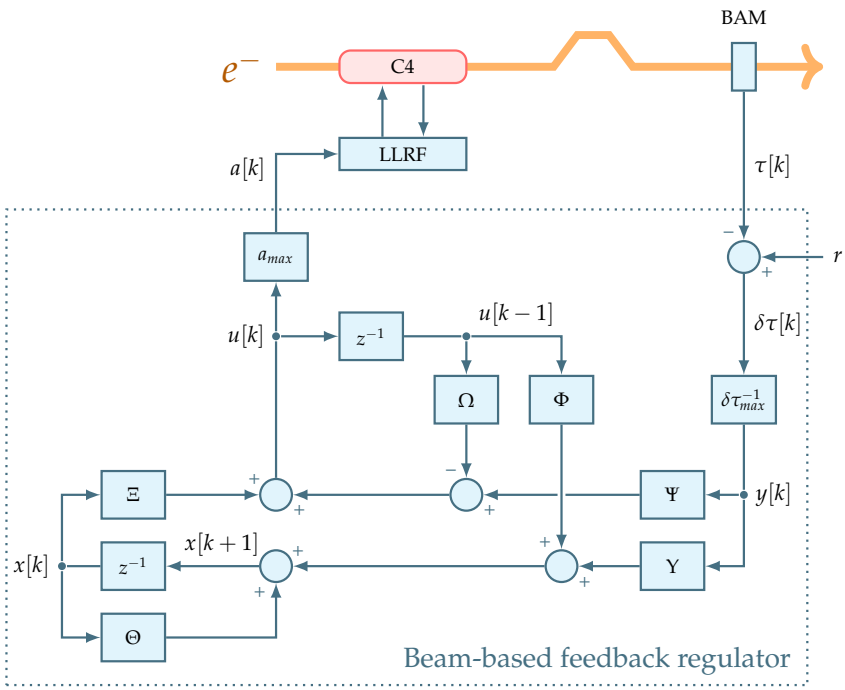

Figure 3. Beam-based feedback loop structure at ELBE.

2.1. Beam-Based Feedback Regulator

The BBF regulator designed in [4] represents a 7th-order single-input single-output $\mathcal{H}_2$ control law expressed in a state-space form

$$x[k+1] = Ax[k] + B_2u[k] + L_xe_x[k], \tag{1}$$
$$u[k] = K_ux[k] + L_ue_u[k], \tag{2}$$

where

$$e_x[k] = y[k] - C_2x[k] - D_{22}u[k], \tag{3}$$
$$e_u[k] = y[k] - C_2x[k] - D_{22}u[k-1], \tag{4}$$

where x, u and y denote the usual state, control input and measured output, and where A, B_2, C_2 and D_{22} are the system, input, output and feed-forward matrices, respectively. Matrices K_u, L_x and L_u are the products of $\mathcal{H}_2$ synthesis generated by MATLAB function h2syn. In order to alleviate the implementation of this control law, Equations (1) and (2) can be rearranged based on variables $x[k]$, $y[k]$ and $u[k-1]$. This yields a new set of matrices

$$\Theta = A + B_2K_u - B_2L_uC_2 - L_xC_2 - L_xD_{22}K_u + L_xD_{22}L_uC_2, \tag{5}$$
$$\Upsilon = B_2L_u + L_x - L_xD_{22}L_u, \tag{6}$$
$$\Phi = L_xD_{22}L_uD_{22} - B_2L_uD_{22}, \tag{7}$$
$$\Xi = K_u - L_uC_2, \tag{8}$$
$$\Psi = L_u, \tag{9}$$
$$\Omega = L_uD_{22}, \tag{10}$$

and since the new matrices can be evaluated offline, Equations (1) and (2) can be rewritten as

$$x[k+1] = \Theta x[k] + \Upsilon y[k] + \Phi u[k-1], \tag{11}$$
$$u[k] = \Xi x[k] + \Psi y[k] - \Omega u[k-1]. \tag{12}$$

As a result, Equations (11) and (12) form the structure of the beam-based feedback regulator displayed in Figure 3.

The regulator acts by correcting the setpoints of RF variables inside the LLRF controller FPGA. So to further reveal the loop details, the LLRF block displayed in Figure 3 needs to be expanded and elaborated.

2.2. RF System as Actuator for Electron Beam Regulation

In case of ELBE, every RF system is controlled by its dedicated LLRF controller. The purpose of such control is the stabilization of the corresponding RF variables, i.e., the amplitude A and phase ϕ of an accelerating RF field. Due to implementation specifics, the LLRF controller operates with the in-phase I and quadrature Q representations of the field amplitude and phase. Stabilized by the LLRF controller these I and Q signals are then applied inside a vector modulator (VM) to modulate a reference RF signal coming from a master oscillator. But since the signals generated by the LLRF controller are in the range of milliwatts, hence the name low-level RF, a solid-state power amplifier (SSPA) is used to drive the modulated RF signal to a kilowatt range. This finally results in a high-power RF signal that is passed through a waveguide to a RF cavity. Figure 4 illustrates the described RF system by expanding the LLRF block first introduced in Figure 3.

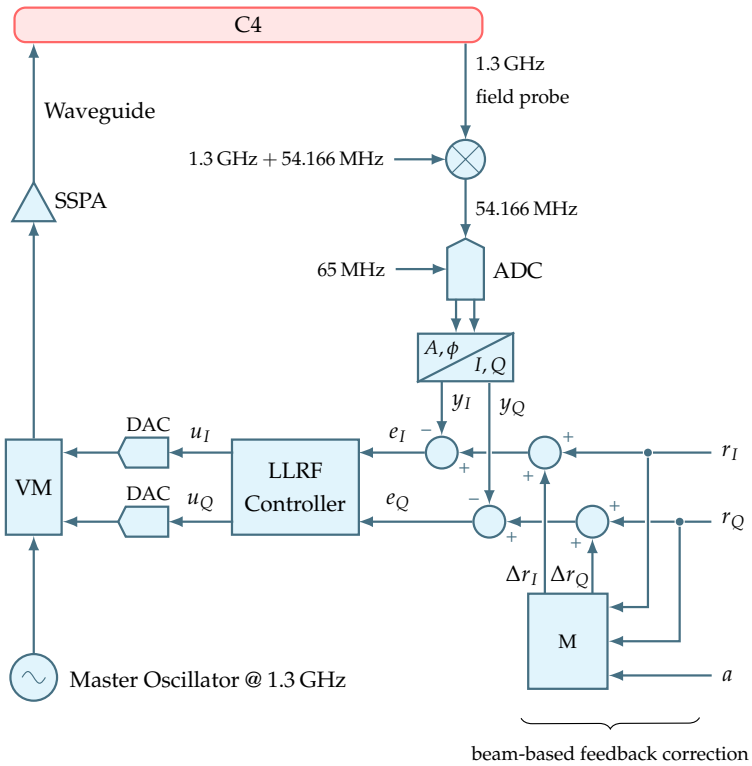

Figure 4. Schematic overview of RF system at ELBE including BBF extension.

To incorporate the RF setpoint correction signal a coming from the beam-based feedback regulator, the LLRF controller FPGA is extended by a setpoint modulation logic M. The logic is defined as

$$\begin{bmatrix} \Delta r_I \\ \Delta r_Q \end{bmatrix} = \frac{1}{100} \begin{bmatrix} r_I \\ r_Q \end{bmatrix} a, \tag{13}$$

where a denotes a change in the RF field amplitude expressed in percent units, and where r_I and r_Q are the RF field setpoints in I and Q, respectively. Factor $1/100$ is required to convert the amplitude change in percent to a relative error $\Delta A/A$ [8]. In fact, this factor could be applied by the BBF regulator implementation. In this case, however, the small resulting number would suffer from underflows caused by the fixed-point data type in use by the LLRF implementation. Therefore, this factor is applied last. To sum up, the I and Q setpoints are modulated by the relative amplitude error in order to alter the RF field oscillating inside the cavity. This will cause a change in the arrival time of subsequent electron bunches, which can then be diagnosed by the BAM sensor.

2.3. Bunch Arrival Time Monitor as Sensor of Electron Beam

The beam-based feedback is represented by a bunch arrival time measured by the BAM sensor, see Figure 3. The operation principle of this sensor is based on measuring bunch arrival time relative to an actively-stabilized optical timing reference. Specifically, periodic pulses of a reference laser are amplitude-modulated with electric signals coming from pick-up antennas that probe the electric field of the passing electron bunch. The arrival time information is thus transferred into an amplitude modulation of coincident laser pulses. According to such arrival time representation, the output of this sensor is

defined by a dimensionless modulation value τ with a working point set to $\tau = 1$. Figure 5 exemplifies a BAM readout taken at a bunch repetition rate of 50 kHz.

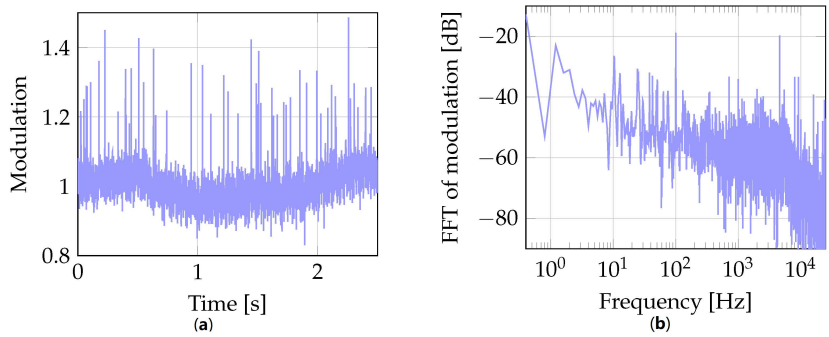

Figure 5. Example of BAM readout in (**a**) time and (**b**) frequency domains.

The BAM readout displays arrival time fluctuations caused by various disturbances, e.g., noise coming from the electron gun, drifts caused by changes in ambient temperature and RF noise inherent to RF acceleration process. In particular, the presented time domain data reveals distinct low frequency oscillations about the working point. Simultaneously, the frequency domain data features two components inherent to RF noise. These are (1) a random component represented by a spectral profile that decays with certain slopes as the frequency offset increases and (2) a deterministic component that manifests itself as a number of spurs along that profile. A harmonic of voltage ripple at 100 Hz is a representative of the latter.

The beam-based feedback regulator seeks to compensate the fluctuations in signal τ, and the simulation of such compensation is displayed in Figure 6.

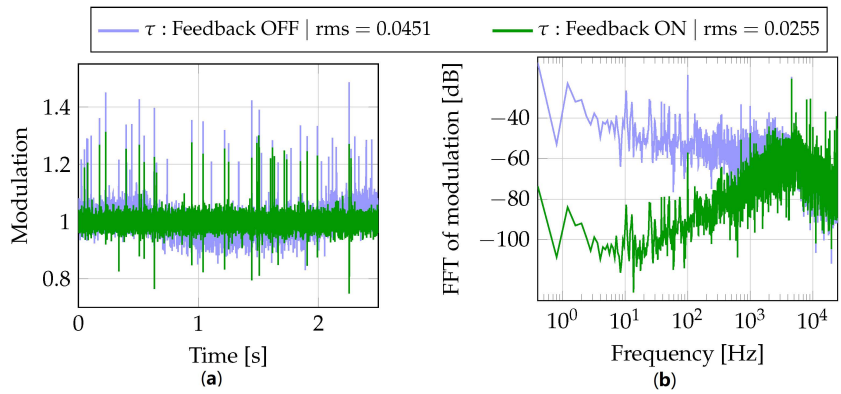

Figure 6. Simulation of BBF regulator with BAM readout in (**a**) time and (**b**) frequency domains.

The compensated data demonstrates the work of the regulator, i.e., (1) time domain data exhibits no drift and (2) the frequency data demonstrates suppression of low frequency noise up to ca. 5 kHz. Compared to the initial τ signal with no feedback, the regulator almost halves the disturbance effect in terms of the corresponding rms values.

The 50 kHz bunch repetition rate is commonly used for the ELBE THz beamline. Still, higher rates are possible, e.g., several hundred kilohertz or even a megahertz. Hence, the main reason to aim for a low-latency implementation of the regulator algorithm.

3. Hardware/Software Environment for Beam-Based Feedback Regulator

As a system, the beam-based feedback regulator relies on a number of subsystems to perform common tasks, such as establishing a user interface, sending and receiving of data, saving these data for further analysis, etc. To alleviate the heavy lifting, the regulator solution takes advantage of a digital platform based on the micro telecommunications computing architecture (MTCA) [23] and deployed on the ELBE accelerator machine [24].

3.1. MTCA.4 Hardware Environment

The fact that the regulator will be incorporated into the existing digital platform sets a few important conditions: (1) use of custom FPGA boards and (2) compliance with the existing firmware framework developed in VHDL [25]. Consequently, the regulator implementation is carried out on a specific data processing and telecommunication board, called the advanced mezzanine card (AMC) TCK7 [26]. The board features a high-performance FPGA device XC7K420T from Xilinx. To help leveraging the features of this board the given firmware framework provides support for

- RAM- or register-based internal interface (II) to communicate with CPU software;
- Low-latency links (LLLs) to communicate with other FPGA boards;
- Data acquisition (DAQ) facility to save diagnostic data to DDR3 memory.

In this work, the AMC TCK7 board must (1) receive data from the BAM FPGA, (2) do the processing and (3) send the result to the LLRF FPGA. While the processing is done inside the XC7K420T chip, the receiving/sending occurs through the low-latency links that are driven by 10-Gigabit small form-factor pluggable (SFP) optical transceivers. Measurement signals τ and control signals a are transferred via these LLL facilities. Similarly, the initialization of the processing stage happens through a register-based hardware/software (HW/SW) interface driven by a PCI Express (PCIe) connection. This interface is used by external CPU software to set the values of gain matrix elements, setpoints, etc. In addition, the processing stage needs to save diagnostics data. For this reason, DAQ facility is used to dump data to DDR3 memory. To sum up this description, Figure 7 illustrates a general block diagram showing the beam-based feedback regulator in the context of the given MTCA.4 hardware environment.

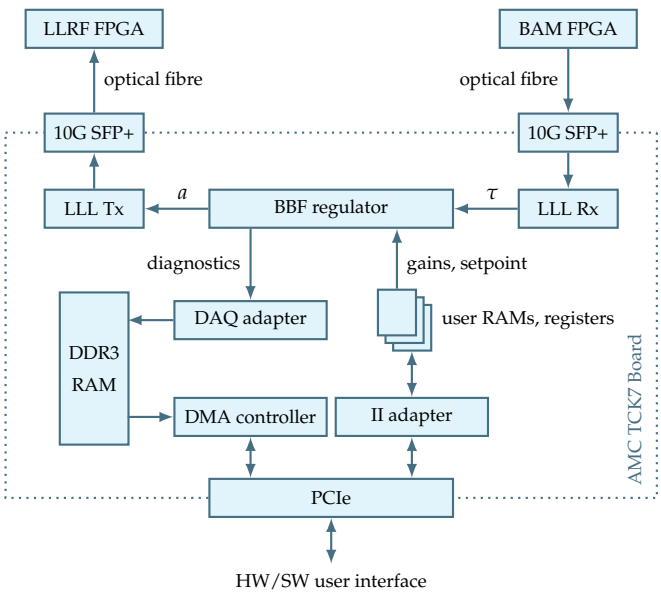

Figure 7. Beam-based feedback regulator in the context of MTCA.4 hardware environment.

The complexity of the presented hardware system underscores the importance of a software-based user interaction. Hence, the necessity to establish a hardware/software interface that would facilitate the initialization, control and other user related tasks.

3.2. Hardware/Software Interface

The MTCA.4 technology uses a special software framework [27] to support the PCIe-based communication between the related hardware and software. Specifically, this framework provides the necessary application programming interface (API) to establish a register-based HW/SW interface. By writing and reading these registers the user is able to interact with the beam-based feedback regulator FPGA, and Figure 8 depicts a basic user interaction as a unified modeling language (UML) use case diagram.

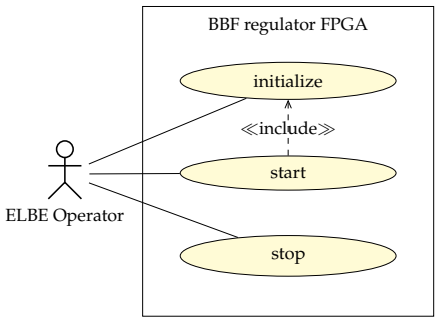

Figure 8. UML use case diagram summarizing user interaction with the BBF regulator FPGA.

Along with the basic use case to initialize the gain data when the application starts, a more sophisticated variant is to allow updating these data when the regulation is already running. The difficulty is related to the fact that ELBE is operated in CW mode, so there are no pauses long enough to permit a plain data overwrite. Moreover, it is reasonable to assume that updating the gain data separately, i.e., regardless of the algorithm state as a whole, will lead to erroneous algorithm results, hence the necessity to update the gains (1) all at once and (2) at a proper time instant. Essentially, the second requirement suggests an FSM-based implementation on the hardware side. In the meantime, the first requirement is fulfilled on the software side by first making a time-consuming write of the entire data from the software to intermediate hardware buffers and then triggering a fast data update on the hardware side. Figure 9 demonstrates this concept.

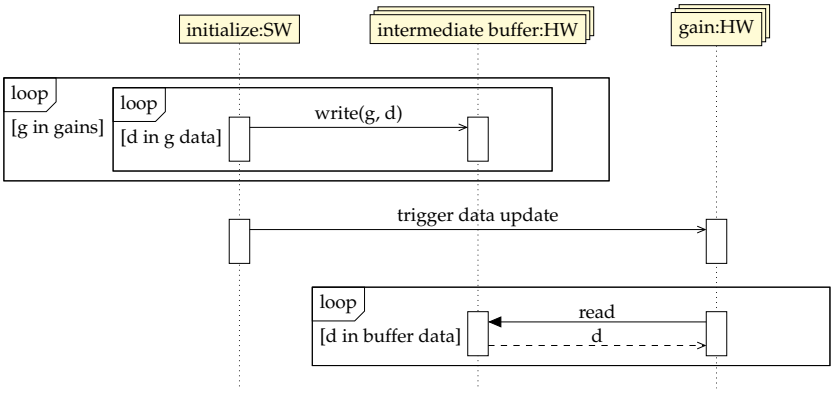

Figure 9. UML sequence diagram demonstrating the concept of (re)initialization of gain data.

The starting and stopping use cases are both based on the manipulation of the same flag to enable feedback data propagation to the regulation algorithm. This one-bit flag, called CTL_ENA, is set to 1 to enable regulation. Fundamentally, this defines an event-driven behavior of the algorithm implementation, i.e., when the algorithm receives no data, the regulation idles, see Figure 10.

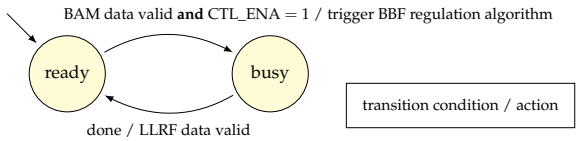

Figure 10. State diagram showing the effect of CTL_ENA flag on regulator state transitions.

In essence, the given MTCA.4 environment sets a number of requirements to the firmware architecture of the beam-based feedback regulator, namely:

- firmware is written in hardware description language VHDL;
- digital design targets an FPGA device from Xilinx;
- communication logic adheres to the given protocols, i.e., LLL and II;
- regulator algorithm is governed by an FSM.

With this in mind, the firmware architecture can now be elaborated.

4. Firmware Architecture of Beam-Based Feedback Regulator

The structure of the MTCA.4 firmware framework divides the on-chip logic into board and application compartments. The former manages the board specific features, including the low-level communication interfaces and clock generation, while the latter defines the application logic. Both compartments are then united inside a top level VHDL entity. Figure 11 depicts this structure as a general block diagram and uses color codes to demarcate the new regulator logic from the given framework.

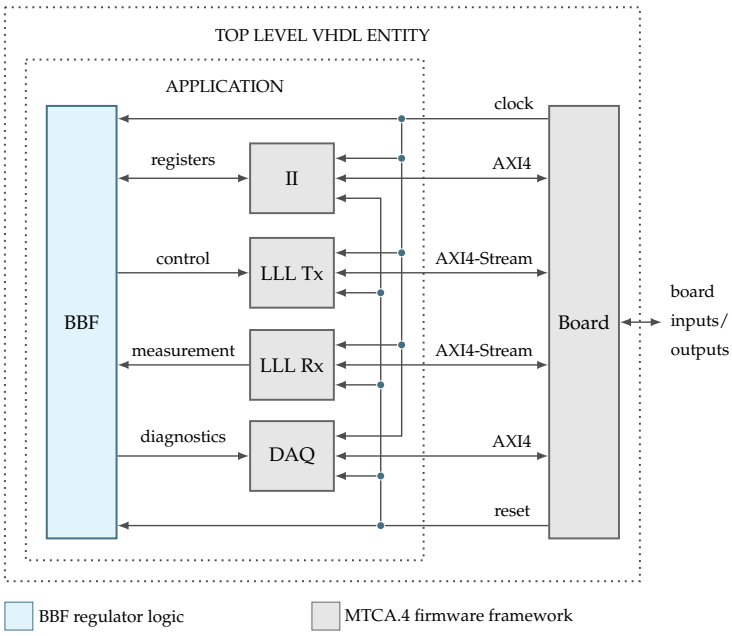

Figure 11. Structure of top level VHDL entity as defined by the MTCA.4 firmware framework.

4.1. Behavioral Model

The behavior of the regulator can be modeled in terms of the data that flows inside the application compartment and drives the initialization, regulation and diagnostics:

Initialization Before running the regulation algorithm, the gain data need to be initialized. Since these data are transferred from the CPU software, the values are received by the firmware through the II communication. In fact, a single gain can be represented by a matrix with multiple values, so the receiver should be RAM-based. According to the firmware requirements outlined in Section 3, this RAM is expected to serve as an intermediate buffer that is first written by the software and then, after a software trigger, read by the actual gain logic. Once such initialization is complete, the regulation data flow becomes enabled.

Regulation The regulation data flow starts from the reception of a BAM sensor measurement coming over a dedicated low-latency link. Provided the regulator algorithm is not busy at the moment and the regulation is enabled by the user, see Figure 10, the new measurement triggers the computation of a new control signal. Otherwise, the received measurement is dropped. Such behavior ensures that the algorithm always sees up-to-date measurements. When the algorithm is indeed triggered, the data starts flowing to gains and further to sums. Once the regulation algorithm is complete, the new control signal is transmitted over a dedicated low-latency link to the LLRF actuator.

Diagnostics The diagnostics saves the regulation data, including the BAM sensor measurements and the corresponding control signals. Importantly, the BAM data are saved even if the regulator is disabled. This allows to diagnose the open-loop behavior of the system.

To sum up, Figure 12 illustrates a functional schematic of the BBF application. Note that the illustrated firmware blocks belong to the new regulator logic, hence the corresponding color code. In this context, the additional Rx and Tx blocks act as adapters between the framework and the regulator in order to establish a properly registered ready/valid handshake—a flow control technique [28] that is used throughout the entire regulator logic. Note also that for the sake of brevity the diagram omits the transformation from signal $\tau[k]$ to $y[k]$ and from $u[k]$ to $a[k]$. Finally, the diagram makes the central role of the FSM obvious.

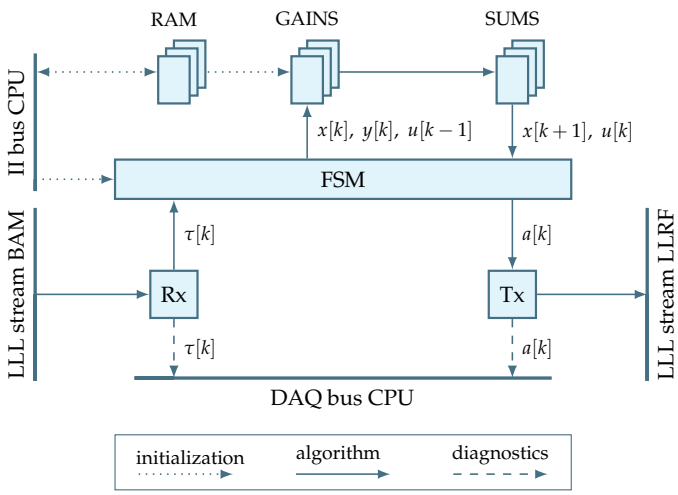

Figure 12. Functional schematic illustrating the main data flows inside the BBF application.

4.2. Finite State Machine

In addition to the firmware requirements outlined in Section 3, another reason for involving an FSM to manage the regulator algorithm is inspired by the analogy between a discrete-time state-space form of the regulator and a Mealy state machine [29]. Specifically, a hardware implementation of the Mealy machine is composed of combinational and sequential logic blocks. The combinational logic takes the current state together with input and computes the next state and output. The next state is then saved, or registered, by the sequential logic. The process repeats during the next iteration. Accordingly, Figure 13 depicts an FSM of the state-space regulator, where sequential logic block z^{-1} registers the regulator state, and where combinational logic blocks $f(\cdot)$ and $g(\cdot)$ implement Expressions (11) and (12), respectively.

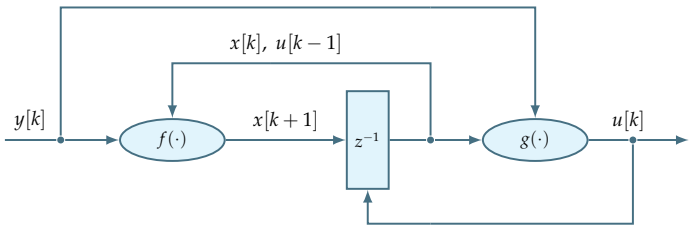

Figure 13. Discrete-time state-space regulator visualized as a Mealy FSM.

Unfolding this FSM approach, Figure 14 demonstrates a state diagram that captures the essential parts of the regulator behavior. Note that once the BBF algorithm is triggered, $f(\cdot)$ and $g(\cdot)$ will be executed in parallel. Yet $f(\cdot)$ will take significant time to process its longest operation, i.e., Θx. So it is possible to get the result of $g(\cdot)$ and initiate the sending of LLRF data before $f(\cdot)$ completes. Hence, a busy state with two stages. Finally, the latency of algorithm operations, such as Θx, underscores the necessity to analyze the implementation of these state-space constructs.

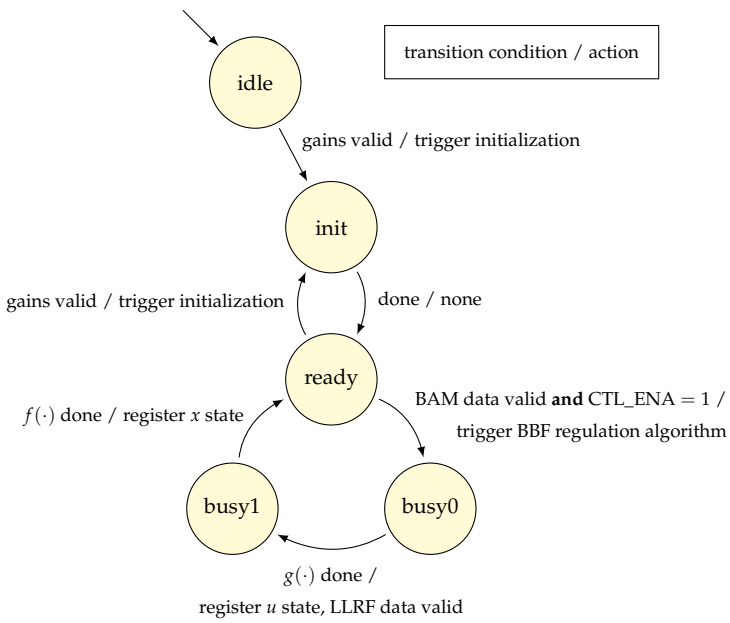

Figure 14. State diagram showing the operation of the regulator FSM.

5. State-Space Implementation in Hardware

In this work, we propose to describe the state-space formalism of the beam-based feedback regulator in terms of systolic arrays. Indeed, Equations (11) and (12) are based on matrix-vector multiplication, and systolic arrays offer a hardware architecture that enables massively parallel execution of this mathematical operation. Moreover, when implemented on FPGAs, systolic arrays can enjoy not only the inherently parallel nature of FPGAs, but also the availability of specialized circuits that are able to efficiently perform mathematical operations.

5.1. Systolic Array Structure

Systolic arrays are grid-like interconnections of data processing elements, or nodes, that are driven by data to perform some specific uniform operation. In particular, a properly organized data flow can drive an array of multiply-accumulate nodes, or MACs, in order to implement a matrix-vector multiplication. Figure 15 demonstrates an example of a node interconnection that computes the product $c = A\,b$, where b and c are 2×1 input and output vectors, respectively, and where A is a 2×2 matrix. In this straightforward systolic implementation the number of nodes corresponds to the size of the output vector c. This allows to parallelize the computation of individual output vector elements and to keep the computation results local to the nodes. Consequently, when the data finishes propagating through this interconnection in a wave-like manner, the nodes will store a fully computed output vector.

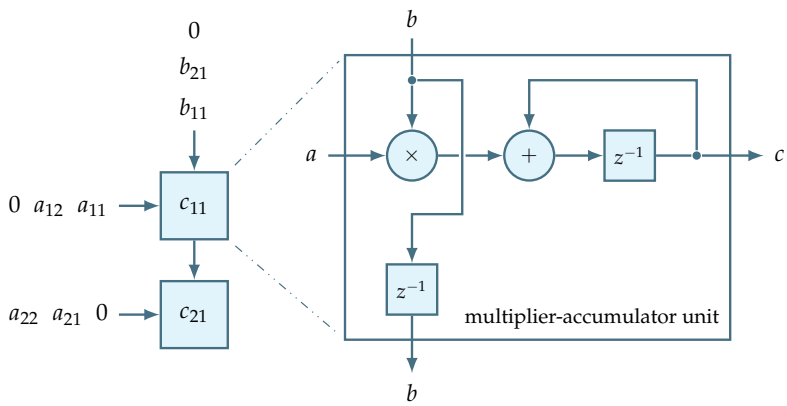

Figure 15. Structure of systolic array for multiplying a 2×1 vector b by a 2×2 matrix A.

An efficient implementation of the presented systolic array node, i.e., the multiplier-accumulator unit, requires a design that exploits specialized computational resources provided by an FPGA, namely digital signal processor (DSP) slices. These high-speed circuits support a number of mathematical functions, including multiplication and addition, and therefore can accelerate a compute-intensive design. According to the data sheet [30], the XC7K420T device features 1680 DSP slices, and each slice contains a pre-adder, a 25×18 multiplier, an adder, and an accumulator. Correspondingly, this kind of slice can be configured to perform a multiply-accumulate operation in the form of $a \cdot b + c$, where a and b are 25-bit and 18-bit signals, respectively, and where accumulation with c is sign-extended to 48 bits. On the one hand, by adhering to these signal widths, e.g., in case of custom fixed-point data types, a MAC unit can be mapped to a single DSP slice on the FPGA, thus leading to an optimal use of FPGA resources. On the other hand, if the MAC unit needs to operate with wider signals, e.g., when dealing with 32-bit floating-point data, the number of DSP slices per MAC unit increases, and the design consumes more FPGA resources. To investigate the optimal solution—both in terms of resources and latency—this work focuses on the custom fixed-point data types.

5.2. Fixed-Point Analysis of Regulator Signals and Gains

Due to the 25 × 18 signal widths dictated by the DSP48E1 slice [31], the fixed-point implementation differentiates between two types of data:

- signals flowing through the regulator, e.g., from $y[k]$ to $u[k]$;
- gain matrix values that modify the signals.

The signals and gains are assigned to 25-bit and 18-bit words, respectively, thus prioritizing the precision of the signal data. Apart from the precision, the 25-bit signal word needs to allocate enough bits for the integer part to avoid overflows inside the regulator. To mitigate this risk and to improve the conditioning of the regulator, the inputs and outputs are properly scaled. It is expected that the input signal coming from the BAM sensor exhibits a deviation of roughly $\delta\tau_{max} = 0.1$. This yields $y = \delta\tau \cdot \delta\tau_{max}^{-1} = 0.1 \cdot 10 = 1$, thus normalizing the signal magnitudes flowing inside the regulator.

However, there can also be unexpected spikes in the BAM readout, see Figure 5. In general, a large deviation of the input signal $\delta\tau$ will result in a considerable action taken by the regulator. In case of ELBE, a drastic change of the signal driving the cavity will have a high probability to trigger the ELBE protection system to switch off the accelerator. To cope with this unwanted scenario the signal $\delta\tau$ is limited as follows

$$\delta\tau = \begin{cases} \delta\tau, & \text{if } \delta\tau < \delta\tau_{lim} \\ \delta\tau_{lim}, & \text{otherwise} \end{cases}. \tag{14}$$

Setting $\delta\tau_{lim} = 1$ yields $y = \delta\tau_{lim} \cdot \delta\tau_{max}^{-1} = 1 \cdot 10 = 10$. Under these conditions, four bits are enough to represent the integer part of the signal. The derived signal data type is then (1, 25, 20), where the fixed-point notation is specified as

$$(\text{sign, word length, word fraction length}). \tag{15}$$

In contrast, the fixed-point data type for gains of a 4th-order regulator is derived by examining the magnitudes of the values stored inside the corresponding matrices, namely

$$\Theta = \begin{bmatrix} 47.0522 & -39.4131 & 1.48102 & -0.45106 \\ 0.26835 & 99.3678 & 0.02415 & -0.00735 \\ 13.2079 & 11.7310 & 99.0439 & 0.13750 \\ -72.9060 & -102.943 & -7.72665 & 87.6644 \end{bmatrix} \times 10^{-2},$$

$$\Xi = \begin{bmatrix} -291.624 & -411.771 & -30.9066 & 9.41304 \end{bmatrix} \times 10^{-2},$$

$$\Upsilon = \begin{bmatrix} -7.13823 \\ -0.11638 \\ -47.8240 \\ 12.2410 \end{bmatrix} \times 10^{-2}, \qquad \Phi = \begin{bmatrix} -2.34632 \\ -0.03825 \\ 0.71523 \\ 12.2410 \end{bmatrix} \times 10^{-2},$$

$$\Psi = 48.9641 \times 10^{-2}, \qquad \Omega = -48.9641 \times 10^{-2}.$$

Depending on the magnitude range of a particular matrix, the gain data type can vary its precision. For example, the maximum magnitude among the matrix values constituting the gain Θ is -1.0294. Hence, only one bit suffices for the integer part, another bit represents the sign, and 16 bits can be allocated to the fraction part, thus yielding a precision of $2^{-16} = 1.5259 \times 10^{-5}$. Following this, Table 1 displays the various fixed-point data types assigned to the regulator matrices.

Table 1. Gain matrices with value magnitude ranges and assigned fixed-point data types.

Gain	Minimum Magnitude	Maximum Magnitude	Fixed-Point Data Type
Θ	-7.3538×10^{-5}	-1.0294	(1, 18, 16)
Ξ	0.0941	-4.1177	(1, 18, 14)
Υ	-0.0012	-0.4782	(1, 18, 16)
Φ	-3.8253×10^{-4}	0.1224	(1, 18, 16)
Ψ	0.4896	0.4896	(1, 18, 16)
Ω	-0.4896	-0.4896	(1, 18, 16)

The gains $\delta\tau_{max}^{-1}$ and a_{max} are integers with values 10 and 1, respectively, so their fraction parts could be omitted. Still, it is expected that these gains can be manipulated during run-time to do fine-tuning of the regulator. Thus, the fraction parts are preserved and the corresponding data types are both chosen as (1, 18, 10). In addition, the BAM and LLRF signals have fixed-point data types (0, 18, 15) and (1, 18, 10), respectively. Consequently, the regulator implementation needs to take this into account when receiving or sending low-latency link data.

The presented analysis underscores the fact that a fixed-point implementation requires a thorough examination of the data flowing inside the design. It is therefore of interest to see how much this effort helps to keep the systolic array structure optimal in terms of latency and resources, e.g., compared to a floating-point implementation.

5.3. Data Flow to Drive Systolic Arrays

The operation of systolic arrays relies on a properly organized data flow. In this work, a digital circuit responsible for the data flow is called a data channel, and multiple data channels compose a data stream. As shown in Figure 16, this circuit plays a central role in the gain entity.

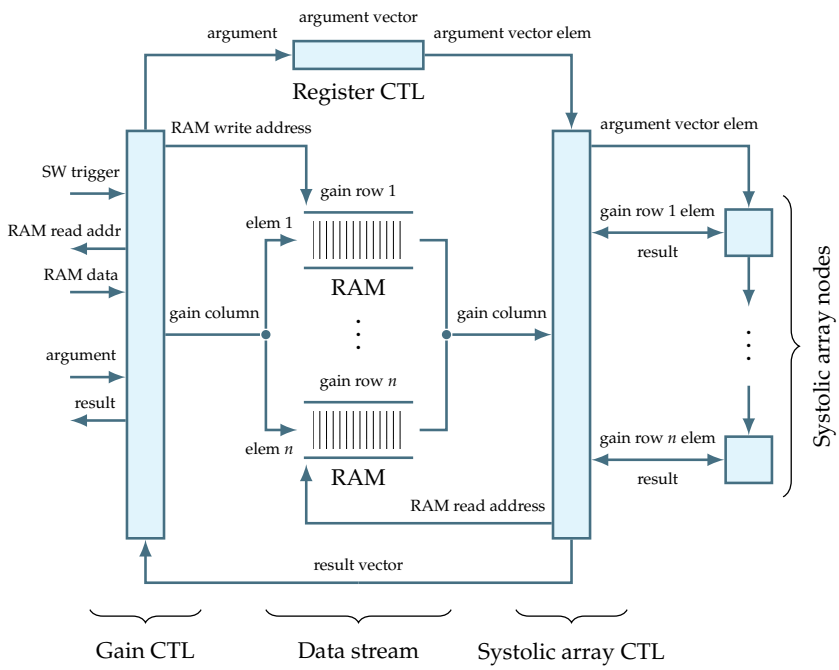

Figure 16. Gain entity schematic showing internal data flow.

Inside the data stream circuit, the data are structured based on their types. The gain is treated as a two-dimensional matrix and is organized into matrix rows. These rows are represented by separate data channels implemented as RAMs. Such organization facilitates the gain data throughput, because it allows to write or read an entire matrix column in a single clock cycle. This also places a requirement on the software to write the gain data to intermediate RAM buffers in a column-major order. After a software trigger, the gain controller will rely on the proper format of the intermediate data in order to initialize the internal data channels column by column. Unlike the gain, the signal is placed into a register-based memory. Again, this allows to register an incoming signal, i.e., the gain argument, in a single clock cycle. Along with the gain column, the signal vector element is then fed into the systolic array to perform the necessary computation. Once the computation is over, the results from each systolic array node are assembled into a result vector which is then propagated to the gain entity output.

Undoubtedly, the data stream circuit introduces some amount of overhead into the design. Moreover, the latency of the data management will dominate in case of low-order regulator implementations, see Figure 17.

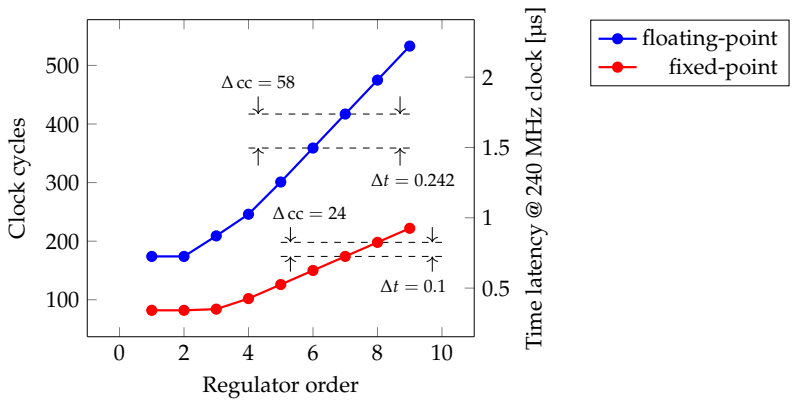

Figure 17. Time latency of the regulator busy state under various orders and data types.

The data stream overhead is partially related to data padding required by systolic arrays. As can be seen in Figure 15, the data flow driving the systolic array is padded with zeros. Although these zeros ensure the correct computation inside the nodes, they also lead to the increase of the corresponding data channel size which becomes

$$\text{data channel size} = \text{gain row size} + \text{gain column size} - 1. \tag{16}$$

Of course, the overall latency of the regulation algorithm is also affected by the implementation of the state-space computation units, i.e., the MAC and the sum. This is especially true for the floating-point case which uses a 32-bit single precision data type [32] and thus relies on an intellectual property (IP) from Xilinx [33]. In this context, even though the sum implementation represents a trivial element-wise summation of the argument vectors, and thus does not involve systolic arrays, its floating-point implementation still uses DSP resources, see Table 2.

Table 2. Use of DSP resources by the two main computation units of the state-space algorithm.

Unit	Implementation	DSPs	Clock Cycles	Total DSPs for 7th Order
MAC	fixed-point	1	5	26
	floating-point	4	22	104
Sum	fixed-point	none	3	none
	floating-point	2	14	18

Indeed, by adhering to the dictated signal widths the fixed-point MAC implementation is mapped to a single DSP slice. Compared to the floating-point counterpart that uses more DSPs per MAC, the one-to-one mapping allows the fixed-point design to occupy considerably less DSP resources on the FPGA.

It can be argued, though, that the usage of the proposed gain entity architecture for scalar operations, such as $\delta\tau_{max}^{-1} \cdot \delta\tau$, is far beyond what is required. Hence, the unwanted overhead. This is a reasonable point provided the system does not change in the future. Yet there are plans to extend the system in order to regulate the compression and energy of the electron bunches. In this case, the current architecture can be easily scaled to implement the required mathematical operation, e.g.,

$$\begin{bmatrix} y_\tau \\ y_E \\ y_C \end{bmatrix} = \begin{bmatrix} \delta\tau_{max}^{-1} & 0 & 0 \\ 0 & \delta E_{max}^{-1} & 0 \\ 0 & 0 & \delta C_{max}^{-1} \end{bmatrix} \cdot \begin{bmatrix} \delta\tau \\ \delta E \\ \delta C \end{bmatrix}, \tag{17}$$

where E and C denote the energy and compression of the electron bunches, respectively. This underscores the scalability of the current digital solution.

In general, the presented data demonstrates that the proposed state-space architecture can be routinely clocked at 240 MHz—a particular clock signal generated by the board compartment of the MTCA.4 firmware framework. Running at such frequency allows the fixed-point implementation to stay on the sub-microsecond level even in the case of high-order regulator designs. The floating-point implementation exhibits greater latency, but even the 7th-order regulator designed in [4] takes less than 2 microseconds to perform its state-space computation. The 50 kHz bunch repetition rate is thus supported by both implementations. In the mean time, the fast fixed-point implementation needs to be verified in hardware.

6. Firmware Verification

The correctness of the regulator implementation is verified by assembling a digital setup which involves the BBF regulator FPGA connected to an additional FPGA that serves as a testbench. Along with the verification of the state-space implementation, the usage of a separate FPGA allows testing the low-latency link communication. The corresponding installation can be observed in Figure 18. The two FPGAs are slided into a MTCA.4 crate leaving only their front panels exposed. As can be seen, these panels feature SFP slots that are used to interconnect the two devices using optical cables.

In principle, the testbench operation can be outlined as follows

1. Sending a stimulus to the BBF regulator FPGA;
2. Receiving a response;
3. Comparing the received response with a similar one generated by a floating-point MATLAB simulation.

The MATLAB simulation is run offline and is driven by the same stimulus—simulated BAM data. Hence, both responses should be identical to a certain degree of precision. Figure 19 summarizes the outlined testbench operation.

Figure 18. MTCA.4 crate with two installed FPGAs serving as a testbench.

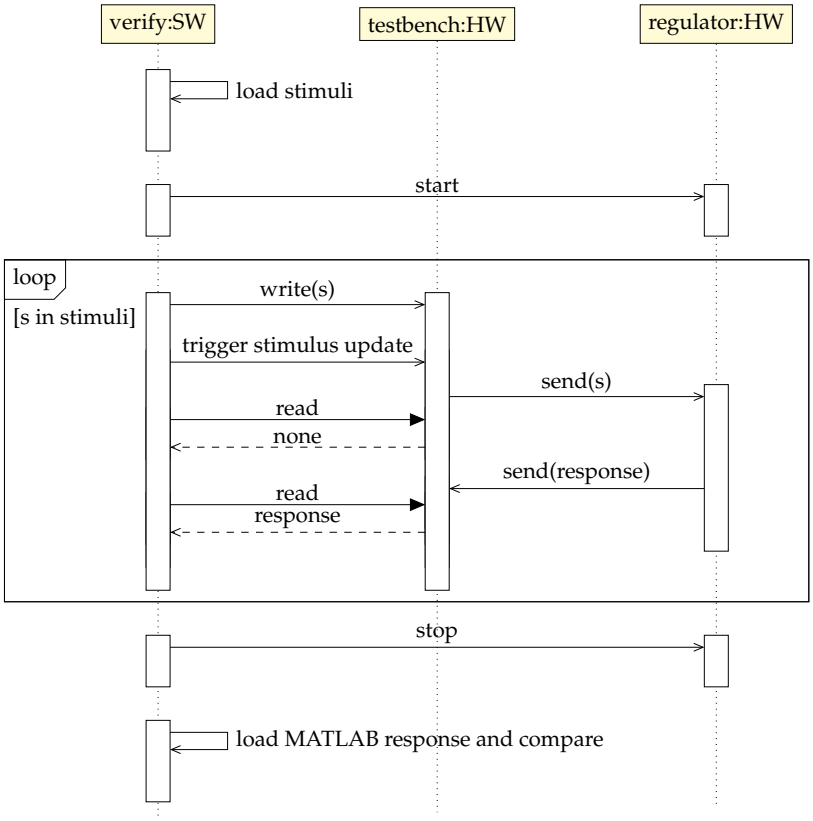

Figure 19. UML sequence diagram showing the operation of the BBF regulator testbench.

In this work, the testbench compares the time response of a 4th-order regulator implemented in fixed-point with the same regulator simulated in a floating-point MATLAB model. The result of this comparison is depicted in Figure 20.

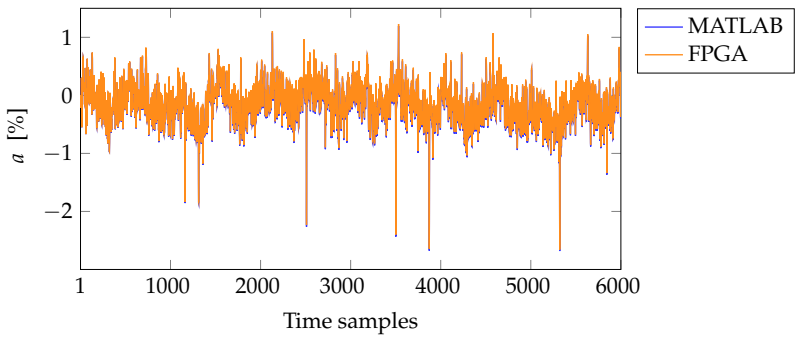

Figure 20. Comparison of MATLAB and testbench time responses for a 4th-order regulator.

The difference between the response simulated in MATLAB and the one produced by the testbench is displayed in Figure 21. Essentially, the assembled testbench represents an open-loop system, i.e., the output of the testbench regulator has no effect on the next BAM data sample. Coupled with the precision issue, the open-loop scenario leads to accumulation of the mismatch between the two responses. Still, it is expected that this negative behavior will disappear, once the fixed-point regulator closes the real machine loop. In the closed-loop scenario, the correctness of the first few responses will matter, and the current testbench data exhibits up to 20 correct responses before the least significant fraction bit flips. Note that the magnitude of the bit flip corresponds to the precision of the fixed-point data type (1, 18, 10) used by the LLRF controller.

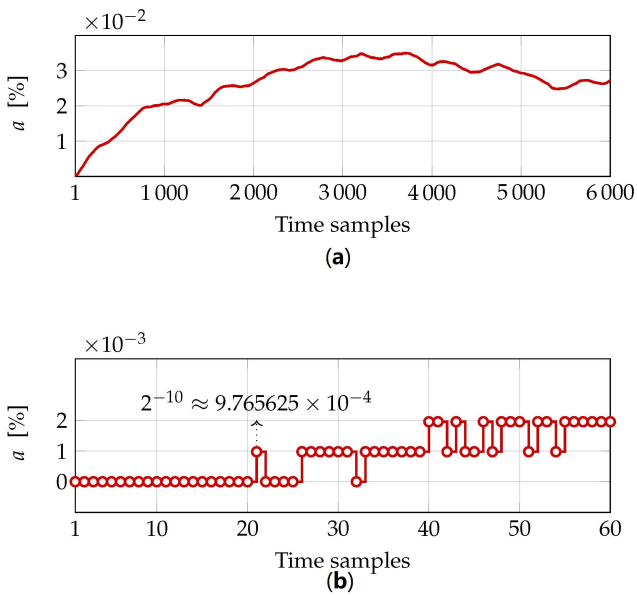

Figure 21. FPGA and MATLAB responses expressed as (**a**) absolute difference and (**b**) zoomed.

7. Conclusions

In the context of the linear accelerator ELBE, the benefit of implementing a beam-based feedback regulator using an FPGA is twofold. Firstly, the low-latency nature of FPGAs allows dealing with fast processes, such as the regulation of an electron bunch arrival time. Secondly, the high configurability of FPGAs enables the implementation of sophisticated regulation algorithms, e.g., an optimal $\mathcal{H}_2$ regulator in its state-space representation.

Accordingly, in this work we proposed an FPGA-based implementation of a beam-based feedback regulation algorithm to compensate electron bunch arrival time fluctuations. Using a top-down approach, we gradually introduced the levels of the regulator system, starting from the structure of the ELBE beam-based feedback loop and culminating in the digital architecture of a state-space regulator. In order to implement the matrix-vector multiplications of the state-space formalism, we used systolic arrays. Even though the systolic arrays added data management overhead into the design, we saw that the design could easily be scaled in terms of the regulator orders as well as its inputs and outputs. Furthermore, we made a thorough analysis of a potential fixed-point implementation and then compared it to a floating-point one. Essentially, when clocked at 240 MHz the fixed-point implementation of a 4th-order $\mathcal{H}_2$ regulator takes 0.425 µs to perform its state-space computations, thus enabling sub-microsecond sample times. In contrast, a similar floating-point implementation takes 1.025 µs. Finally, we verified the correctness of the implementation by running a hardware testbench which included two interconnected FPGAs.

The next step is to validate the proposed digital solution on the real machine. This will allow evaluating the whole spectrum of decisions made in this and our previous works, including the disturbance modeling, the choice of the regulation algorithm and the state-space implementation. Such evaluation will be the subject of our future report.

Author Contributions: Conceptualization, A.M., M.K. and E.P.; methodology, A.M.; software, A.M.; validation, A.M.; formal analysis, A.M.; investigation, A.M. and M.K.; resources, M.K.; data curation, A.M.; writing—original draft preparation, A.M.; writing—review and editing, M.K. and E.P.; visualization, A.M.; supervision, M.K. and E.P.; project administration, M.K.; funding acquisition, M.K. and E.P. All authors have read and agreed to the published version of the manuscript.

Funding: This work was partially funded by the Estonian Research Council grant PRG658.

Institutional Review Board Statement: Not applicable.

Informed Consent Statement: Not applicable.

Data Availability Statement: Not applicable.

Acknowledgments: The authors would like to thank the MicroTCA Technology Lab at the German Electron Synchrotron (DESY) for their help with the MTCA.4 firmware framework. Special thanks goes to Cagil Gümüş, Burak Dursun and Łukasz Butkowski.

Conflicts of Interest: The authors declare no conflict of interest.

Abbreviations

AMC	Advanced mezzanine card
API	Application programming interface
BAM	Bunch arrival time monitor
BBF	Beam-based feedback
CPU	Central processing unit
CW	Continuous wave
DAQ	Data acquisition
DDR	Double data rate
DSP	Digital signal processor
ELBE	Electron linear accelerator for beams with high brilliance and low emittance
FPGA	Field-programmable gate array

FSM	Finite state machine
HZDR	Helmholtz-Zentrum Dresden-Rossendorf
HW	Hardware
II	Internal interface
IP	Intellectual property
LLL	Low-latency link
LLRF	Low-level radio frequency
MAC	Multiply-accumulate
MTCA	Micro telecommunications computing architecture
PCIe	Peripheral component interconnect express
RAM	Random-access memory
RF	Radio frequency
SFP	Small form-factor pluggable
SSPA	Solid-state power amplifier
SW	Software
UML	Unified modeling language
VHDL	VHSIC hardware description language
VHSIC	Very high-speed integrated circuit
VM	Vector modulator

Nomenclature

ELBE accelerator	
A	RF field amplitude
a	RF field amplitude change in percents
ϕ	RF field phase
e^-	electron
τ	electron bunch arrival time in dimensionless BAM modulation units
I	in-phase representation of RF field amplitude and phase
Q	quadrature representation of RF field amplitude and phase
Control configuration	
A	system matrix
B_2	input matrix
C_2	output matrix
D_{22}	feed-forward matrix
r	reference input (setpoint)
e	error signal
u	control signal (manipulated plant input)
x	control state
y	plant output
z^{-1}	discrete integrator
K_u	state feedback gain
L_u	observer gain
L_x	observer gain
Θ	gain from $x[k]$ to $x[k+1]$
Υ	gain from $y[k]$ to $x[k+1]$
Φ	gain from $u[k-1]$ to $x[k+1]$
Ξ	gain from $x[k]$ to $u[k]$
Ψ	gain from $y[k]$ to $u[k]$
Ω	gain from $u[k-1]$ to $u[k]$

References

1. Schlarb, H. Techniques for Pump-Probe Synchronisation of Fsec Radiation Pulses. In Proceedings of the Particle Accelerator Conference, Knoxville, TN, USA, 16–20 May 2005.
2. Pfeiffer, S.; Branlard, J.; Hoffmann, M.; Schmidt, C. Advanced LLRF System Setup Tool for RF Field Regulation of SRF Cavities. In Proceedings of the 19th International Conference on RF Superconductivity, Dresden, Germany, 30 June–5 July 2019. [CrossRef]

3. Zenker, K.; Gümüş, C.; Hierholzer, M.; Michel, P.; Pfeiffer, S.; Schlarb, H.; Schmidt, C.; Schurig, R.; Steinbrück, R.; Kuntzsch, M. MicroTCA.4-Based Low-Level RF for Continuous Wave Mode Operation at the ELBE Accelerator. *IEEE Trans. Nucl. Sci.* **2021**, *68*, 2326–2333. [CrossRef]
4. Maalberg, A.; Kuntzsch, M.; Petlenkov, E. Regulation of the Linear Accelerator ELBE Exploiting Continuous Wave Mode of a Superconducting RF Cavity. In Proceedings of the American Control Conference, Atlanta, GA, USA, 8–10 June 2022.
5. Kwakernaak, H. $\mathcal{H}_2$-optimization—Theory and applications to robust control design. *Annu. Rev. Control* **2002**, *26*, 45–56. [CrossRef]
6. Skogestad, S.; Postlethwaite, I. *Multivariable Feedback Control: Analysis and Design*, 2nd ed.; John Wiley & Sons, Ltd.: Chichester, UK, 2005; pp. 355–356.
7. Pfeiffer, S.; Schmidt, C.; Bock, M.K.; Schlarb, H.; Jalmuzna, W.; Lichtenberg, G.; Werner, H. Fast Feedback Strategies for Longitudinal Beam Stabilization. In Proceedings of the 2012 International Particle Accelerator Conference, New Orleans, LA, USA, 20–25 May 2012.
8. Koprek, W.; Behrens, C.; Bock, M.K.; Felber, M.; Gessler, P.; Schlarb, H.; Schmidt, C.; Schulz, S.; Steffen, B.; Wesch S.; et al. Intra-train Longitudinal Feedback for Beam Stabilization at FLASH. In Proceedings of the 32nd International Free Electron Laser Conference, Malmö, Sweden, 23–27 August 2010.
9. Rezaeizadeh, A.; Schilcher, T.; Smith, R. MPC based Supervisory Control Design for a Free Electron Laser. In Proceedings of the 54th Conference on Decision and Control, Osaka, Japan, 15–18 December 2015.
10. Rezaeizadeh, A.; Schilcher, T.; Smith, R. Adaptive robust control of longitudinal and transverse electron beam profiles. *Phys. Rev. Accel. Beams* **2016**, *19*, 052802. [CrossRef]
11. Bellandi, A.; Butkowski, Ł.; Dursun, B.; Eichler, A.; Gümüş, C.; Kuntzsch, M.; Nawaz, A.; Pfeiffer, S.; Schlarb, H.; Schmidt, C.; et al. Online Detuning Computation and Quench Detection for Superconducting Resonators. *IEEE Trans. Nucl. Sci.* **2021**, *68*, 385–393. [CrossRef]
12. Löhl, F. Optical Synchronization of a Free-Electron Laser with Femtosecond Precision. Ph.D. Thesis, University of Hamburg, Hamburg, Germany, 2009.
13. Bock, M.K. Measuring the Electron Bunch Timing with Femtosecond Resolution at FLASH. Ph.D. Thesis, University of Hamburg, Hamburg, Germany, 2013.
14. Kuntzsch, M.; Zenker, K.; Maalberg, A.; Schwarz, A.; Czwalinna, M.K.; Kral, J. Update of the Bunch Arrival Time Monitor at ELBE. In Proceedings of the 13th International Particle Accelerator Conference, Bangkok, Thailand, 12–17 June 2022.
15. Rybaniec, R.; Przygoda, K.; Cichalewski, W.; Ayvazyan, V.; Branlard, J.; Butkowski, Ł.; Pfeiffer, S.; Schmidt, C.; Schlarb, H.; Sekutowicz, J. FPGA-Based RF and Piezocontrollers for SRF Cavities in CW Mode. *IEEE Trans. Nucl. Sci.* **2017**, *64*, 1382–1388. [CrossRef]
16. Wibowo, S. B.; Matsumoto, T.; Michizono, S.; Miura, T.; Qiu, F.; Liu, N. Digital low level rf control system for the International Linear Collider. *Phys. Rev. Accel. Beams* **2018**, *21*, 082004. [CrossRef]
17. Qiu, F.; Michizono, S.; Miura, T.; Matsumoto, T.; Liu, N.; Wibowo, S.B. Real-time cavity simulator-based low-level radio-frequency test bench and applications for accelerators. *Phys. Rev. Accel. Beams* **2018**, *21*, 032003. [CrossRef]
18. St. John, J.; Herwig, C.; Kafkes, D.; Mitrevski, J.; Pellico, W.A.; Perdue, G.N.; Quintero-Parra, A.; Schupbach, B.A.; Seiya, K.; Tran, N.; et al. Real-time artificial intelligence for accelerator control: A study at the Fermilab Booster. *Phys. Rev. Accel. Beams* **2021**, *24*, 104601. [CrossRef]
19. Kumar, V.K.P.; Tsai, Y.-C. Synthesizing optimal family of linear systolic arrays for matrix computations. In Proceedings of the International Conference on Systolic Arrays, San Diego, CA, USA, 25–27 May 1988.
20. Jang, J.-W.; Choi, S.B.; Prasanna, V.K. Energy- and time-efficient matrix multiplication on FPGAs. *IEEE Trans. Very Large Scale Integr. VLSI Syst.* **2005**, *13*, 1305–1319. [CrossRef]
21. Shen, J.; Qiao, Y.; Huang, Y.; Wen, M.; Zhang, C. Towards a Multi-array Architecture for Accelerating Large-scale Matrix Multiplication on FPGAs. In Proceedings of the 2018 International Symposium on Circuits and Systems, Florence, Italy, 27–30 May 2018.
22. Wei, X.; Yu, C.H.; Zhang, P.; Chen, Y.; Wang, Y.; Hu, H.; Liang, Y.; Cong, J. Automated Systolic Array Architecture Synthesis for High Throughput CNN Inference on FPGAs. In Proceedings of the 54th Annual Design Automation Conference, Austin, TX, USA, 18–22 June 2017.
23. Walter, T.; Ludwig, F.; Rehlich, K.; Schlarb, H. Novel Crate Standard MTCA.4 for Industry and Research. In Proceedings of the 4th International Particle Accelerator Conference, Shanghai, China, 12–17 May 2013.
24. Kuntzsch, M.; Steinbrück, R.; Schurig, R.; Hierholzer, M.; Killenberg, M.; Schmidt, C.; Hoffmann, M.; Iatrou, C.; Rahm, J.; Rutkowski, I.; et al. MicroTCA.4-Based LLRF for CW Operation at ELBE - Status and Outlook. In Proceedings of the 6th International Beam Instrumentation Conference, Grand Rapids, MI, USA, 20–24 August 2017.
25. Butkowski, Ł.; Kozak, T.; Prędki, P.; Rybaniec, R.; Yang, B.Y. FPGA Firmware Framework for MTCA.4 AMC Modules. In Proceedings of the 15th International Conference on Accelerator and Large Experimental Physics Control Systems, Melbourne, Australia, 17–23 October 2015.
26. Data Processing AMC Module for MTCA & ATCA. Available online: https://www.nateurope.com/products/NAT-AMC-TCK7.html (accessed on 30 March 2022).

27. Killenberg, M.; Petrosyan, L.M.; Schmidt, C.; Marsching, S.; Piotrowski, A. Drivers and Software for MTCA.4. In Proceedings of the 5th International Particle Accelerator Conference, Dresden, Germany, 15–20 June 2014.
28. Dimitrakopoulos, G.; Psarras, A.; Seitanidis, I. *Microarchitecture of Network-on-Chip Routers: A Designer's Perspective*; Springer Science+Business Media: New York, NY, USA, 2015; pp. 11–12.
29. Clements, A. *Principles of Computer Hardware*, 4th ed.; Oxford University Press Inc.: New York, NY, USA, 2006; pp. 134–136.
30. 7 Series FPGAs Data Sheet: Overview. Available online: https://docs.xilinx.com/v/u/en-US/ds180_7Series_Overview (accessed on 15 May 2022).
31. 7 Series DSP48E1 Slice: User Guide. Available online: https://docs.xilinx.com/v/u/en-US/ug479_7Series_DSP48E1 (accessed on 15 May 2022).
32. *IEEE Std 754-2019*; IEEE Standard for Floating-Point Arithmetic. (Revision of IEEE 754-2008). IEEE: Piscataway, NJ, USA, 2019.
33. Floating-Point Operator v7.1: LogiCORE IP Product Guide. Available online: https://docs.xilinx.com/v/u/en-US/pg060-floating-point (accessed on 15 May 2022).

Appendix 6

IV

A. Maalberg, M. Kuntzsch, K. Zenker, and E. Petlenkov. Regulation of electron bunch arrival time for a continuous-wave linac: Exploring the application of the $\mathcal{H}_2$ mixed-sensitivity problem. *Phys. Rev. Accel. Beams*, 26:072801, Jul 2023

Regulation of electron bunch arrival time for a continuous-wave linac: Exploring the application of the $\mathcal{H}_2$ mixed-sensitivity problem

Andrei Maalberg,* Michael Kuntzsch, and Klaus Zenker
Helmholtz-Zentrum Dresden-Rossendorf, 01328 Dresden, Germany

Eduard Petlenkov
Department of Computer Systems, Tallinn University of Technology, 19086 Tallinn, Estonia

(Received 31 January 2023; accepted 14 June 2023; published 10 July 2023)

Regulating the arrival time of electron bunches is a crucial step to improve the temporal resolution of accelerator-based pump-probe experiments. In this regard, an electron beam regulation method called beam-based feedback, has been shown to work well for stabilizing longitudinal beam properties on pulsed accelerator machines. Essentially, the method resembles a typical design of a proportional regulator, where the plant is represented by an electron beam response matrix, and where the inversion of such matrix produces the regulator. In recent years, however, linear accelerators that operate in a continuous-wave mode have received increasing attention. One of the key features of such machines is the improved statistics of measured data, which enables a high-resolution spectral analysis of the noise acting on the electron beam. This new insight allows us to reinterpret the electron beam regulation as a disturbance rejection goal, where the disturbance is based on measured frequency data. In this work, we show that the proportional beam-based feedback method has a principal performance limitation that becomes apparent by analyzing continuous-wave data. To improve this situation, we propose a regulator design that incorporates a dynamical disturbance model formulated in the context of the so-called $\mathcal{H}_2$ mixed-sensitivity problem. The designed regulator demonstrated excellent agreement between the model and measurements carried out at the continuous-wave linear accelerator ELBE and showed a potential to improve the proportional regulator approach.

DOI: 10.1103/PhysRevAccelBeams.26.072801

I. INTRODUCTION

Pump-probe experiments allow capturing the dynamics that occur in materials on an ultrafast timescale [1]. This is achieved by first exciting the dynamics in matter with an electromagnetic field of a pump pulse and then probing the excited matter with ultrashort photon pulses in a stroboscopic manner. To achieve a temporal resolution of less than a few tens of femtoseconds root-mean-square (rms) [2,3], these experiments rely on a tight synchronization between a pump source, which is typically an optical laser, and a source that generates the probes, e.g., a terahertz light source driven by an electron accelerator. Besides potential instabilities in the optical laser, the temporal stability of the electron accelerator, specifically of the underlying electron beam, is, therefore, of critical importance, which stresses the need to apply proper beam regulation.

Nowadays, an electron beam regulation method, called beam-based feedback, has been shown to work well for stabilizing longitudinal beam properties on pulsed accelerator machines [4–8]. Basically, the method first derives a matrix that denotes an electron beam response to variations in a radio-frequency (rf) field resonating inside an upstream accelerating structure, called cavity. The inverse of such matrix is then incorporated into the so-called low-level rf (LLRF) controller to allow adjusting the rf field based on the beam feedback. Finally, during an rf pulse, i.e., when the rf field is active, the LLRF controller can use the beam-based feedback to compensate for the noise acting on the beam. Putting aside the rf pulse details, the method resembles a typical design of a proportional regulator, where the beam response matrix represents a plant and where the plant inversion produces a regulator.

Contrary to the pulsed operation, a continuous-wave (cw) mode fills the accelerating cavities with a continuously driven rf field. That is, an rf field with a 100% duty cycle. For the user, such mode allows flexible electron bunch repetition rates and a high average beam current.

*a.maalberg@hzdr.de

Published by the American Physical Society under the terms of the Creative Commons Attribution 4.0 International license. Further distribution of this work must maintain attribution to the author(s) and the published article's title, journal citation, and DOI.

This enables experiments that would otherwise be impossible to perform. In addition, a continuous train of electron bunches maintained for a sufficient amount of time greatly improves the statistics of experiment data. Consequently, linear accelerators (linacs) operating in the cw mode have received increasing attention in recent years. In particular, the construction of the Shanghai hard x-ray free electron laser facility (SHINE) began in 2018 [9]. The Linac Coherent Light Source II (LCLS-II) is nearing completion [10]. Moreover, the European X-ray Free Electron Laser (EuXFEL) considers a cw upgrade in the foreseeable future [11]. In this context, the electron linear accelerator for beams with high brilliance and low emittance (ELBE) [12] has been operating in cw mode for nearly 20 years and, therefore, represents a unique environment to test new algorithms and beamline components [13,14]. Hence, the results that are obtained at ELBE may have a substantial impact on the growing cw community.

Besides the user benefits, the improved statistics also help enhance feedback-related beam diagnostics. For example, a 1-s sampling of the rf field by a 50-kHz electron beam, i.e., a beam with a 50-kHz bunch repetition rate, provides data for a spectrum with a frequency resolution of 1 Hz. Since the electron bunches sample the inherent rf noise as well, a high-resolution spectral analysis of such noise becomes feasible. Clearly, this opens a possibility to reinterpret the electron beam regulation as a disturbance rejection goal, where the disturbance is based on the frequency-domain data of a measured electron beam signal. In this work, we exploit this opened possibility to address the regulation of an electron bunch arrival time. Specifically, we propose a solution that incorporates a dynamical disturbance model formulated in the context of the so-called $\mathcal{H}_2$ mixed-sensitivity problem. Even though design methods based on the $\mathcal{H}_2$ norm have already been used in the field of accelerators, e.g., to regulate an optical synchronization system [15–17], it is of interest to study the application of such methods to regulate the electron bunch arrival time on a cw machine. In this context, our designed regulator demonstrates excellent agreement between the model and measurements carried out at the cw linac ELBE and shows a potential to improve the proportional regulator.

The remainder of this paper is organized as follows: Section II starts by introducing the physics behind the beam-based feedback method and then continues the discussion from a control engineering point of view. Special attention is devoted to the performance limitation of the commonly used proportional regulator. In order to resolve the limitation, Sec. III proposes an improvement that is implemented in terms of a certain control engineering concept, called $\mathcal{H}_2$ mixed-sensitivity problem. Section IV evaluates the proposed improvement on the cw linear accelerator ELBE. Finally, Sec. V concludes the paper.

II. BEAM-BASED FEEDBACK METHOD

The state of a single particle is usually expressed relative to a reference trajectory, where the trajectory is assumed to be the path of a reference particle with nominal parameters. This allows us to define a Cartesian frame moving with the reference particle and providing the corresponding x, y, and z coordinates. Moreover, this concept can be generalized to represent an ensemble of particles, e.g., an electron bunch, by treating the ensemble as its center of mass. It is therefore common to describe the state as a six-dimensional phase space vector [18]

$$\rho = [x \quad x' \quad y \quad y' \quad z \quad \delta]^T, \tag{1}$$

where x, y, and z are the distances from the reference trajectory, $x' = \partial_x/\partial_z$ and $y' = \partial_y/\partial_z$ are the horizontal and vertical derivatives, respectively, and where $\delta = \Delta E/E_0$ is a relative deviation from the reference energy. To first order, the x, y, and z components can be decoupled, and thus, we can neglect the rest of the phase space and concentrate only on the longitudinal part

$$\rho_L = [z \quad \delta]^T. \tag{2}$$

The main beamline section that is able to change the longitudinal state ρ_L is called bunch compressor [18–20]. It is a combination of an rf cavity and a magnetic structure called chicane, formed by a minimum of four dipole magnets. The rf cavity is operated off-crest in order to chirp the bunch, i.e., to imprint an energy modulation that correlates with the longitudinal position z within the bunch. Correspondingly, the transfer map of the rf cavity can be expressed as

$$z(s_1) = z(s_0), \tag{3}$$

$$\delta(s_1) = \delta(s_0) + \frac{eA}{E_0}\cos\left(\frac{\omega}{c}z(s_0) + \phi\right), \tag{4}$$

where e is an elementary charge, c is the speed of light, and where A, ϕ, and ω are the amplitude, phase, and angular frequency of the rf cavity field, respectively. Beamline locations s_0 and s_1 mark the start and end of the rf cavity section, respectively. Then, by means of energy dispersion, the magnets of the chicane force the electrons to travel different paths, depending on the electron energy. Using only first-order terms, the corresponding transfer map is denoted as

$$z(s_2) = z(s_1) + R_{56}\delta(s_1), \tag{5}$$

$$\delta(s_2) = \delta(s_1), \tag{6}$$

where R_{56} is a first-order design parameter of the magnetic chicane that translates the energy modulation into a

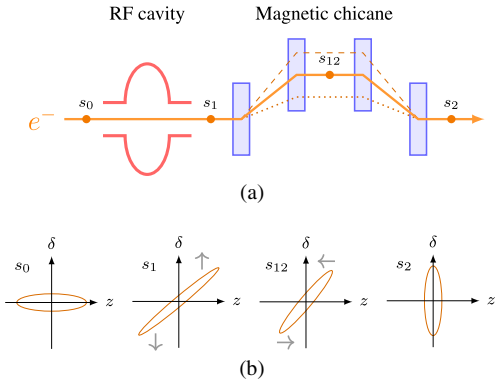

FIG. 1. Schematic of a bunch compressor exhibiting (a) the combination of an rf cavity and a magnetic chicane, as well as (b) the evolution of the longitudinal phase space of passing electron bunches.

longitudinal position change. Beamline locations s_1 and s_2 mark the start and end of the magnetic chicane section, respectively. Following this, the concept of the bunch compressor is illustrated in Fig. 1. It can be seen how electrons travel different paths through the magnetic chicane, depending on the energy received from the rf cavity. So in principle, the bunch compressor changes the longitudinal phase space of the electrons in a two-step sheering process: First, the rf cavity changes the energy distribution within the bunch; and second, the magnetic chicane alters the electron positions accordingly.

In case of arrival time, the electron bunch is represented by its center of mass. Thus, setting $z = 0$ and focusing only on the energy modulation introduced by the rf cavity allows transforming (3) into

$$\Delta\delta = \frac{eA}{E_0}\cos\phi. \tag{7}$$

This leads to a similar update of (5) featuring, in addition, a conversion to proper arrival time units

$$\Delta\tau = \frac{1}{v}R_{56}\Delta\delta, \tag{8}$$

where τ is the arrival time in seconds, and where $v \approx c$ and denotes the velocity of a relativistic electron bunch. So according to (7) and (8), where v and R_{56} are static for a given setting, the arrival time of the electron bunch can be regulated by modulating its energy. Usually, this modulation is performed with the help of an rf actuator, i.e., a control loop that allows setting and stabilizing the amplitude and phase of an rf field. To give a concrete example, the rf field control loop that is responsible for the bunch compressor at ELBE consists of a superconducting rf (SRF) cavity and a digital LLRF controller. The loop shows rms field stability of 0.005% in amplitude and 0.01° in phase [21]. Principally, this means that there are two rf field variables that the beam-based feedback can use to modulate the bunch energy. Yet according to (7), the rf field amplitude A is more linear than the phase ϕ. Moreover, changing ϕ changes the bunch compression, which is not desirable in this case. It is therefore reasonable to consider the phase ϕ a constant and define the output of the beam-based feedback regulator in terms of A exclusively, i.e.,

$$a = \frac{\Delta A}{A} \times 100, \tag{9}$$

where a is a change in percent with respect to the absolute rf field amplitude.

Meanwhile, the applied energy modulation leads to arrival time changes that can be measured downstream of the bunch compressor using an appropriate sensor. A bunch arrival time monitor (BAM) that is installed at ELBE may serve as an example of such sensor. It is able to measure the arrival time of the passing electron bunches with a time resolution of 4 fs rms at a bunch charge of 225 pC [22]. Finally, adding a beam-based feedback to regulate the electron bunch arrival time τ extends the bunch compressor schematic by cascaded control loops, i.e., the already existing rf field control loop becomes the so-called inner loop, whereas the added beam-based feedback forms the outer loop, see Fig. 2.

To design the corresponding beam-based feedback regulator, we may cast the extended bunch compressor to a single-input single-output (SISO) control problem, where τ is a controlled process variable and a is a control signal. The bunch compressor then represents a plant, where W_δ converts the control signal a to the absolute rf field amplitude A and G_δ and G_τ are (7) and (8), respectively. According to this simple design, the dynamics of the rf actuator are neglected. Instead, the beam-based

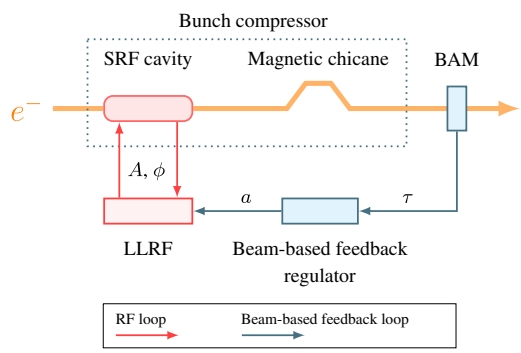

FIG. 2. Schematic of a bunch compressor extended by cascaded control loops to regulate an electron bunch arrival time.

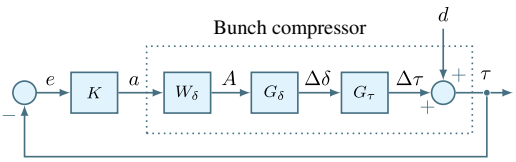

FIG. 3. Beam-based feedback regulation cast to a SISO control problem that is based on the first principles derived from the bunch compressor.

feedback regulator K acts directly on the bunch compressor in order to compensate for an error e, i.e., a negative impact of some unknown disturbance d on the process variable τ, see Fig. 3.

The origin of disturbance d is twofold: the rf noise inherent to the rf cavity [23] and the initial arrival time jitter of the passing electron bunches. In any case, the signal d represents a generalization, e.g., a unit step. To counteract such disturbance, it is straightforward to let K be an inverse of the bunch compressor plant, i.e.,

$$K = \gamma G_{BC}^{-1}, \tag{10}$$

where

$$G_{BC} = G_\tau G_\delta W_\delta = \frac{1}{v} R_{56} \frac{eA}{E_0} \cos\phi \frac{1}{100}, \tag{11}$$

and where γ is an additional gain to adjust the regulator performance. In fact, the value of G_{BC} can be determined analytically by evaluating (11) with corresponding parameters. Since we aim to regulate the ELBE accelerator, we evaluate G_{BC} with ELBE bunch compressor parameters from Table I. We are interested in finding the amount of variation in τ, given the input parameter $a = 1$. In this case, G_{BC} yields 776 fs/%. Essentially, the resulting scalar plant represents an electron beam response to variations in the rf field. The scalar variant can also be replaced by a matrix, provided there are more beam sensors available. The inverse of such matrix produces a proportional regulator K.

Even though the presented analytical formulation of G_{BC} captures the ultimate concept of the bunch compressor, it is still too simplified to match reality. The phase space of an electron bunch entering the bunch compressor may be far more complicated [24] than a simple ellipse illustrated in Fig. 1. This is why, a common engineering practice is to measure the beam response on a real machine, while

TABLE I. Bunch compressor parameters at ELBE.

Parameter	Value
rf field amplitude A of a chirping SRF cavity	7.27 MV
Off-crest rf field phase ϕ of a chirping SRF cavity	−21 deg
Reference energy E_0 of a magnetic chicane	28 MeV
R_{56} of a magnetic chicane	96 mm

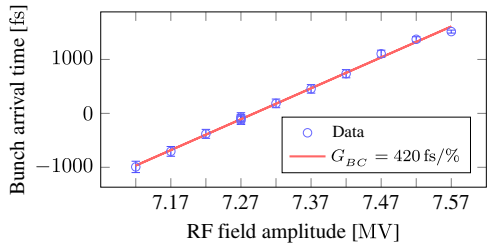

FIG. 4. Measuring the response of the electron bunch arrival time at ELBE, while changing the setpoint of the rf field amplitude $A = 7.27$ MV by steps of 50 kV.

changing the rf field in a stepwise manner. The ELBE bunch compressor, configured according to Table I, yields about 420 fs/% as a result of such measurement, see Fig. 4.

To cross-check the measured beam response, we use the final value theorem [25]. This theorem shows the final value of $e(t)$, i.e., the error of a closed-loop system, as t approaches infinity. So the idea of the cross-check is to first find γ that corresponds to the measured $e(\infty)$. Knowing the value of K that was applied during the measurement, we can then use the found γ to determine G_{BC} from (10). Therefore, given our assumption that disturbance d is a unit step, the theorem is defined as

$$e(\infty) = \frac{1}{1 + \lim_{s\to 0} L(s)}, \tag{12}$$

where s is the Laplace variable, and where the limit of a constant open-loop transfer function $L = G_{BC}K$ can be evaluated with the help of (10), yielding

$$\lim_{s\to 0} G_{BC}K = G_{BC}K = \gamma G_{BC} G_{BC}^{-1} = \gamma. \tag{13}$$

By substituting the limit in (12) with (13), we can express $e(\infty)$ as a function of γ, i.e.,

$$e(\infty) = \frac{1}{1+\gamma}. \tag{14}$$

Then, we define $e(\infty)$ as

$$e(\infty) \equiv \frac{\tau_o}{\tau_i}, \tag{15}$$

where τ_i and τ_o denote the integrated rms jitter of the electron bunch arrival time measured at ELBE with the proportional feedback off and on, respectively, see Fig. 5.

So by substituting $e(\infty)$ in (14) with (15), we are able to express γ as a function of the measured arrival time ratio, namely

$$\gamma = \frac{\tau_i}{\tau_o} - 1. \tag{16}$$

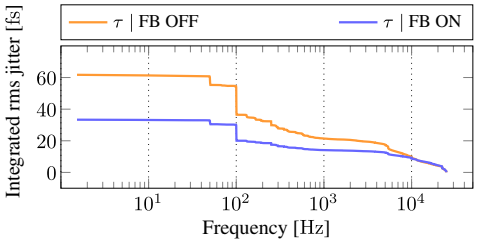

FIG. 5. Integrated rms jitter of the electron bunch arrival time measured at ELBE with the proportional feedback off and on.

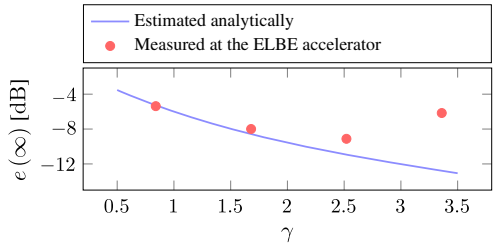

FIG. 6. Performance of a set of proportional regulators K, when G_{BC} is tied to the ELBE beam response of 420 fs/%, but γ is intentionally varied.

Finally, when evaluated with values from Table II, (16) and (10) yield $\gamma = 0.85$ and $G_{BC} = 427$ fs/%, respectively. The cross-checked value of G_{BC} indicates the validity of the beam response reported earlier.

Choosing $\gamma < 1$ to evaluate G_{BC} is characterized by a need to avoid triggering the degradation of the regulator performance. Specifically, increasing γ on the real machine does not reduce $e(\infty)$ according to an analytical estimation in (14) but rather causes (15) to substantially deviate, see Fig. 6.

The performance degradation observed on the real machine exposes the principal drawback of proportional regulators, namely the lack of bandwidth specification. Basically, such regulators apply control action across the whole frequency spectrum, which may cause interference with other control system components, mostly the actuators. For example, the above-mentioned rf actuator may exhibit dynamics with a certain bandwidth and gain margin. While the former property characterizes the speed of the actuator, the latter one defines how much gain can be additionally introduced into the closed-loop system before turning it unstable [25]. In this situation, the absence of a proper bandwidth specification makes the proportional regulator part of the actuator dynamics and, therefore, forces it to rely on the actuator gain margin. Derived from [21], the LLRF system at ELBE has a bandwidth of about 35 kHz and a gain margin of 11.6 dB. So theoretically, setting $\gamma \approx 3.8$ will consume the gain margin completely and, thus, turn the system unstable. Yet practically, we observe strong plant oscillations above 10 kHz already when $\gamma \approx 3.36$, see Fig. 7.

In this case, an *ad hoc* solution would be a trade-off between the noise suppression and plant stability. For example, setting $\gamma \approx 2.52$ achieves a suppression of the rms jitter by a factor of 3, i.e., only 22 fs rms jitter remains, while causing a moderate plant oscillation, see Fig. 8.

The displayed trade-off gives rise to the problem of finding a regulation approach that is able to achieve good noise suppression without compromising the plant's stability. In comparison to the displayed settings of the proportional regulator, the new approach should perform similarly to $\gamma \approx 0.85$ in the high-frequency range, but preferably better than $\gamma \approx 2.52$ in the low-frequency range. Therefore, in this study, we aim to take the actual noise explicitly into account. This means shifting the focus of attention from the analytical formulation to the size of a

TABLE II. Regulation of the electron bunch arrival time at ELBE using the proportional regulator.

Parameter	Value	Remark
τ_i	61.9 fs	rms integration range 1.5 Hz–25 kHz
τ_o	33.4 fs	rms integration range 1.5 Hz–25 kHz
K	0.002 fs/%	

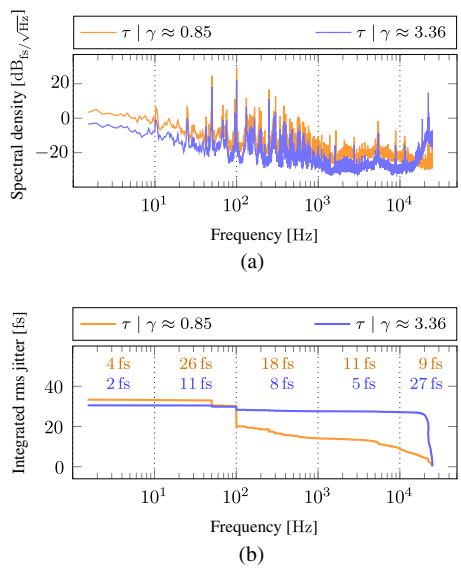

FIG. 7. Regulation of a 50-kHz electron beam at ELBE using a proportional regulator. (a) Setting $\gamma \approx 3.36$ triggers a pronounced plant oscillation above 10 kHz. (b) When calculating the rms jitter, this oscillation results in a large integration step, which negates the applied suppression effort, compared to a less aggressive regulator.

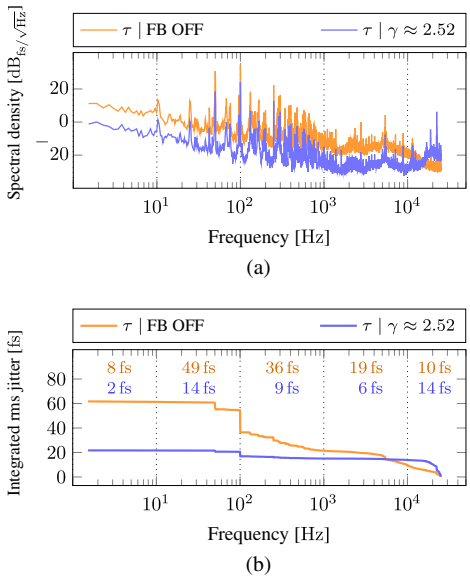

FIG. 8. Regulation of a 50-kHz electron beam at ELBE using a proportional regulator. (a) Setting $\gamma \approx 2.52$ causes a moderate oscillation above 10 kHz. (b) Nevertheless, the set γ allows suppressing the integrated rms jitter by a factor of 3.

concrete disturbance signal. So contrary to the proportional regulator, the new regulator K will try to compensate for the impact of a known disturbance d on the process variable τ. Obviously, the updated beam-based feedback method will have to ensure (i) a proper bandwidth definition in order to decouple the new regulator dynamics from the LLRF loop; (ii) a natural ability to incorporate a dynamical disturbance model inside the regulator design; (iii) a correspondence between the regulator performance criterion and the ultimate goal to suppress the rms value of the electron beam fluctuations.

To satisfy these requirements, we employ a regulator design method that is based on the $\mathcal{H}_2$ mixed-sensitivity problem [26,27]. On the one hand, this new regulator design represents a frequency-dependent optimization procedure. Hence, we can use a frequency-domain specification of the disturbance signal d. On the other hand, the designed regulator is expected not only to stabilize the plant model but also to minimize the rms fluctuations of the model output. Since the $\mathcal{H}_2$ norm of a model is directly related to the rms value of its output, minimizing such norm matches well our physical problem.

III. $\mathcal{H}_2$ MIXED-SENSITIVITY PROBLEM

The $\mathcal{H}_2$ norm of a transfer function G_d measures the rms response of the output when the input is driven by a white noise excitation [26,28]. The norm is denoted as

$$\|G_d\|_2 \triangleq \sqrt{\frac{1}{2\pi}\int_{-\infty}^{\infty} |G_d(j\omega)|^2 d\omega}, \tag{17}$$

where $|G_d(j\omega)|$ designates the magnitude frequency response of G_d evaluated at angular frequency ω. Suppose now that G_d defines the dynamics of a stochastic disturbance d that acts on the electron bunch arrival time τ. By using this transfer function together with its $\mathcal{H}_2$ norm as design specifications, the beam-based feedback regulator K can be aimed at reducing the sensitivity of τ to rms perturbations coming from d. Such interpretation allows formulating the beam-based feedback regulation in terms of the $\mathcal{H}_2$ mixed-sensitivity problem, see Fig. 9. According to such formulation, models G_d and G_n define the transfer functions of the electron beam disturbance d and the sensor measurement noise n, respectively. In addition, frequency weights W_S and W_{KS} help shaping the regulator performance and produce error signals w_S and w_{KS} that are used by an optimization procedure. Finally, as shown below, we define a specific bandwidth to decouple the designed regulator from the LLRF dynamics. This allows us to omit the rf field control loop from the design and continue using G_{BC} as the plant model.

Compared to the initial beam-based feedback control system, the main feature of the new design is the inclusion of the disturbance model G_d. This dynamical model is based on electron bunch arrival time data measured downstream of the ELBE bunch compressor. The model approximates the slopes of a linear spectral density derived from the data. That is, the model can be interpreted as a filter that shapes a theoretical white noise signal into the frequency content of the arrival time data. Importantly, to reflect the size of the measured signal, the $\mathcal{H}_2$ norm of the model is adjusted to satisfy

$$\|G_d\|_2 \approx \sqrt{\int_{f_1}^{f_2} [\tilde{\tau}(f)]^2 df}, \tag{18}$$

where $\tilde{\tau}(f)$ denotes the linear spectral density of the arrival time data τ in femtoseconds evaluated at frequency f, and

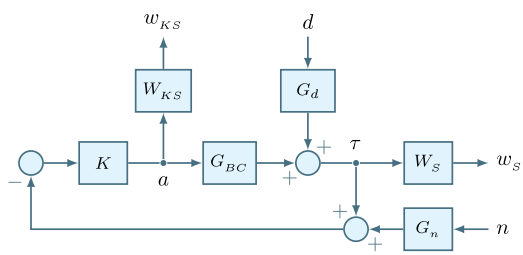

FIG. 9. Regulation of an electron bunch arrival time expressed in terms of the $\mathcal{H}_2$ mixed-sensitivity problem.

where $f_1 = 1$ Hz and $f_2 = 3.5$ kHz for a 50-kHz electron beam. Choosing 3.5 kHz as the upper integration limit has a couple of reasons. First, we know that the majority of the noise resides below 1 kHz [23], so we can use this information as a design constraint. Second, the designed $\mathcal{H}_2$ regulator aims to achieve decoupling from the LLRF dynamics [29], and this is accomplished by targeting a regulation bandwidth of 3.5 kHz, i.e., 1 order of magnitude lower than the 35 kHz bandwidth of the LLRF. Therefore, by choosing the locations of poles and zeros to reflect the frequency-domain shape of measured electron bunch arrival time noise, the transfer function G_d can be defined as

$$G_d(s) = \alpha \frac{s + z_0}{(s + p_0)(s + p_1)}, \tag{19}$$

where z_0 denotes the location of a zero at 500 rad/s, and where p_0 and p_1 are two pole locations at 50 and 5000 rad/s, respectively. The scalar parameter $\alpha = 4.1727 \times 10^3$ is used to satisfy (18). Hence, the norm $\|G_d\|_2$ yields 59 fs rms, which is, indeed, the majority of the noise when compared to the overall jitter of 62 fs rms. Accordingly, $G_d(s)$ represents an appropriately scaled second-order dynamical system with a 20-dB roll-off after 1 kHz, see Fig. 10.

By putting the disturbance model G_d into the context of the $\mathcal{H}_2$ mixed-sensitivity problem, the electron bunch arrival time signal can be expressed as

$$\tau = \underbrace{(1 + L)^{-1}}_{S} G_d d, \tag{20}$$

where $L = G_{BC}K$ and denotes an open-loop transfer function and S is a closed-loop transfer function called the sensitivity function. Inspection of (20) shows that we can reduce the sensitivity to disturbance input d by properly shaping S. Specifically, the shaping is performed in the frequency domain with the help of a frequency weight

$$W_S(s) = \frac{s/M_S + \omega_S}{s + \omega_S A_S}, \tag{21}$$

where $W_S(s)$ is a first-order low-pass filter, and where A_S and M_S define the low- and high-frequency gains, respectively. Parameter ω_S specifies an approximate bandwidth of the designed regulator. A typical guideline [26,27] is to make S small in the low-frequency range to achieve better disturbance rejection. For this purpose, we can use the low-frequency gain A_S to specify the desired suppression of G_d, see Fig. 11.

Another relevant closed-loop transfer function is related to the control signal a. This signal is generated by the beam-based feedback regulator K as a response to a perturbed electron bunch arrival time τ. Since the generated signal is used to manipulate the amplitude setpoint of the rf cavity field, our goal is to limit the control energy in order to avoid sensitivity to any unmodeled rf dynamics. This is accomplished by shaping the so-called input sensitivity function KS, which represents a link between the disturbance input d and control signal a, namely

$$a = KSG_d d. \tag{22}$$

Similar to the shaping of S, we shape the input sensitivity function KS using a frequency weight

$$W_{KS}(s) = \frac{s + \omega_{KS} A_{KS}}{s/M_{KS} + \omega_{KS}}, \tag{23}$$

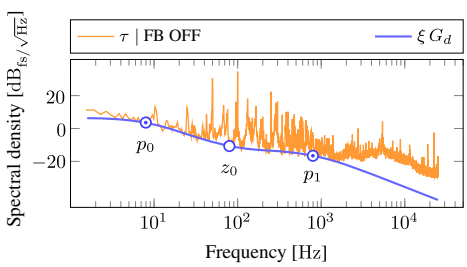

FIG. 10. Designing the disturbance model G_d to match the electron bunch arrival time noise up to 1 kHz. It is important to note that adherence to (18) makes the magnitude of G_d slightly greater than the noise shape. Consequently, for demonstration purposes, we use an extra parameter $\xi = 0.25$ to align the slopes.

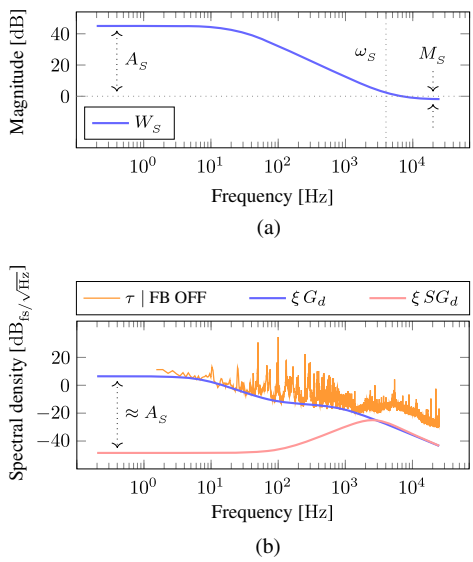

FIG. 11. Shaping the sensitivity function S using (a) a frequency weight W_S to (b) suppress the disturbance model G_d into its shaped closed-loop counterpart SG_d. For demonstration purposes, the extra parameter $\xi = 0.25$ aligns the slopes.

where $W_{KS}(s)$ is a first-order high-pass filter, and where A_{KS} and M_{KS} define the low- and high-frequency gains, respectively. Again, the parameter ω_{KS} is linked to the regulator bandwidth. The main objective is to increase the high-frequency roll-off of the closed-loop transfer function KSG_d by increasing the high-frequency gain M_{KS}. The steeper the roll-off, the less action is applied by the regulator beyond its bandwidth. Meanwhile, the low-frequency range of KSG_d follows the shape of the disturbance model G_d with a magnitude offset defined by G_{BC}^{-1}, see Fig. 12.

The sensor measurement noise model G_n is used to regularize the so-called sensor singularity at $\omega = \infty$. The fact is that the optimization procedure assumes that the sensor measurement τ has noise at every frequency, $\omega = \infty$ included. Yet the actual disturbance model G_d is defined by a strictly proper transfer function, such that

$$\omega \to \infty\colon\ G_d(j\omega) \to 0. \tag{24}$$

Consequently, to eliminate the singularity, the sensor measurement τ is redefined as $\tau + G_n n$, where G_n is a small nonzero constant. Interestingly, G_n can also be used as an effective bandwidth tuning knob. Together with ω_S and ω_{KS}, this parameter establishes the following regulator tuning procedure (i) Set parameters A_S, M_S, A_{KS}, and M_{KS} according to the specification, e.g., $A_S = 10^{\beta/20}$, where $\beta = -45$ dB; (ii) set parameters ω_S and ω_{KS} about equal to the bandwidth requirement or somewhat larger. Simultaneously, keep $\omega_S \le \omega_{KS}$; (iii) adjust the scalar G_n to align the bandwidth of the complementary sensitivity function $T = SL$ with the bandwidth requirement; (iv) adjust parameters ω_S and ω_{KS} as well as G_n to improve correspondence to the specification. Following this, Table III summarizes design parameters for a regulator that targets a bandwidth of about 4 kHz while suppressing the low-frequency noise by roughly 50 dB. By increasing the regulator bandwidth from 3.5 kHz to about 4 kHz, we aim to stress the decoupling test on the real machine.

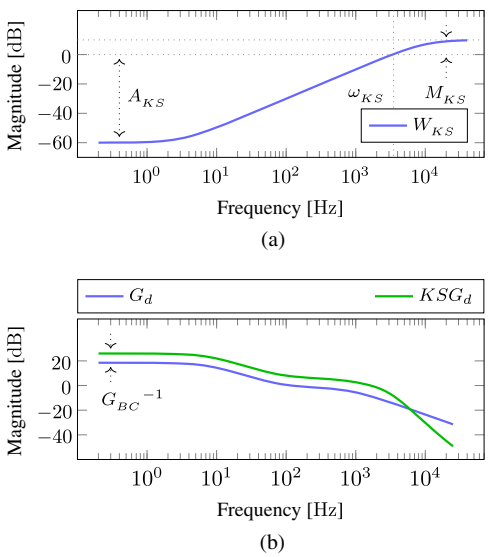

FIG. 12. Shaping the input sensitivity function KS using (a) a frequency weight W_{KS} to (b) increase the high-frequency roll-off of the closed-loop transfer function KSG_d.

Meanwhile, the synthesis of the $\mathcal{H}_2$ regulator is performed by a MATLAB function `h2syn` from the Robust Control Toolbox [30]. As the main input, the function expects a state-space model that resembles an interconnection of the blocks and signals displayed in Fig. 9, but with no regulator K to close the loop. As such, the interconnected model features inputs $[d\, n\, a]^T$ and outputs $[w_S\ w_{KS}\ \tau]^T$. This kind of interconnection is usually called a generalized, or augmented, plant. One possible way to prepare the generalized plant is to create the required block interconnection in SIMULINK, populate these blocks with model data, and then use a MATLAB function `linmod` [31] to extract a model of the generalized plant. Since the extracted model is in a state-space form, it is represented by matrices A, B, C, and D, which denote the system, input, output, and feedforward matrices, respectively. For the purpose of synthesizing the regulator K for this generalized plant, the function `h2syn` attempts to solve an optimization task. It amounts to finding a stabilizing regulator K that is able to minimize the $\mathcal{H}_2$ norm of a transfer function from the disturbance signal d to the error signals w, i.e.,

$$\begin{bmatrix} w_S \\ w_{KS} \end{bmatrix} = \begin{bmatrix} W_S S G_d \\ W_{KS} K S G_d \end{bmatrix} d. \tag{25}$$

Along with a state-space model of the synthesized regulator K, the function `h2syn` produces a full-state feedback gain K_u and an observer gain L_x, both returned as matrices. The relevance of these gains becomes evident, once we start discussing the relation between the states of the generalized plant and a real machine. In addition, the

TABLE III. $\mathcal{H}_2$ regulator design parameters.

Parameter	Value	Remark
$\lVert G_d \rVert_2$	59 fs	rms amount of expected noise
G_{BC}	420 fs/%	
G_n	0.00018	
A_S	0.0056	−45 dB
M_S	1.26	2 dB
ω_S	26 000 rad/s	4.14 kHz
A_{KS}	0.001	−60 dB
M_{KS}	3.16	10 dB
ω_{KS}	28 000 rad/s	4.46 kHz

manual regularization, which we apply with the help of the scalar G_n, allows us to switch off the automatic one applied by the function `h2syn`. Finally, the result of the regulator synthesis can be visualized in terms of the most relevant transfer functions, see Fig. 13.

As can be seen, the combination of S and KS sensitivity functions, often referred to as S/KS, plays the main role in shaping the desired behavior of the presented $\mathcal{H}_2$ mixed-sensitivity problem. Of course, this shaping adds a certain overhead to the design, because now the plant model is not merely the scalar G_{BC}, but the generalized plant, which includes the second-order disturbance model G_d, as well as the first-order shaping filters W_S and W_{KS}. As a result, we have a plant with four states, which essentially have no physical relation to the real machine and thus cannot be directly measured. To resolve this issue, the regulator K relies on state observation. That is, the regulator consists of two parts, namely (i) a dynamical state observer system, which estimates the state vector $\hat{x}$ and (ii) the above-mentioned full-state feedback matrix K_u, which uses the estimated states to produce an optimal control signal a, see Fig. 14. The matrices A, B, and C are derived from the state-space representation of the generalized plant obtained by the function `linmod`.

Mathematically, the observer-based structure of the beam-based feedback regulator K is expressed in a state-space form as

$$\dot{\hat{x}} = A\hat{x} + Ba + L_x(\tau - C\hat{x}), \tag{26}$$

$$a = K_u\hat{x}. \tag{27}$$

Converted to their discrete-time form, (26) and (27) can be implemented on a real-time field-programmable gate array-based digital platform [32]. By using the resulting digital implementation to close the loop on the real machine, we can finally validate the concept of the proposed beam-based feedback method. In particular, the ability to decouple the beam-based feedback from the LLRF dynamics in order to achieve greater noise suppression without triggering the unwanted plant oscillations. In addition, we can verify our performance estimations shown in Table IV.

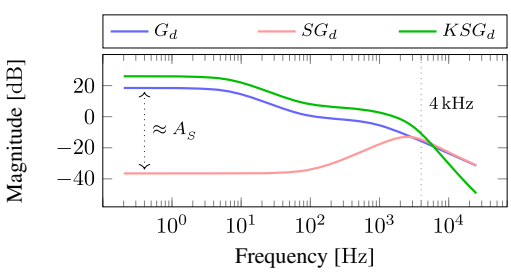

FIG. 13. $\mathcal{H}_2$ regulator visualized in terms of its transfer functions. The closed-loop transfer functions SG_d and KSG_d are clearly tailored to the disturbance model G_d.

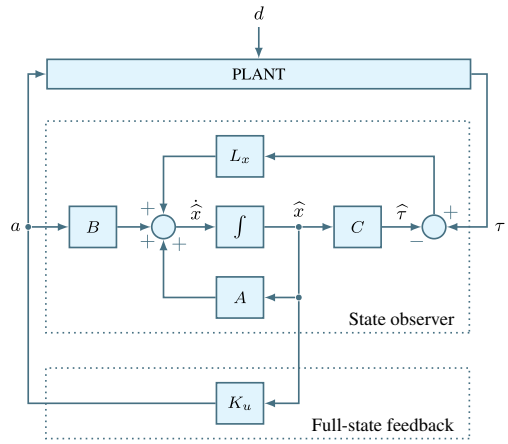

FIG. 14. Observer-based structure of the regulator K designed in terms of the $\mathcal{H}_2$ mixed-sensitivity problem.

IV. EVALUATING $\mathcal{H}_2$ REGULATOR AT ELBE

To evaluate the performance of the proposed $\mathcal{H}_2$ regulator, we conducted measurements on the cw linac ELBE. The layout of the measurement setup was equivalent to the proportional scheme displayed in Fig. 2. Accordingly, the bunch compressor was configured as shown in Table I. The compressed electron bunches with a bunch charge of 225 pC were then measured by the BAM with a time resolution of 4 fs rms. The result of this measurement demonstrated that in principle, the $\mathcal{H}_2$ regulator is able to achieve good noise suppression without triggering the plant oscillations, see Fig. 15. Specifically, the residual jitter amounts to 19 fs rms with the majority of it coming from frequency ranges, where the regulator is not active, i.e., above 1 kHz.

Moreover, the demonstrated correspondence between the model and arrival time data, both in open- and closed-loop cases, also applies to the control effort data. That is, the frequency-domain data of the control signal a follows the magnitude frequency response of the KSG_d transfer function up to 1 kHz. After this frequency, however, a flattens, as τ ascends to the peak located at approximately 5 kHz.

TABLE IV. Estimated performance parameters of the $\mathcal{H}_2$ beam-based feedback regulator.

Parameter	Value	Remark
$\lVert SG_d \rVert_2$	23 fs	rms amount of residual noise
$\lVert KSG_d \rVert_2$	0.14%	rms amount of regulation effort

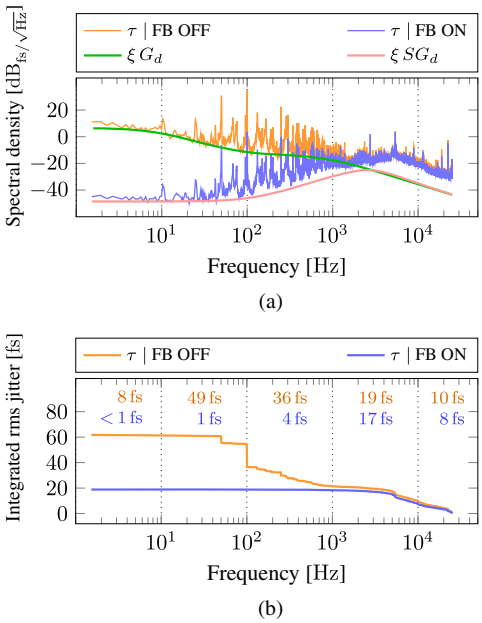

FIG. 15. Regulation of a 50-kHz electron beam at ELBE using the $\mathcal{H}_2$ regulator. (a) In the frequency domain, machine data exhibit correspondence with the model. (b) Simultaneously, integrated rms jitter data show that the regulator achieves good noise suppression below 1 kHz.

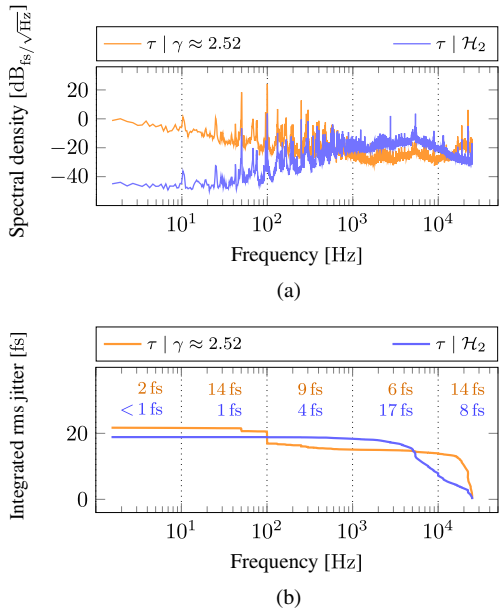

FIG. 17. Comparing performance between the proportional beam-based feedback method with $\gamma \approx 2.52$ and the $\mathcal{H}_2$ regulator. (a) The frequency domain clearly shows the different behaviors of both regulators depending on the frequency range. (b) This difference can also be seen while examining the band-limited amounts of the integrated rms jitter.

Once τ starts its descent, a can finally demonstrate the designed high-frequency roll-off, see Fig. 16. Also, the estimated parameters from Table IV turn out to be more conservative than our measurements. That is, the integration of a yields 0.13% rms, whereas the estimated parameter is 0.14% rms.

Therefore, the absence of the plant oscillations indicates a successful validation of the $\mathcal{H}_2$ regulator with respect to its decoupling from the LLRF dynamics. Compared to the proportional beam-based feedback method, the $\mathcal{H}_2$ regulator not only leaves the high frequencies intact but also shows superior suppression within its band of frequencies, see Fig. 17.

Finally, to better appreciate the achieved regulation of the electron bunch arrival time, one can view the

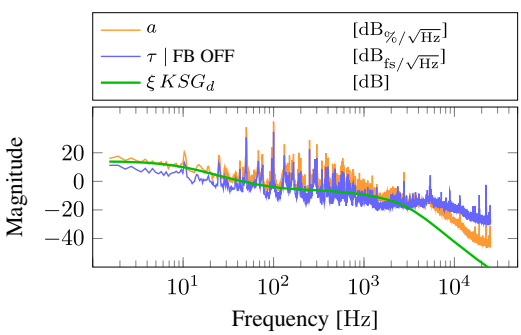

FIG. 16. Control effort to regulate a 50-kHz electron beam at ELBE using the $\mathcal{H}_2$ regulator. For demonstration, the extra parameter $\xi = 0.25$ aligns KSG_d with the slope of a.

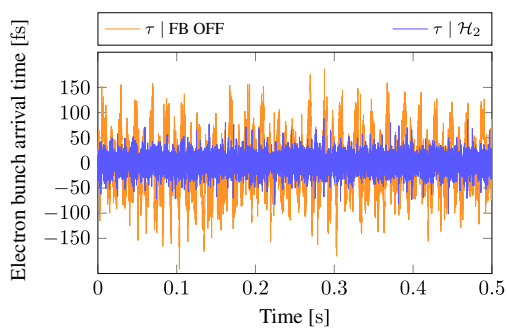

FIG. 18. Regulation of a 50-kHz electron beam at ELBE as observed in the time domain. The beam fluctuations are reduced using the $\mathcal{H}_2$ regulator.

result in the time domain, see Fig. 18. Indeed, large slow fluctuations disappear as the $\mathcal{H}_2$ regulator counteracts them, whereas small fast ones prevail. This is a natural outcome of applying a band-limited regulator that focuses on low-frequency range.

V. CONCLUSIONS

The increasing interest in superconducting linacs that operate in a cw mode enables the exploration of new capabilities in the design of a beam-based feedback method. The improved statistics of measured data allow reinterpreting the beam-based feedback as a disturbance rejection goal, where the disturbance is based on high-resolution frequency spectra of the measured data. Following this, S/KS disturbance rejection designs, such as the $\mathcal{H}_2$ mixed-sensitivity problem, become feasible.

In this work, we proposed a new design of a beam-based feedback regulator that exploits possibilities opened by the cw mode. The design seeks to minimize the noise of an electron bunch arrival time. Compared to a frequently used proportional regulator, the proposed design takes beam disturbance explicitly into account. Due to the low-frequency nature of this disturbance, it is possible to specify the design bandwidth accordingly and, thus, decouple the new regulator from the actuator dynamics. As a result, a specific plant instability, which is easily triggered by the proportional approach, poses no problem for the $\mathcal{H}_2$ regulator.

Despite its limited bandwidth, the designed $\mathcal{H}_2$ regulator demonstrated good noise suppression during an evaluation at the cw linac ELBE. Specifically, the electron bunch arrival time noise was reduced by a factor of 3, i.e., from 62 fs rms down to 19 fs rms. The corresponding frequency-domain data showed that a single regulation stage, which was installed at the end of the beamline, was sufficient to suppress low-frequency bands, i.e., from 1 Hz to 1 kHz, to less than 5 fs rms. The majority of the residual noise came then from the frequency bands, where the regulator was not active. Therefore, we expect to improve the overall suppression by carefully increasing the regulation bandwidth. In comparison, the above-mentioned plant instability prevented the proportional regulator from reducing the noise below 22 fs rms. Presumably, the use of multiple regulation stages, each working with $\gamma \approx 0.85$, could help overcome this situation. So in spite of its simplicity, improving the proportional regulation would require complex control system solutions, including more diagnostics, additional regulator hardware, and increased maintenance effort.

Another positive aspect of the proposed $\mathcal{H}_2$ design lies in its ability to estimate the size and frequency shape of important signals with the help of closed-loop transfer functions. In particular, functions S and KS can be tailored to a specific disturbance model in order to estimate residual noise and applied control effort, respectively. By displaying such frequency spectra together with their $\mathcal{H}_2$ norms, we showed an agreement between the model and measured data.

Therefore, having understood actual plant dynamics, we are now able to derive the right regulator parameters by (i) shaping a disturbance filter according to a measured noise spectrum and (ii) respecting a bandwidth limit given by a LLRF system. We expect this design procedure to be applicable to other cw machines as well. In addition, our implementation [32] could be transferred to these machines and tailored to their requirements.

Still, limiting the bandwidth of the new beam-based feedback method has an apparent downside. Namely, high-frequency noise cannot be addressed by the new regulator. Of course, suppressing such noise with an actuator that is based on a superconducting radio-frequency cavity with its inherently narrow bandwidth is problematic *per se*. Therefore, to counteract this negative scenario, a different design approach is required. For example, employing a normal conducting cavity that features a significantly wider bandwidth in order to specifically target the high-frequency noise [33,34]. Both regulators could then work in parallel, each targeting its own frequency range.

ACKNOWLEDGMENTS

The authors would like to thank Sven Pfeiffer from the German Electron Synchrotron (DESY) for fruitful discussions concerning beam-based feedback regulation. Special thanks goes also to Cagil Gümüs, Burak Dursun, and Łukasz Butkowski for their help with the MTCA.4 firmware framework. This work was partially funded by the Estonian Research Council Grant No. PRG658.

[1] B. Green *et al.*, High-field high-repetition-rate sources for the coherent THz control of matter, Sci. Rep. **6**, 22256 (2016).

[2] H. Schlarb, Techniques for pump-probe synchronisation of FSEC radiation pulses, in *Proceedings of the 21st Particle Accelerator Conference, Knoxville, TN, 2005* (IEEE, Piscataway, NJ, 2005), pp. 59–63.

[3] S. Kovalev, B. Green, T. Golz, S. Maehrlein, N. Stojanovic, A. S. Fisher, T. Kampfrath, and M. Gensch, Probing ultrafast processes with high dynamic range at 4th-generation light sources: Arrival time and intensity binning at unprecedented repetition rates, Struct. Dyn. **4**, 024301 (2017).

[4] W. Koprek, C. Behrens, M. K. Bock, M. Felber, P. Gessler, K. Hacker, H. Schlarb, C. Schmidt, B. Steffen, S. Wesch, S. Schulz, and J. Szewinski, Intra-train Longitudinal Feedback for Beam Stabilization at FLASH, in *Proceedings of 32nd International Free Electron Laser Conference Malmö, Sweden* (JACoW, Geneva, Switzerland, 2010), pp. 537–543.

[5] C. Schmidt, M. Bock, W. Koprek, S. Pfeiffer, H. Schlarb, and W. Jałmużna, Feedback strategies for bunch arrival time stabilization at FLASH towards 10 fs, in *Proceedings of 33rd International Free Electron Laser Conference,*

Shanghai, China (SINAP, Shanghai, China, 2011), pp. 531–534.

[6] S. Pfeiffer, C. Schmidt, M. K. Bock, H. Schlarb, W. Jalmuzna, G. Lichtenberg, and H. Werner, Fast feedback strategies for longitudinal beam stabilization, in *Proceedings of the 3rd International Particle Accelerator Conference, New Orleans, LA, 2012* (IEEE, Piscataway, NJ, 2012).

[7] S. Schulz, I. Grguraš, C. Behrens, H. Bromberger, J. T. Costello, M. K. Czwalinna, M. Felber, M. C. Hoffmann, M. Ilchen, H. Y. Liu, T. Mazza, M. Meier, S. Pfeiffer, P. Predki, S. Schefer, C. Schmidt, U. Wegner, H. Schlarb, and A. L. Cavalieri, Femtosecond all-optical synchronization of an X-ray free-electron laser, Nat. Commun. **6**, 5938 (2015).

[8] A. Rezaeizadeh, T. Schilcher, and R. S. Smith, Adaptive robust control of longitudinal and transverse electron beam profiles, Phys. Rev. Accel. Beams **19**, 052802 (2016).

[9] Z. Zhao, D. Wang, Z. Yang, and L. Yin, SCLF: An 8-GeV CW SCRF linac-based x-ray FEL Facility in Shanghai, in *Proceedings of 38th International Free Electron Laser Conference, Santa Fe, NM* (JACoW, Geneva, Switzerland, 2018), pp. 182–184.

[10] F. Zhou, C. Adolphsen, A. Benwell, G. Brown, D. H. Dowell, M. Dunning, S. Gilevich, K. Grouev, G. Huang, B. Jacobson, X. H. Liu, A. Miahnahri, F. Sannibale, J. Schmerge, and T. Vecchione, Commissioning of the SLAC Linac Coherent Light Source II electron source, Phys. Rev. Accel. Beams **24**, 073401 (2021).

[11] R. Brinkmann, E. Schneidmiller, J. Sekutowicz, and M. Yurkov, Prospects for CW and LP operation of the European XFEL in hard X-ray regime, Nucl. Instrum. Methods Phys. Res., Sect. A **768**, 20 (2014).

[12] P. Michel, The radiation source ELBE at the Forschungszentrum Dresden-Rossendorf, in *2008 IEEE Nuclear Science Symposium Conference Record, Dresden, Germany* (IEEE, New York, 2008), pp. 3078–3080.

[13] A. Bellandi, Ł. Butkowski, B. Dursun, A. Eichler, Ç. Gümüş, M. Kuntzsch, A. Nawaz, S. Pfeiffer, H. Schlarb, C. Schmidt, K. Zenker, and J. Branlard, Online detuning computation and quench detection for superconducting resonators, IEEE Trans. Nucl. Sci. **68**, 385 (2021).

[14] H. Vennekate, A. Arnold, P. Lu, P. Murcek, J. Teichert, and R. Xiang, Emittance compensation schemes for a superconducting rf injector, Phys. Rev. Accel. Beams **21**, 093403 (2018).

[15] M. Heuer, G. Lichtenberg, S. Pfeiffer, H. Schlarb, C. Schmidt, and H. Werner, Modeling of the master laser oscillator phase noise for the European XFEL using fractional order systems, in *IFAC Proc.* Vol. 47 (2014), p. 9235.

[16] M. Schütte, A. Eichler, H. Schlarb, G. Lichtenberg, and H. Werner, Decentralized output feedback control using sparsity invariance with application to synchronization at European XFEL, in *Proceedings of 60th IEEE Conference on Decision Control, Austin, TX* (IEEE, New York, 2021), pp. 5723–5728.

[17] M. Schütte, A. Eichler, H. Schlarb, G. Lichtenberg, and H. Werner, Convex synthesis of robust distributed controllers for the optical synchronization system at European XFEL, in *Proceedings of IEEE Conference on Control Technology and Applications, Trieste, Italy* (IEEE, New York, 2022), pp. 1061–1067.

[18] A. Wolski, *Beam Dynamics in High Energy Particle Accelerators* (Imperial College Press, London, England, 2014).

[19] P. Emma, *Bunch compression, Handbook of Accelerator Physics and Engineering*, 2nd ed. (World Scientific Publishing Co. Pte. Ltd., Hackensack, NJ, 2013), pp. 334–337.

[20] P. Emma, X-band RF harmonic compensation for linear bunch compression in the LCLS, Stanford Linear Accelerator Center, Stanford University, Stanford, CA, Technical note, Report No. LCLS-TN-01-1, 2001.

[21] K. Zenker, Ç. Gümüş, M. Hierholzer, P. Michel, S. Pfeiffer, H. Schlarb, C. Schmidt, R. Schurig, R. Steinbrück, and M. Kuntzsch, MicroTCA.4-based low-level RF for continuous wave mode operation at the ELBE Accelerator, IEEE Trans. Nucl. Sci. **68**, 2326 (2021).

[22] M. Kuntzsch, K. Zenker, A. Maalberg, A. Schwarz, M. Czwalinna, and J. Kral, Update of the bunch arrival time monitor at ELBE, in *Proceedings of 13th International Particle Accelerator Conference, Bangkok, Thailand* (JACoW, Geneva, Switzerland, 2022), pp. 260–262.

[23] A. Maalberg, M. Kuntzsch, and E. Petlenkov, Simulation of RF noise propagation to relativistic electron beam properties in a linear accelerator, IFAC Pap. **53**, 348 (2020).

[24] U. Lehnert, P. Michel, R. Schurig, A. Aksoy, P. Evtushenko, and J. Krämer, Bunch compression of the low-energy ELBE electron beam for super-radiant THz sources, in *Proceedings of the 5th International Particle Accelerator Conference, IPAC2014, Dresden, Germany* (JACoW, Geneva, Switzerland, 2014), pp. 1123–1125.

[25] N. Nise, *Nise's Control Systems Engineering*, global ed. (John Wiley & Sons, Ltd, Chichester, West Sussex, England, 2015).

[26] S. Skogestad and I. Postlethwaite, *Multivariable Feedback Control: Analysis and Design*, 2nd ed. (John Wiley & Sons, Ltd, Chichester, West Sussex, England, 2005).

[27] H. Kwakernaak, $\mathcal{H}_2$-optimization—theory and applications to robust control design, *IFAC Proc.* Vol. 33 (2000), p. 437.

[28] S. Boyd and C. Barratt, *Linear Controller Design: Limits of Performance* (Prentice-Hall Inc., Hoboken, NJ, 1991).

[29] A. Maalberg, M. Kuntzsch, and E. Petlenkov, Regulation of the linear accelerator ELBE exploiting continuous wave mode of a superconducting RF cavity, in *Proceedings of the 2022 American Control Conference, Atlanta, GA* (IEEE, New York, 2022), pp. 5346–5353.

[30] G. Balas, A. Packard, M. Safonov, and R. Chiang, Next generation of tools for robust control, in *Proceedings of the 2004 American Control Conference, Boston, MA* (IEEE, New York, 2004), pp. 5612–5615.

[31] MathWorks, linmod: Extract continuous-time linear state-space model around operating point, Available online at https://se.mathworks.com/help/simulink/slref/linmod.html (2023) [accessed: March 31, 2023].

[32] A. Maalberg, M. Kuntzsch, and E. Petlenkov, Real-time regulation of beam-based feedback: Implementing an FPGA solution for a continuous wave linear accelerator, Sensors **22**, 6236 (2022).

[33] S. Pfeiffer, J. Branlard, Ł. Butkowski, M. Hierholzer, M. Hoffmann, K. Honkavaara, H. Schlarb, C. Schmidt, S. Schreiber, M. Vogt, J. Zemella, and M. Fakhari, Status update of the fast energy corrector cavity at FLASH, in *Proceedings of 29th Linear Accelerator Conference, LINAC2018, Beijing, China* (JACoW, Geneva, Switzerland, 2018), pp. 112–114.

[34] S. Pfeiffer, Ł. Butkowski, M. Czwalinna, B. Dursun, C. Gerth, B. Lautenschlager, H. Schlarb, and C. Schmidt, Longitudinal intra-train beam-based feedback at FLASH, in *Proceedings of 39th Free Electron Laser Conference, FEL2019, Hamburg, Germany* (JACoW, Geneva, Switzerland, 2019), pp. 346–349.

Curriculum Vitae

1. Personal data

Name	Andrei Maalberg
Date and place of birth	16 October 1984 Tallinn, Estonia
Nationality	Russian

2. Contact information

Address	Tallinn University of Technology, School of Information Technologies, Department of Computer Systems, Ehitajate tee 5, 19086 Tallinn, Estonia
Phone	+372 56 45 1838
E-mail	andrei.maalberg@taltech.ee

3. Education

2019–2023	Tallinn University of Technology, School of Information Technologies, Information and Communication Technology, PhD studies
2015–2018	Tallinn University of Technology, Faculty of Information Technology, Computer and Systems Engineering, MSc *cum laude*
2012–2015	Tallinn University of Technology, Faculty of Information Technology, Computer and Systems Engineering, BSc *cum laude*

4. Language competence

Russian	native
English	fluent
Estonian	fluent
German	average
French	basic skills

5. Professional employment

2017–2017	IBM Research Zürich, Guest scientist
2013–2017	Proekspert, Software developer
2004–2012	Estonian National Opera, Ballet artist

6. Honours and awards

- 2018, The main prize and a special prize from AS Cybernetica at the ICT Thesis Contest in the Hardware and Systems category
- 2015, Skype and Study IT in Estonia Master's Scholarship

7. Defended theses

- 2018, SpaceWire to SPI Bridge in VHDL for Microsemi ProASIC3E FPGA, MSc, supervisor Prof. Dr. Eduard Petlenkov, Tallinn University of Technology, Faculty of Information Technology, Department of Computer Systems

- 2015, Towards Oculus Rift based Augmented and Virtual Reality, BSc, supervisor Prof. Dr. Eduard Petlenkov, Tallinn University of Technology, Faculty of Information Technology, Department of Computer Systems

8. Scientific work
Papers

1. A. Maalberg, M. Kuntzsch, K. Zenker, and E. Petlenkov. Regulation of electron bunch arrival time for a continuous-wave linac: Exploring the application of the $\mathcal{H}_2$ mixed-sensitivity problem. *Phys. Rev. Accel. Beams*, 26:072801, Jul 2023

2. A. Maalberg, M. Kuntzsch, and E. Petlenkov. Real-Time Regulation of Beam-Based Feedback: Implementing an FPGA Solution for a Continuous Wave Linear Accelerator. *Sensors*, 22(16):6236, Aug 2022

3. A. Maalberg, M. Kuntzsch, and E. Petlenkov. Regulation of the Linear Accelerator ELBE Exploiting Continuous Wave Mode of a Superconducting RF Cavity. In *Proc. 2022 Am. Control Conf.*, pages 5346–5353, Jun 2022

4. A. Maalberg, M. Kuntzsch, and E. Petlenkov. Simulation of RF Noise Propagation to Relativistic Electron Beam Properties in a Linear Accelerator. In *Proc. 21st IFAC World Congr.*, pages 348–354, Jul 2020

Elulookirjeldus

1. Isikuandmed

Nimi	Andrei Maalberg
Sünniaeg ja -koht	16.10.1984, Tallinn, Eesti
Kodakondsus	Eesti

2. Kontaktandmed

Aadress	Tallinna Tehnikaülikool, Infotehnoloogia teaduskond, Arvutisüsteemide instituut, Ehitajate tee 5, 19086 Tallinn, Estonia
Telefon	+372 56 45 1838
E-post	andrei.maalberg@taltech.ee

3. Haridus

2019–2023	Tallinna Tehnikaülikool, Infotehnoloogia teaduskond, Info- ja kommunikatsioonitehnoloogia, doktoriõpe
2015–2018	Tallinna Tehnikaülikool, Infotehnoloogia teaduskond, Arvutisüsteemid, MSc *cum laude*
2012–2015	Tallinna Tehnikaülikool, Infotehnoloogia teaduskond, Arvutisüsteemid, BSc *cum laude*

4. Keelteoskus

vene keel	emakeel
inglise keel	kõrgtase
eesti keel	kõrgtase
saksa keel	kesktase
prantsuse keel	algtase

5. Teenistuskäik

2017–2017	IBM Research Zürich, Külalisteadur
2013–2017	Proekspert, Tarkvaraarendaja
2004–2012	Estonia Rahvusooper, Balletiartist

6. Autasud

- 2018, Peaauhind ja eriauhind AS Cybernetica firmalt IKT lõputööde konkursil riistvara ja süsteemide kategoorias
- 2015, Skype ja Study IT in Estonia magistri stipendium

7. Kaitstud lõputööd

- 2018, SpaceWire to SPI Bridge in VHDL for Microsemi ProASIC3E FPGA, MSc, juhendaja Prof. Dr. Eduard Petlenkov, Tallinna Tehnikaülikool, Infotehnoloogia teaduskond, Arvutisüsteemide instituut
- 2015, Towards Oculus Rift based Augmented and Virtual Reality, BSc, juhendaja Prof. Dr. Eduard Petlenkov, Tallinna Tehnikaülikool, Infotehnoloogia teaduskond, Arvutisüsteemide instituut

8. Teadustegevus

Teadusartiklite, konverentsiteeside ja konverentsiettekannete loetelu on toodud ingliskeelse elulookirjelduse juures.

ISSN 2585-6901 (PDF)
ISBN 978-9916-80-054-6 (PDF)